

© 2016

Muharrem Acerce

ALL RIGHTS RESERVED

**Electrochemical Charge Storage and
Electrochemomechanical Behavior of Chemically
Exfoliated & Restacked MoS₂ Nanosheets**

By

MUHARREM ACERCE

A Dissertation submitted to the

Graduate School – New Brunswick

Rutgers, The State University of New Jersey

In partial fulfillment of the requirements

For the degree of

Doctor of Philosophy

Graduate Program in Materials Science and Engineering

Written under the direction of

Professor Manish Chhowalla

And approved by

New Brunswick, New Jersey

October, 2016

ABSTRACT OF THE DISSERTATION

Electrochemical Charge Storage and
Electrochemomechanical Behavior of Chemically Exfoliated and
Restacked MoS₂ Nanosheets

By MUHARREM ACERCE

Dissertation Director:
Prof. Manish Chhowalla

In the past few decades, there has been a tremendous ongoing effort to understand the nature of nanomaterials. Shrinking dimensions of the materials to the nanoscale regime reveal various intriguing properties of the nanomaterials due to quantum confinement effects. Especially, electron confinement in two dimensional materials enables compelling electronic properties as compared to the other nanostructured materials. Besides, thinning 2D materials down to monolayer thicknesses increases the surface-to-volume ratio to such an extent that makes them appealing for electrochemical energy conversion and storage technologies. Moreover, atomically thin 2D materials are flexible with good performance under bending, making them attractive materials for flexible electronics, energy storage devices and actuators.

Recent advancements in energy storage technologies using 2D materials, particularly in materials such as graphene and its analogues, would finally make

supercapacitors viable to complement or replace batteries. High surface-to-volume ratio and good ionic transport in addition to excellent electrical conductivity enables high charge storage capacities with fast energy uptake and delivery. For instance, graphene possess very high capacitive charge storage performance thanks to pure electrostatic attraction of ions (electrochemical double layer effect) on the highly porous carbon surface. Besides, pseudocapacitive 2D materials such as transition metal carbides (Mxenes) possess good electrical conductivity and capacitive performance concurrently because of the presence of transition metal in the structure. Transition metal dichalcogenides (LTMDs) such as molybdenum disulphide (MoS_2) are also studied candidate materials for electrochemical charge storage as well. However, naturally occurring MoS_2 has a 2H phase crystal structure with 1.9 eV band gap, which renders it semi-insulating and therefore not immediately attractive as an electrode material for energy storage. Despite, the 1T phase of MoS_2 is metallic and 10^7 time more conductive than 2H phase.

The aim of this work is to use the metallic 1T phase of MoS_2 , which can be obtained from the semiconducting 2H phase of MoS_2 during chemical exfoliation of the bulk material. In so doing, the ultimate goal is to exploit the phase transformation of MoS_2 and successfully utilize it as supercapacitor electrode. The results show that that chemically exfoliated nanosheets of MoS_2 containing a high concentration of the metallic 1T phase can electrochemically intercalate ions such as H^+ , Li^+ , Na^+ and K^+ with extraordinary efficiency and achieve capacitance values ranging from ~ 400 to $\sim 700 \text{ F cm}^{-3}$ in a variety of aqueous electrolytes. We also demonstrate that this material is suitable for high-voltage operation in non-aqueous organic electrolytes, showing

prime volumetric energy and power density values, coulombic efficiencies in excess of 95%, and stability over 5,000 cycles. As we show by X-ray diffraction analysis, these favourable electrochemical properties of 1T MoS₂ layers are mainly a result of their hydrophilicity and high electrical conductivity, as well as the ability of the exfoliated layers to dynamically expand and intercalate the various ions. The obtained layer expansion behavior can indeed be utilized to transform the energy to mechanical energy. Our findings indicate that charge storage induces a reversible elongation of electrodes, generating enough mechanical force to bend bimorph actuator and lift masses 100 times heavier than its own weight. This study also includes a detailed experimental work on the synthesis of the metallic MoS₂ phase, fabrication of supercapacitor and actuator electrodes and, their electrochemical and electrochemomechanical performance in various electrolytes.

DEDICATIONS

Dedicated to my beloved family

ACKNOWLEDGEMENTS

I would like to express my sincere appreciation to my advisor Prof. Manish Chhowalla for his continuous guidance and encouragement throughout my research. His wisdom helps me out whenever I lose my path and stuck on the details. Besides my advisor, special thanks to Dr. Damien Voiry for assistance during my PhD and also advice on styling techniques.

My sincerest thanks also go to the rest of the committee members: Prof. Lisa Klein, Prof. Glenn Amatucci, Prof. Tewodros Asefa and Assist. Prof. Koray Akdogan for their profound comments and encouragement, but also for the hard questions which inspired me to widen my research. Besides, my special thanks go to Assistant Prof. Koray Akdogan for technical editing and writing assistance on my thesis dissertation.

It is my pleasure to work with a group of brilliant, hardworking and sincere labmates, Dr. Cecilia de Carvalho Castro e Silva, Dr. Jeung Yang, Dr. Abdul Rahman Mohmad, Dr. Rajesh Kappera, Mr. Ibrahim Bozkurt, Mr. Sol Torrel, Mr. Raymond Fullon, Mr. Daniel Kaplan, Mrs. Yan Wang, Mrs. Maryam Salehi, and my friends in the Materials Science Department, Mr. Metin Ornek, Dr. Fatih Toksoy, Dr. E. Tevfik Ozdemir, Dr. Ilyas Savkliyildiz, Dr. Hulya Bicer, Dr. Binxing Yu, Mrs. Berra Beyoglu, Mr. Christopher Petoukhoff, Mr. Azmi Mert Celik, Mrs. Zeynep Ayguzer, Mr. Paul Kim, Dr. Kanak Kuwelkar, Dr. Vitor Almeida and Dr. Rafael Silva. Special thanks to Mr. Dheeraj Chandrasekhar and Mr. Hiren Makadia for assisting me on MATLAB coding.

My sincere thanks also go to my previous advisor, Prof. A.T. Charlie Johnson and his colleagues who gave me the interest on 2D materials by giving me the

opportunity to join his group, Dr. Xhengtang Luo, Dr. Brett Goldsmith, Dr. John Qi, Dr. Mitchell Lerner and Dr. Ye Lu.

I would like to acknowledge Ministry of National Education Ministry in Turkey for supporting all my expanses throughout my Master and PhD education. I would like to also acknowledge Materials Science Department at Rutgers University and University of Pennsylvania for providing us the opportunity to share knowledge and resources to explore new materials.

I would like to express my heartfelt thanks to my entire family including ones who are not among us, Meryem and Lutfullah Acerce. Without their love, encouragement and patience, I would not complete this degree successfully.

Table of Contents

Abstract	ii
Dedications	v
Acknowledgments	vi
Table of Contents	viii
List of Figures	xiv
List of Tables	xviii
Chapter 1. Introduction	1
1.1 Motivation	1
1.2 Objective and Scope of the Work	4
1.3 Organization of Thesis	5
Chapter 2. Molybdenum Disulphide (MoS₂)	6
2.1 Structure of MoS ₂	7
2.2 Phase Transformation in MoS ₂	8
2.3 Electronic Properties of 2H Phase MoS ₂ and 1T Phase MoS ₂	9
2.4 Phase Characterization	11
2.4.1 RAMAN Spectroscopy	11
2.4.2 X-Ray Photoelectron Spectroscopy	12
2.5 1T Phase MoS ₂ Synthesis	13
2.5.1 Lithiation and Chemical Exfoliation Process	13

2.5.2	Restacking of Exfoliated MoS ₂	14
2.5.2.1	Crystal Structure of Restacked and intercalated MoS ₂	14
2.6	MoS ₂ as a Supercapacitor Electrode	16
2.7	MoS ₂ as a Piezoelectric Material and an Electrochemical Actuator	18
2.8	Mechanical Properties of MoS ₂	19
2.9	Chapter Summary	20
Chapter 3. Electrochemical Supercapacitors		22
3.1	Supercapacitor Device Configuration	24
3.1.1	Electrode Materials	25
3.1.1.1	Carbonaceous Materials	26
3.1.1.1.1	Pore and Channel Distribution	27
3.1.1.1.2	Pore Size and Shape Effect	27
3.1.1.1.3	Functionalization	28
3.1.1.2	Transition Metal Oxides	29
3.1.1.2.1	Ruthenium Oxide	29
3.1.1.2.2	Manganese Oxide	30
3.1.1.2.3	Conjugated Polymers	31
3.1.2	Electrolytes	32
3.1.2.1	Aqueous Electrolytes	33
3.1.2.2	Organic Electrolytes	33
3.1.2.3	Ionic Liquids	33
3.1.3	Separators	34
3.2	Electrochemical Characterization Techniques	34

3.2.1	Cyclic Voltammetry (CV)	35
3.2.1.1	Randles-Sevcik Equation	38
3.2.2	Galvanostatic Charge/Discharge	39
3.2.2.1	Energy Density / Power Density Calculations	40
3.2.3	Electrochemical Impedance Spectroscopy (EIS)	40
3.3	Charge Storage Mechanisms	43
3.3.1	Electrochemical Double Layer Capacitors	43
3.3.1.1	Double Layer Phenomena and Models	45
3.3.1.2	Hemholtz Double Layer	47
3.3.1.3	Gouy-Chapman Model	48
3.3.1.4	Stern Model (1924)	48
3.3.1.5	Grahame Model (1947)	49
3.3.1.6	Bockris/Devanathan/Müller (1963)	49
3.3.1.7	Failure at Classical Double Layer Model (BDM)	50
3.3.2	Pseudocapacitors	50
3.3.2.1	Pseudocapacitor Models	52
3.3.3	Understanding the Charge Storage Mechanisms	54
3.4	Chapter Summary	57
Chapter 4. Electrochemical Actuators		58
4.1	Electrochemical Actuator Device Configuration	61
4.2	Electrochemical Actuation Measurement Techniques	63
4.3	Bimorph Actuators	66
4.3.1	Mechanical Calculations	69

4.3.2	Work Density Calculations	71
4.4	Electrochemical Expansion Mechanisms	72
4.4.1	Ion Intercalation/de-intercalation	73
4.4.2	Faradaic Redox Reaction	73
4.4.3	Quantum Mechanical and Electrostatic Effect	73
4.5	Chapter Summary	74
Problem Statement and Solution Strategy		75
Chapter 5. Experimental Results		77
5.	Material Synthesis, Electrode Fabrication and Material Analysis	77
5.1	Lithiation and Chemical Exfoliation of MoS ₂	77
5.2	Restacking of Exfoliated MoS ₂ for Electrode Fabrication	78
5.3	Fabrication of Chemically Exfoliated 2H Phase MoS ₂ Electrodes	78
5.4	Physical Characterizations	79
5.4.1	Characterizing Chemically Exfoliated Single Layer MoS ₂	79
5.4.2	Characterizing Phase Transformation from 2H to 1T MoS ₂	80
5.4.2.1	Raman Spectroscopy	80
5.4.2.2	X-ray photoelectron spectroscopy (XPS)	80
5.4.3	Characterizing Restacked MoS ₂	81
5.4.3.1	X Ray Diffraction (XRD)	81
5.4.3.2	Scanning Electron Microscopy (SEM)	82
5.4.3.3	Measurements Contact Angle	83
5.5	Chapter Summary	84

Chapter 6. Electrochemical Characterizations	85
6.1. Electrochemical Measurements in Aqueous Electrolytes	85
6.1.1. Cyclic Voltammetry	85
6.1.1.1. In Neutral Electrolytes	86
6.1.1.2. In Acidic Electrolyte	88
6.1.1.3. Thickness Effect	89
6.1.1.4. 2H and 1T phase MoS₂ Comparison	90
6.1.1.5. Comparison of All Aqueous Electrolytes	91
6.1.2. Galvanostatic Charging/discharging Measurements	92
6.1.3. Electrochemical Impedance Spectroscopy (EIS)	93
6.1.4. Discussion for Aqueous Electrolytes	95
6.2 Electrochemical Behavior in Organic Electrolytes	97
6.2.1 Cyclic Voltammetry	97
6.2.2 Galvanostatic Charging/discharging Measurements	99
6.2.3 Ragone Plot	100
6.2.4 Full Device Comparison with Thicker Electrode	101
6.2.5 Discussion for Organic Electrolytes	104
6.3 Chapter Summary	105
Chapter 7. Ex-situ XRD Analysis	106
7.1 Experimental Setup for Ex-situ XRD Analysis	106
7.2 Results & Discussion for Ex-situ XRD Analysis	107
7.3 In –situ RAMAN Spectroscopy	110

7.4 Chapter Summary	111
Chapter 8. Electrochemical Actuation with MoS₂	112
8.1 Electrochemical Actuation Experimental Setup	112
8.2 Electrochemical Induction and Mechanical Response	114
8.2.1 Capacitance vs Curvature Change	117
8.2.2 Potential Range vs Curvature Change	118
8.2.3 Electrochemical Actuation in Neutral Electrolytes	120
8.2.4 Cycle Stability	121
8.3 Understanding the Bending Mechanics	122
8.3.1 Thin Film Approximation (Stoney Approach)	122
8.3.2 Multilayer Bending Models	124
8.3.3 Mechanical Work Density	126
8.4 Inverted Series Connected Bimorph Actuator	128
8.4.1 The Inverted S-beam Actuator Fabrication	129
8.4.2 The Inverted S-beam Actuator Energy Calculations	130
8.5 Discussion	133
8.6 Chapter Summary	135
Chapter 9. Future Works and Conclusion	136
9.1 Future Work	136
9.2 Conclusion	137
References	138

List of Figures

Figure 1.1 Ragone chart comparison	2
Figure 2.1 Schematic of layered MoS ₂ crystal structure	6
Figure 2.2 Crystal structure of 2H phase and 1T phase MoS ₂	8
Figure 2.3 Atomic orientation & density of states for 2H and 1T phase MoS ₂	10
Figure 2.4 Band structure of 2H phase MoS ₂ and 1T phase MoS ₂	10
Figure 2.5 Raman spectrum for 1T MoS ₂ and 2H MoS ₂	11
Figure 2.6 X-ray photoelectron spectroscopy	12
Figure 2.7 X-ray diffraction patterns of suspended single layer MoS ₂ in water	15
Figure 2.8 Schematics of the cation intercalated $A_x(H_2O)_yMoS_2$ compounds	16
Figure 2.9. Electrochemical charge storage on 2H phase MoS ₂	17
Figure 2.10. Illustration for surface redox charge storage on 1T phase WS ₂	19
Figure 3.1. Principle of a single-cell double-layer capacitor	22
Figure 3.2. Gravimetric capacitance vs specific surface area	27
Figure 3.3. Pore size effect on the specific surface capacitance	28
Figure 3.4. Comparison of ideal and real cyclic voltammograms	37
Figure 3.5. Galvanostatic charge / discharge curve	39
Figure 3.6. Equivalent circuit models and equivalent Nyquist plot	42
Figure 3.7. Schematics of capacitor and EDLC	44

Figure 3.8. Schematic representation of a double layer on an electrode	45
Figure 3.9. The Helmholtz, Gouy-Chapman, Stern and Grahame models	47
Figure 3.10. CV curves for various materials	51
Figure 3.11. Langmuir and Temkin isotherms	53
Figure 3.12. The intercalation of cations between $\text{Ti}_3\text{C}_2\text{T}_x$ layers	55
Figure 3.13. The dilatometer technique	56
Figure 4.1. Design principles for actuator systems	60
Figure 4. 2. Schematic of electrochemical actuator device	62
Figure 4.3. Highly oriented MEGO sheets as actuator electrode	64
Figure 4.4 Graphene actuators	65
Figure 4.5. Graphene based bilayer actuator	66
Figure 4.6. Schematics of displacement measurements of actuator	67
Figure 4.7. Illustration of strain with charge injection and DL	74
Figure 5.1. Schematics of chemical exfoliation of MoS_2	77
Figure 5.2. Schematics of restacking process of MoS_2	78
Figure 5.3. SEM images of as-exfoliated 1T phase MoS_2 nanosheets	79
Figure 5.4. Raman spectra of 1T MoS_2 compared to 2H MoS_2	80
Figure 5.5. XPS survey spectrum for as-exfoliated 1T MoS_2	81
Figure 5.6. X-ray diffraction of bulk MoS_2 compared to restacked MoS_2 .	82

Figure 5.7. Side-view of the electrode observed by SEM	83
Figure 5.8. Static contact angle images of 1T MoS ₂ film	83
Figure 6.1. CVs of 1T phase MoS ₂ electrodes in 0.5 M Na ₂ SO ₄	86
Figure 6.2. Comparison of the CV curves of 1T MoS ₂	87
Figure 6.3. CV characteristic of 1T phase MoS ₂ in 0.5M H ₂ SO ₄	88
Figure 6.4. Thickness effect on the capacitance of 1T MoS ₂	89
Figure 6.5. Comparison of the capacitances at different annealing conditions	91
Figure 6.6. The volumetric capacitance of the 1T phase MoS ₂ electrodes	92
Figure 6.7. Galvanostatic cycles from 0.5 A/g to 16 A/g current rates	93
Figure 6.8. Nyquist plot of 1T MoS ₂ electrode	94
Figure 6.9. Nyquist plot for the transition from 1T MoS ₂ to 2H MoS ₂	95
Figure 6.10. Electrochemical behaviour in organic electrolytes	98
Figure 6.11. CV curves of 1T MoS ₂ electrodes in TEA BF ₄ /MeCN	99
Figure 6.12. Galvanostatic charging/discharging curves in TEA BF ₄ /MeCN	100
Figure 6.13. Ragone plot	101
Figure 6.14. Thicker electrodes with 1T phase MoS ₂ / PTFE	103
Figure 7.1. Schematic of the ex-situ X-ray diffractometer	106
Figure 7.2. Ex-situ X-ray diffraction from restacked 1T phase MoS ₂ films	108
Figure 7.3. In-situ Raman spectra of 1T MoS ₂	110

Figure 8.1. Schematics of experimental setup to track the actuation	113
Figure 8.2. Schematics of bending beam and corresponding charge flow	115
Figure 8.3. Time dependence of curvature change	116
Figure 8.4. Curvature change and capacitance at different frequencies	117
Figure 8.5. The curvature change at different potential ranges	119
Figure 8.6. The curvature change via square wave potential	120
Figure 8.7. Comparison of the actuation in different electrolytes	120
Figure 8.8 . Cycle stability test in 0.5 M H ₂ SO ₄	121
Figure 8.9. Snapshots of bending status of MoS ₂	123
Figure 8.10. Maximum curvature values for different thickness ratios	125
Figure 8.11. Comparison of actuator systems	127
Figure 8.12. Schematic of inverted IPC bimorph actuator to lift up weight	128
Figure 8.13. Schematics of IPC actuator fabrication	130
Figure 8.14. Stretched IPC actuator under loading	131

List of Tables

Table.1. Actuation performance of various materials	59
--	----

Chapter 1. Introduction

1. Motivation

The increasing global demand for energy, depleting fossil fuels and rising global warming threat due to fossil fuel usage have led to the investigation of clean, efficient and sustainable energy production systems. Besides energy conversion as part of the global clean energy efforts, there is a vast amount of ongoing work on electrochemical energy storage systems such as rechargeable batteries[1], [2] and supercapacitors[3]–[8].

Recently, the electrochemical supercapacitors (ECs) have drawn attention due to their high charge storage capabilities and fast charge delivery performance as compared to conventional capacitors and batteries[4], [9]. Considering the long charging time and low power output of batteries, supercapacitors provide better power performance with fast charging/discharging rate. Therefore, ECs are very promising energy storage devices in high power hybrid vehicles where mechanical energy can be recovered during deceleration (braking) and then used during acceleration over short time scales[10]. Moreover, ECs also have very long service life[4] (10^5 cycles) as compared to rechargeable batteries (10^3 cycles).

On the other hand, higher fabrication costs[3] and lower charge storage capacity[10] as compare to Li-ion batteries limit the ECs usage in the marketplace (see Fig. 1.1). Therefore, extensive research efforts are geared toward improving the ECs devices to make them cost effective without sacrificing their power density.

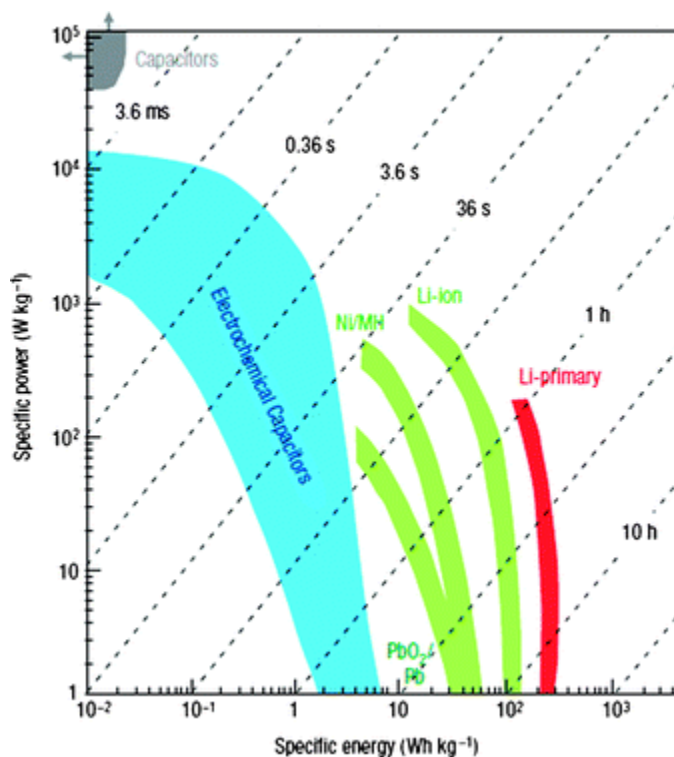


Figure 1.1 Ragone chart comparison for various electrochemical energy conversion and storage systems[10].

A deep understanding of the charge storage mechanism in ECs is important to find the most appropriate material in device applications. According to the previous studies, ECs are classified based on two distinct charge storage mechanisms:

- (1) Electrochemical double layer capacitor (EDLC)
- (2) Pseudocapacitors

The charge storage for electrochemical double layer capacitors (EDLCs) is based on the electrostatic attraction of charges on the surface of porous electrode[9], [11]. By applying an electrical potential, the charge separation occurs at the interface of electrode/electrolyte without any chemical reaction (non-Faradaic) as in conventional capacitors. Pseudocapacitors, on the other hand, store charges on the surface of an active

material via fast redox reaction (Faradaic)[3], [12, p. 2]. Redox reactions typically enable two orders of magnitude higher energy storage capacity than electrostatic double layer charge storage[3]. However, pseudocapacitors have lower cycle stability as compared to EDLCs due to the faradaic reaction. In order to enhance the cycle stability and charge storage capacity, hybrid systems were proposed by combining EDLC materials with pseudocapacitive materials[13]. Since the double layer formation and surface redox reaction occur on the surface of the active material, highly porous materials are required for both charge storage mechanisms. The first rule of attack to increase the surface area is to utilize porous or nanostructured materials[13]. However charge storage only occurs over a few angstrom distances on the surface, which is why excessive pore volume is not desired. Here, one needs to optimize pore size to minimize the unnecessary volume[14].

Layered materials are promising candidates for an efficient pore distribution due to their anisotropic crystal structures. The layer separation in such materials can be engineered by introducing guest species between the layers. This methodology enables one to obtain the highest volumetric capacitance in pore engineered graphene[15], [16]. In addition to graphene, other layered materials such as VS_2 , Ti_2C_3 are used as supercapacitor electrodes and exhibit notable capacitive behaviour[5], [8], [17, p. 2]. Furthermore, limited number of studies have addressed the properties of two-dimensional layered transition metal dichalcogenides (2D LTMDs) such as molybdenum disulfide (MoS_2) [18]–[20] and determined that their charge storage performance is quite poor. A key reason for this is that the electrodes tested in previous studies were comprised of the 2H phase of MoS_2 nanosheets that possess poor electrical conductivity. To enhance the conductivity, hybrid electrodes such as graphene/ MoS_2 [21] and polyaniline/ MoS_2 [22]

have been investigated. To date, the electrochemical storage performance obtained thus far with either pure or hybrid 2H phase MoS₂ electrodes has been relatively modest as compared to graphene [7], [23] or MXene (Ti₂C₃) electrodes [8].

2.Objectives and Scope of the Work

The major problem with MoS₂ based supercapacitors is their poor conductivity. There is another phase of MoS₂, 1T phase, which is 10⁷ times more conductive than 2H phase MoS₂ [24]. 1T phase has layered structure similar to 2H phase, and can be obtained in the form of monolayer as a result of chemical exfoliation technique via organolithium chemistry. Considering the layered morphology and comparably higher conductance similar to reduced graphene oxide, 1T phase of MoS₂ can be a candidate as supercapacitor electrode, however there is no report about 1T phase MoS₂ based supercapacitors. Therefore, the primary objective of this thesis dissertation will be using 1T phase MoS₂ as supercapacitor electrode.

Here, I propose phase engineered MoS₂ electrodes for use in supercapacitor. Accordingly, the scope of the thesis is to develop a methodology to fabricate the 1T phase MoS₂ electrode, convey the electrochemical analysis and understand the mechanism of charge storage. To synthesize monolayer 1T phase MoS₂, I propose to use the previously constructed lithiation and exfoliation procedure[24]. On the other hand, typical vacuum filtration technique will be used to fabricate supercapacitor electrodes. To characterize the phase transformation, chemical exfoliation, and restacking of MoS₂, various characterization techniques will brought to bear including SEM, XPS, HR TEM, XRD. To analyze the electrochemical charge storage behavior, electrochemical analysis

will be conducted including cyclic voltammetry, galvanostatic charge/discharge and electrochemical impedance analysis in various electrolytes. To unveil the charge storage mechanism, the structural changes associated with the charge storage will be screened via ex-situ XRD analysis. To monitor the macroscopic effects of charge storage; the electrode expansion/contraction will be monitored using bimorph actuator configuration.

3. Organization of the Thesis

Chapter 1 of the thesis is a brief introduction to the energy storage technologies, the challenges and the proposals to address these issues. Correspondingly, Chapter 1 establishes a motivation to the specific objectives of the thesis project. Chapter 2 provides a detailed literature survey to review the layered materials, especially MoS_2 , which is the key material considered in this study. Chapter 3 gives a detailed literature review about electrochemical supercapacitors to convey fundamental understanding of the charge storage systems. Chapter 4 provides an introduction to electrochemical actuator systems and mechanical aspect of the electroactive materials. Chapter 5-8 cover the experimental studies of the thesis. Chapter 5 elaborates on the implemented procedures for materials synthesis (1T phase MoS_2) to fabricate state-of-the-art supercapacitor electrode including lithiation, chemical exfoliation, phase transformation, vacuum filtration and their characterizations via SEM, XPS, Raman, HR STEM. Chapter 6 focuses on the electrochemical analyses of 1T and 2H phase MoS_2 in different electrolytes to explore the capacitive behavior. Chapter 7 specifically investigates the charge storage mechanism via ex-situ XRD analysis and in-situ Raman spectroscopy. Chapter 8 focuses on the electromechanical properties of MoS_2 under electrochemical induction. Finally Chapter 9 summarizes the thesis and concludes with the future works.

Chapter 2 Molybdenum disulfide (MoS₂)

The transition metal dichalcogenide is the common form for the compounds consisting of one transition metal atom (Group IVB, VB or VIB transition metals) and two chalcogenide atoms (S, Se or Te)[25]. These transition metals have commonly +4 oxidation states and bond covalently with two chalcogene atoms as illustrated in Fig. 2.1. Molybdenum disulphide is one of the most investigated layered transition metal dichalcogenides (LTMDs). Between the S-Mo-S layers, no metal atoms are present and weak Van der Waals bonds (S~S) hold individual MoS₂ sheets. These weak Van der Waals bonds make bulk MoS₂ a good solid lubricant[26].

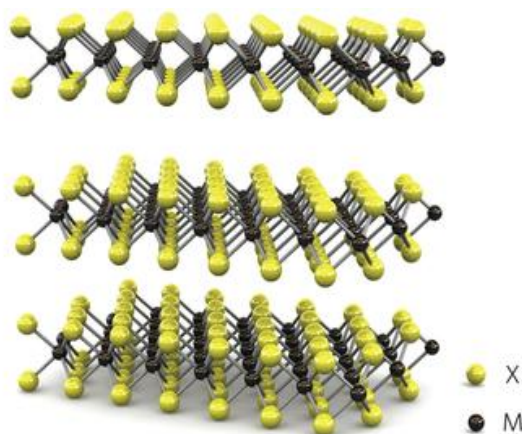


Figure 2.1 Schematic of layered MoS₂ crystal structure[27].

Current interest in MoS₂ arises from the ability to isolate MoS₂ sheets thanks to the weak Van der Waals bonds between the sheets. Unlike bulk MoS₂, exfoliated single layer MoS₂ shows distinct electrical[24], optoelectronic[24], and mechanical[28] properties. Therefore, MoS₂ may have found potentially applications as semiconductor materials for transistors[29] (electronics) and solar cells[30] (optoelectronics). Also MoS₂ was

proposed as electrode material for Li-ion battery application[31] and as catalyst material for hydrogen evolution reaction (HER) [32].

2.1 Structure of MoS₂

Structurally bulk MoS₂ is a layered structure where molybdenum atoms are sandwiched between sulphur atoms as illustrated in Fig. 2.1. There are three polymorphs of MoS₂ which are 2H MoS₂, 1T MoS₂ and 3R MoS₂. The different polymorphs are based on the change in the coordination of metal atoms in the primitive unit cell [25], [33]. The 2H phase MoS₂ is the most stable phase where the coordination of Mo atom is trigonal prismatic (Space group: P6₃-mmc)[34]. There are six “S” atoms covalently bonded with one “Mo” atom as shown in Fig. 2.2a.

Structurally, 2H MoS₂ layers can be distorted by intercalating lithium atoms between MoS₂ layers. After distortion, the position of bottom three sulphur atoms rotate 60° with respect to upper sulphur atoms, then the coordination of Mo atoms become octahedral as illustrated in Fig. 2.2b. (Space group: P3)[35]. While 2H MoS₂ is stable, 1T MoS₂ is a metastable phase that relaxes back to 2H MoS₂ at mild annealing conditions (98°C)[36].

Due to the 60° rotation of sulphur atoms in 2H MoS₂, all six sulphur atoms are visible from top view of single layer 1T phase MoS₂ and but only three sulphur atoms are visible for 2H phase MoS₂ (Fig 2.2(a,b))[37]. Because of the differences in planar densities of these planes, it is possible to discern between the 2H and 1T phases by High Resolution Scanning Transmission Electron Microscopy (HR STEM)[25] as shown in Fig. 2.2(c,d).

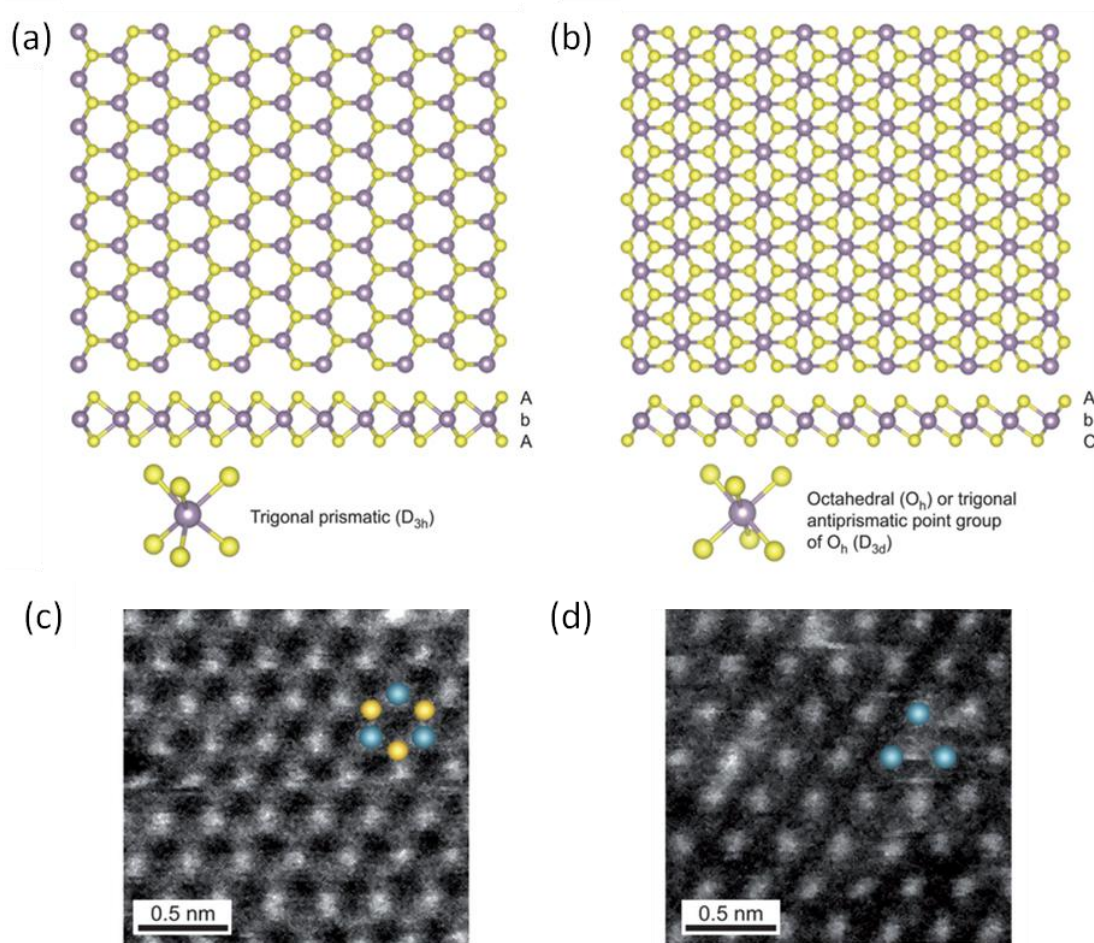


Figure 2.2 Crystal structure with top view and side view with layer stacking for trigonal 2H phase MoS₂ (a) and octahedral 1T phase MoS₂ (b). Dark-field scanning transmission electron microscopy image of single-layer MoS₂ showing the contrast variation of 2H (c) and 1T (d)[25]

2.2 Phase Transformation in MoS₂

The 2H phase is the most stable one in the MoS₂ system, but other phases can also form if a phase transformation can be induced. In order to promote a phase transformation from the 2H to 1T phases in MoS₂, typically an alkali metal intercalation process is used[33]. Ideally, the missing atoms between two MoS₂ sheets enable

interplanar cationic insertion in between the MoS₂ sheets. However, the 2H MoS₂ has tendency to resist intercalation unless lithium atoms with strong reducing agents such as n-butyl[38]. Then lithium atoms are able to diffuse through the octahedral and tetrahedral sites in the hexagonal crystal structure. During the lithiation process, a charge transfer occurs from the valence s orbital of the lithium atom to the d orbital of the molybdenum atom. The charge transfer might be responsible for destabilization of the 2H phase structure. It makes the 1T phase more favorable.

2.3 Electronic Properties of 2H Phase MoS₂ and 1T Phase MoS₂

According to experimental and the theoretical studies, the bulk 2H form of MoS₂ is a semiconductor with an indirect band gap of 1.2 eV [39]. On the other hand, 1T phase of MoS₂ exhibits metallic conduction that is 10⁷ times higher than 2H phase's conductivity[24]. Such distinct electronic behavior between the 2H and 1T originates from the difference in the coordination of Mo atoms, resulting in different electron configuration (d orbitals) and band structure as shown in Figs.(2.3,2.4). For trigonal prismatic coordination, the d-orbitals split into three bands with occupied d_z^2 and unoccupied $d_{x^2-y^2,xy}$, and $d_{xz,yz}$ states[25]. Split orbitals and fully occupied states render a band gap with semiconductive behavior for 2H phase of MoS₂.

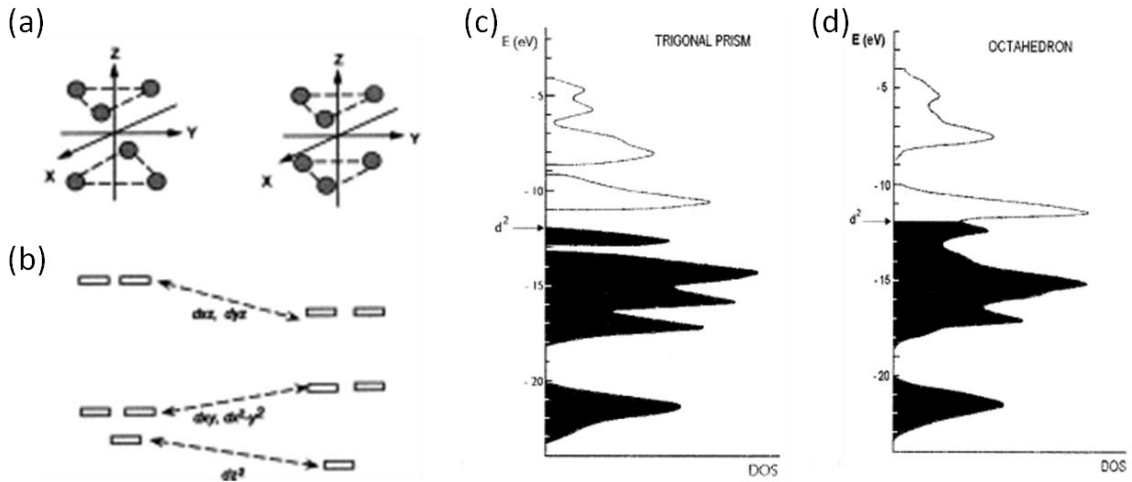


Figure 2.3 Atomic orientation of sulphur atoms for 2H and 1T phase MoS₂ (a), electrons states for d orbital of MoS₂ (b), corresponding density of states for 2H phase MoS₂ (c) and 1T phase MoS₂ (d) [33].

On the other hand, octahedrally coordinated Mo atoms have partially occupied degenerate $d_{z^2}, d_{x^2-y^2}$ (e_g) and d_{yz}, d_{xz}, d_{xy} (t_{2g}) orbitals[25]. Two electrons are shared by three degenerate orbitals and partially filled states render an overlapping band structure in the Fermi level energy (Fig. 2.4). Therefore, 1T MoS₂ presents metallic behavior.

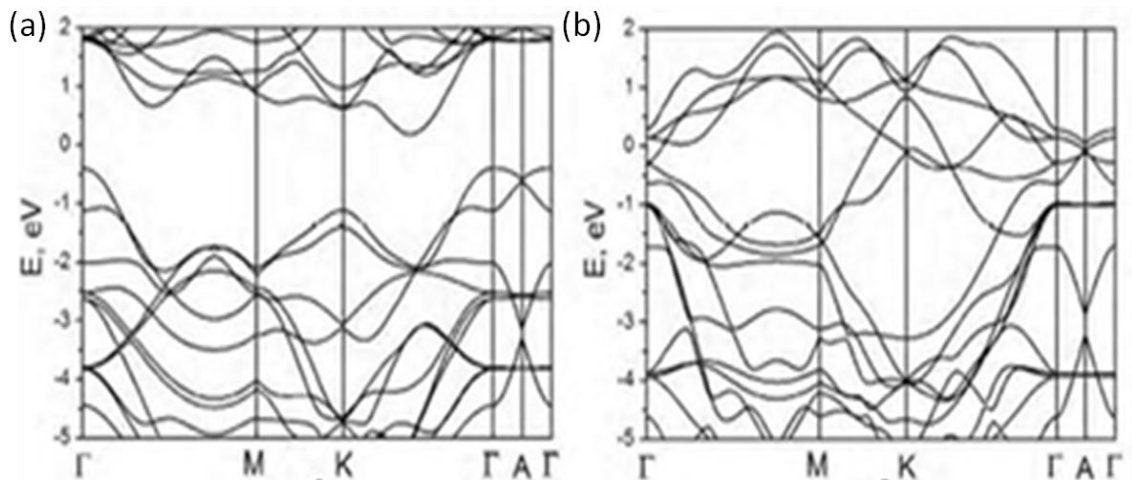


Figure 2.4 Band structure of 2H phase MoS₂ (a) and 1T phase MoS₂ (b).[40]

2.4 Phase Characterization

2.4.1 Raman Spectroscopy

Raman spectroscopy can be used to characterize the phase transformations in MoS₂ because of the different vibrational modes of 1T MoS₂ and 2H MoS₂ [41]. There are two main Raman modes in 2H MoS₂, the in-plane E_{2G}^1 mode and the out-of-plane A_{1G} mode. Several additional RAMAN signatures appear in the spectrum of single layer 1T MoS₂ that are designated as J_1 , J_2 and J_3 peaks at 156 cm⁻¹, 226 cm⁻¹ and 333 cm⁻¹ [41], [42]. The presence of these new peaks are attributed to zone folding mechanism due to the formation of $2 a_0 \times a_0$ superlattice structure in a single layer MoS₂[41]. While Raman spectroscopy is effective in qualitative phase analyses, it does not help with quantitative phase analysis.

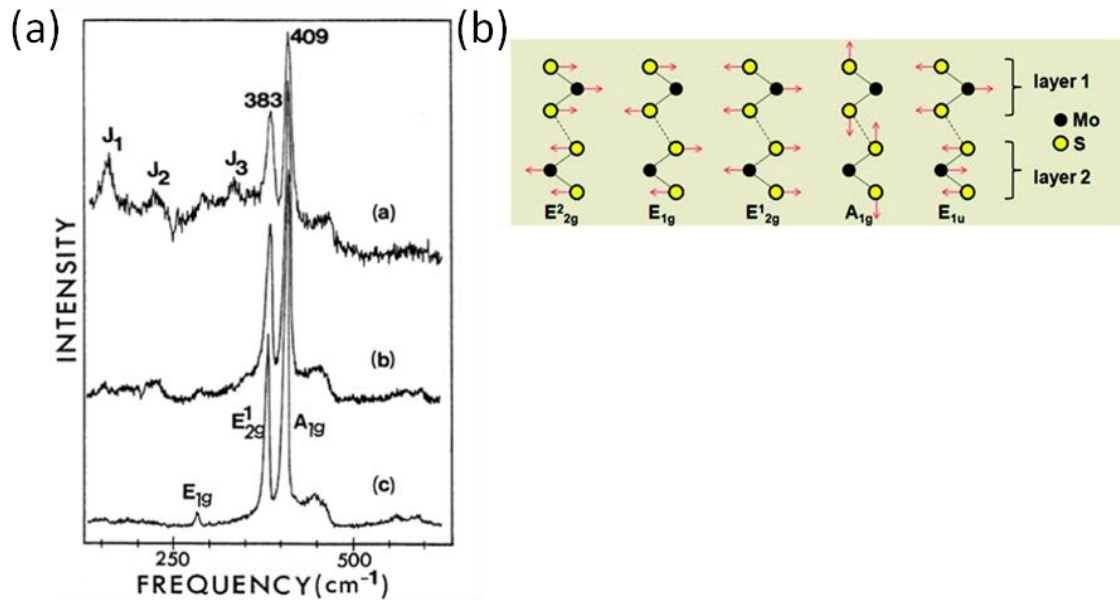


Figure 2.5 Raman spectrum for 1T MoS₂ and 2H MoS₂ (a). Corresponding vibration schematics for the vibration modes in the RAMAN spectrum(b) [41].

2.4.2 X-Ray Photoelectron Spectroscopy (XPS)

XPS is a more effective method for assessing the phase composition of MoS₂ [24]. After chemical exfoliation, both 2H and 1T phases coexist, and Raman spectroscopy cannot provide a quantitative assay. On the other hand, XPS elemental analysis is based on characteristic binding energies of each element and bond. For 2H MoS₂, there are two bonds present giving peaks for Mo 3d (229.5eV and 232eV) and S2p regions. Due to the different positioning of sulfur atom around Mo atoms for 1T MoS₂, Mo3d peak signals coming from the 1T phase are down-shifted by ~ 0.9 eV. Since both phases are present, XPS gives a convoluted peak for Mo 3d region. By deconvoluting the Mo 3d peak, we calculate the amount of 1T phase and 2H phase content of the MoS₂ film. The typical gradual phase transformation of 1T to 2H as induced by annealing and the corresponding Mo3d, S2s and S2p peaks[24] are shown (Fig. 2.6).

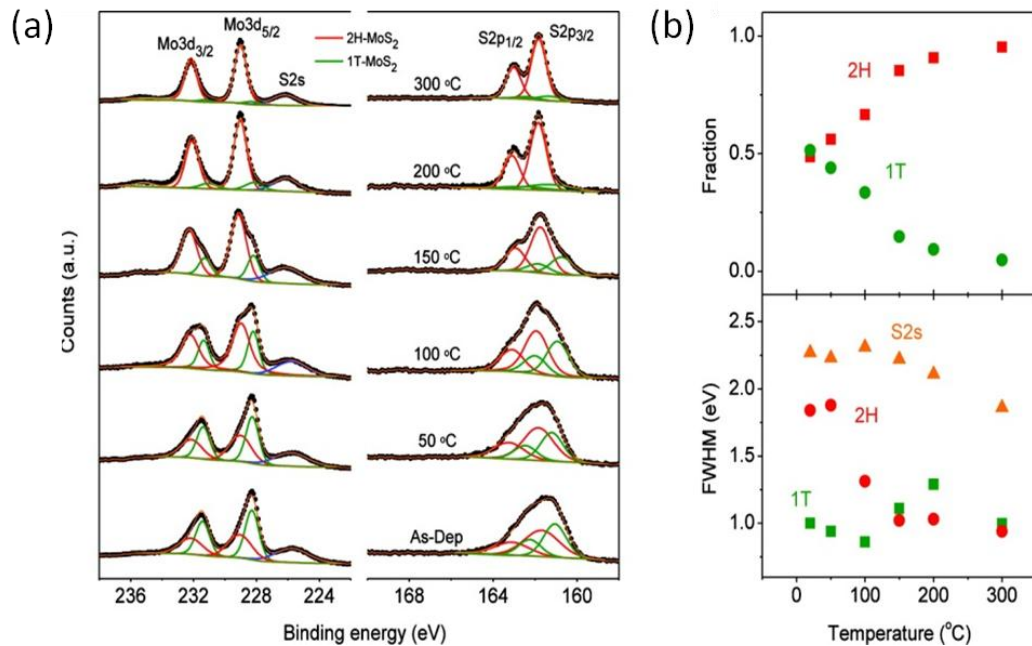


Figure 2.6 Phase difference can be detected by X-ray photoelectron spectroscopy[24].

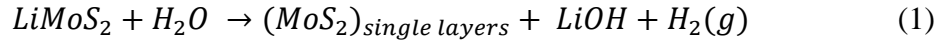
2.5 1T Phase MoS₂ Synthesis

There are two proposed methods for the phase transformation of the 2H phase to the 1T phase. The common method is the alkali cation insertion into 2H MoS₂. [43] This method has been studied since the 1970s and the mechanism of phase transformation is well understood [44]. To promote phase transformation, an electron needs to be donated from the alkali cation to 2H MoS₂. Recently, a new method was reported for local phase transformation [45]. By irradiating MoS₂ with an electron beam, it is possible to induce the phase transformation on a small domain of a few nm² in size. While this mechanism is not well understood, it is speculated that charging with the electron beam plays a role in inducing the phase transformation.

2.5.1 Lithiation and Chemical Exfoliation Process

The chemical exfoliation method is more appropriate to fabricate electrode material because it is applicable to mass production. The 1T MoS₂ was first obtained by a chemical exfoliation process by Joensen et al [44]. In this method, one utilizes butyl lithium with hexane by which lithium cations are inserted into layered MoS₂. Lithium diffuses toward the octahedral and tetrahedral vacant sites in the layered MoS₂ structure and weakens the van der Waals bonds between the MoS₂ layers. Here, the lithium reacts with MoS₂ by giving one electron. This process causes a distortion in the MoS₂ crystal structure and the trigonal molecular orientation of the atoms transforms to the octahedral coordination. At the end of the intercalation process, LiMoS₂ compound is obtained in an inert atmosphere. To remove lithium, the intercalated compound (LiMoS₂) is mixed with

deionized water in a sonication bath. Then, subsequent reaction of Li with water results in LiOH by the following reaction and MoS₂ layers are thereby exfoliated [24].



Here, due to the reaction and agitation of intercalated particles by sonication, weaker van der Waals bonds break and bulk MoS₂ exfoliates. During this process, full dispersion in water solution takes place, including single layer MoS₂ layers, butyl group and LiOH. Upon centrifuging at 10k rpm for three times, single layer MoS₂ can be purified and colloidally dispersed by which the 1T phase MoS₂ is obtained[24]. Interestingly chemically exfoliated MoS₂ retains its 1T phase after removing the intercalated Li by exfoliation. Then 2H phase of MoS₂ is successfully transformed to 1T phase of MoS₂ via lithiation and exfoliation.

2.5.2 Restacking Exfoliated MoS₂

Single layer MoS₂ flakes disperse colloidally in water and are stable for months[24], but they require an additional process to transfer exfoliated layers onto a desired substrate. By using a vacuum filtration technique, the suspended layers can be restacked and transferred on a substrate.

2.5.2.1 Crystal Structure of Restacked MoS₂ and Intercalation Compounds

Randomly distributed MoS₂ flakes in water reorient themselves upon removing the water and drying. Previous XRD studies[43] show that MoS₂ in water has (100) and (110) peaks without the presence of the (00l) peak indicating that they are single layer (Fig.2.7). Upon removing the water slowly, MoS₂ layers reorient and new peak appears at

7.8 2θ degrees corresponding to the (001) peak and indicating that two water layers are stable between the MoS_2 layers (Fig.2.7). Then upon the drying process, intercalated MoS_2 (001) peak decreases and the (002) peak increases corresponding to restacked MoS_2 at 14.4 2θ degrees (Fig.2.7). This study shows that chemically exfoliated MoS_2 exhibit different surface behavior that attributed to the stable water molecule between MoS_2 layers under aqueous conditions.

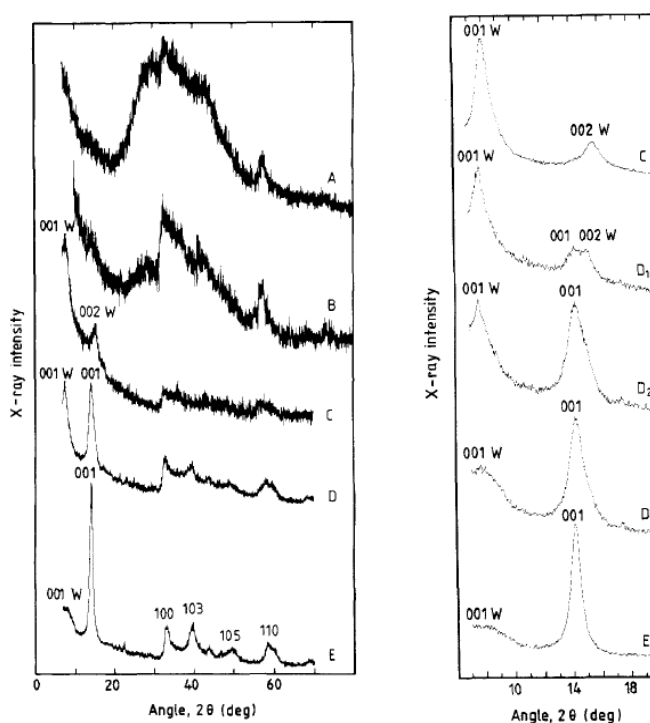


Figure 2.7 X-ray diffraction patterns of suspended single layer MoS_2 in water[43].

In addition to the water layer between MoS_2 layers, cationic guest species can be incorporated between layers of exfoliated MoS_2 [36], [46]. XRD and NMR analysis were conducted for intercalated compounds and their molecular structure were suggested as shown in Fig. 2.8[38]. It was stated that lithiation retained the negative charges on the

surface of exfoliated MoS_2 layers, attracting positive or neutral species on the surface of MoS_2 thereby.

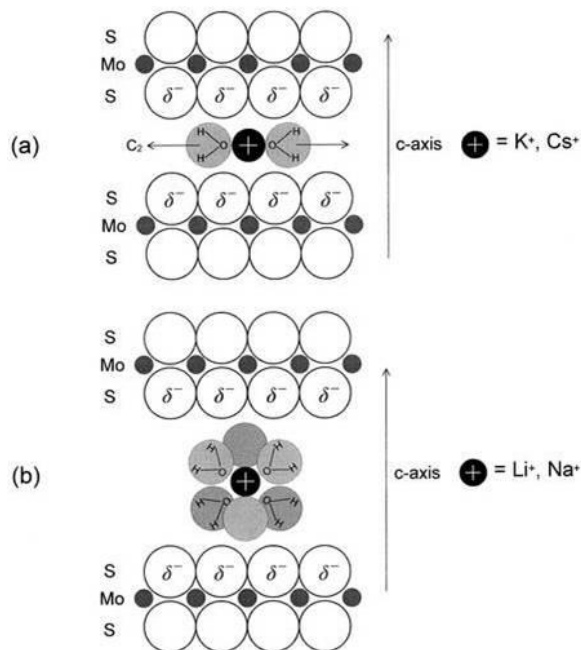


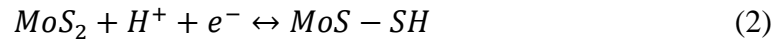
Figure 2.8 Schematics of the cation intercalated $A_x(\text{H}_2\text{O})_y\text{MoS}_2$ compounds[38].

To quantify the surface charges, the zeta potential was measured in exfoliated MoS_2 [32]. Previous analysis on exfoliated MoS_2 indicated that a zeta potential of -40-50mV is typical, which supports the negatively charged exfoliated MoS_2 surface hypothesis.

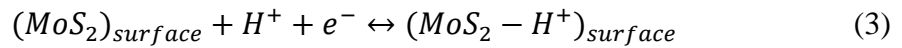
2.6 MoS_2 as Supercapacitor Electrode

Soon et al. reported the first MoS_2 based supercapacitor[18]. In that study[18], MoS_2 nanosheets were synthesized as supercapacitor electrode by thermal decomposition of tetrakis (diethylaminodithiocarbamate)molybdate(IV)[18]. Here, the MoS_2 nanowalls consist of sheets that are 500 nm in width and 100 nm in thickness. The dimensions of the

nanosheets are very thick in comparison to the thickness of single layers. The capacitance of nanowalled MoS_2 is around 100 F/g at 1mV/s scan rate, but it reduces to 20 F/g at 50 mV/s showing that the charge storage is limited by diffusion. Based on the electrochemical analysis, two charge storage processes were proposed for MoS_2 . Firstly, faradaic charge storage is responsible for high capacitance at slow scan rates



And secondly, protons or alkali cations adsorb on the surface of MoS_2 nanowalls which is not diffusion limited, resulting in



Eqn (3) designates a mechanism that is not a faradaic charge storage mechanism. Since the surface area of MoS_2 nanowalls is low, non-faradaic charge storage performance is also low.

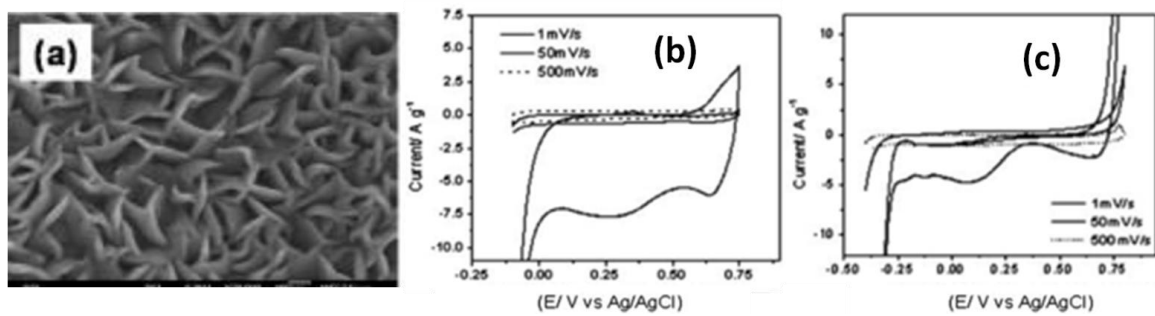


Figure 2.9. SEM image of MoS_2 nanofilm[18] (a), CVs at different scan rates in 0.5M NaOH (b), and H_2SO_4 .(c)

2.7 MoS₂ as a Piezoelectric Material and an Electrochemical Actuator

Recently, piezoelectric behavior has been observed in 2H phase monolayer transition metal dichalcogenides (LTMDs) [47], [48] such as 2H phase MoS₂. Piezoelectricity is an electromechanical coupling mechanism which has been used in a variety of actuators and sensors[49]. Such behavior is attributed to the lack of centrosymmetry in the crystal structure. The considerable large bandgap renders insulating or semi-insulating electronic behavior in the monolayers of LTMDs. For instance, crystal symmetry is broken in a monolayer 2H phase MoS₂ which has ~1.9 eV bandgap[50], and in consequence becomes an attractive material for piezoelectricity. However, the metallic 1T phase MoS₂ does not meet the requirements for piezoelectricity, due to its metallic behavior which is reported to be 10⁷ times more conductive than that of the 2H phase MoS₂[50], [51].

Unlike piezoelectricity, electrochemical actuators require highly conductive electrode for a better actuation performance. By incorporating MoS₂ to CNTs, 60 % of enhancement has been obtained[52]. However, 1T phase MoS₂ as a material for electrochemical actuator has remained unexplored.

The possible mechanisms for electrochemical actuator will be discussed in the Chapter 4. Regarding MoS₂ electrodes, either the intercalation of ions or change in bond length in the crystal structure might cause the electrochemical actuation behavior. On the other hand, there are very few studies reported on Mo-Mo or Mo-S change in bond length during ion adsorption[53], [54]. Alexiev et al. published a theoretical study on hydrogen adsorption on MoS₂ and according to their theoretical studies, hydrogen adsorption can

cause 1.4-4% Mo-S bond length increment [54]. Very recently, Mahmood et al. conducted an in situ synchrotron X-ray absorption spectroscopy on the charge storage in WS_2 . According to their studies, there is 1% W-W increase in bond length for the 1T phase of WS_2 during charge storage in H_2SO_4 electrolyte[53]. The schematic of change in bond length during surface redox reaction is depicted (Fig. 2.10). Since 1T phase of WS_2 has similar properties with 1T phase MoS_2 , we might expect similar behavior from 1T phase MoS_2 . Therefore, MoS_2 is also a prime candidate for substantial actuating due to electro-chemo-mechanical effects that remain to be unearthed.

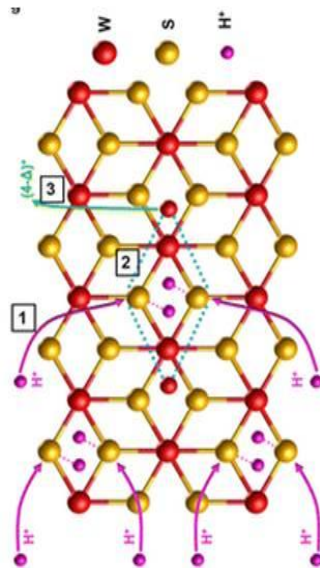


Figure 2.10. Illustration for surface redox charge storage on 1T phase WS_2 [53].

2.8 Mechanical Properties of MoS_2

Because of its anisotropic crystal structure, MoS_2 has different mechanical properties along in-plane and out-of-plane directions. Due to the strong covalent bonding, 2H phase MoS_2 has very high in-plane Young's modulus (~ 270 GPa)[28] and can sustain large deformations up to 11% before rupture[28]. After phase transformation, the

binding energies[50] of Mo and S atoms for 1T phase MoS₂ decreases which might lead to a slightly lower in-plane elastic modulus. While there are no experimental finding, theoretical studies suggested the in plane modulus of 1T phase MoS₂ to be 183 GPa[55].

For the restacked MoS₂ films, individual layers overlapped on top of each other. Consequently, weak Van der Waals bonds and coulombic interactions between layers lower the mechanical performance. Applying a lateral force will induce sliding between interlayers that determines the shear strength[56]. The shear strength of 2H phase MoS₂ is very low (1 MPa in vacuum) and increases with the presence of adsorbents which enhance the shear strength up to 59 MPa depending on the measurement conditions[56]. On the other hand, chemically exfoliated 1T phase of MoS₂ has negative surface charges and corrugated surface[37], which might increase the attraction between layers and results in higher shear strength. The mechanical behavior of thick films of 1T phase MoS₂ still remain to be studied in depth.

2.9 Chapter Summary

This chapter focused on the material aspect of this dissertation. A summary was presented on the different crystal structures of MoS₂ including naturally occurring stable 2H phase and metastable 1T phase; the phase transformation from semiconductive 2H phase to metallic 1T phase via organolithium chemistry; and subsequent exfoliation to monolayer. Several techniques to characterize the structure and chemical composition of different phases of chemically exfoliated MoS₂ were discussed. It was shown that phase engineering to tune the properties and render them attractive material for variety of applications such as electrode material in batteries and supercapacitors, catalyst for

hydrogen evolution reaction as well as piezoelectric material in energy conversion systems are within the realm of possibility.

Chapter 3. Electrochemical Supercapacitors

Electrochemical Supercapacitor (EC) devices are generally designed in a similar fashion as batteries [9]. An EC device contains two electrochemically active electrodes separated with a porous and insulating separator filled with electrolyte as shown in Fig. 3.1. Under an applied potential (V), charge storage occurs on the surface of the charged electrodes by polarizing the electrons and mobile ions (see Fig. 3.1). The corresponding potential curve of the charged electrode/electrolyte interface is depicted in Fig. 3.1b. Here, charge storage occurs only on the surface of electrode which has a thickness of 2-10 Å [9]. If such ionic interaction is purely electrostatic, such devices are called electrochemical double layer supercapacitor (EDLCs).

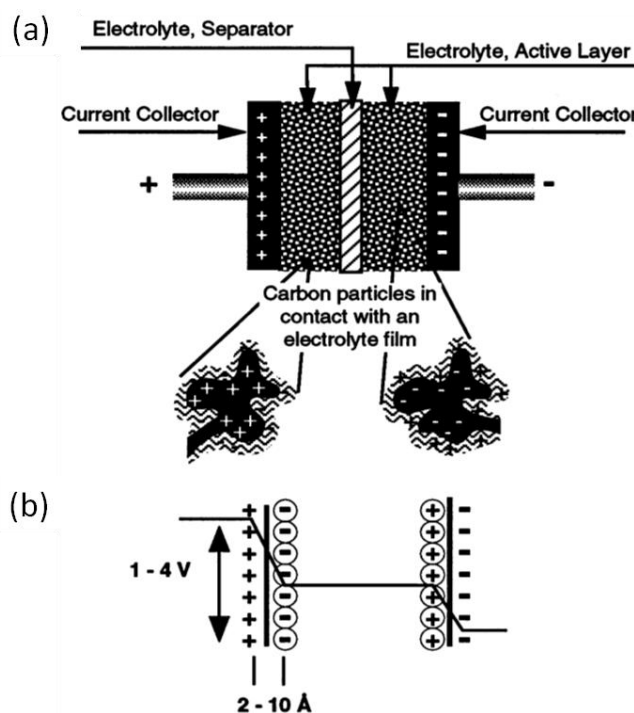


Figure 3.1. Principle of a single-cell double-layer capacitor (a) and illustration of the potential drop at the electrode/electrolyte interface (b) [9].

For EDLCs, the energy can be stored on the surface of highly porous and conductive materials. Porous materials such as graphene[7], [15], [16], [23], carbon nanotubes[57], [58] (CNTs), mesoporous carbon[59] and nanoporous gold[13] were studied for use as EDLC electrodes. For high charge storage capacity, materials require high surface area (up to 3000 m²/g) because the capacitance is proportional to the accessible surface area. According to previous studies, typical capacitance per unit area is around 21 μF/cm² for EDLC type materials[60]. For example, if all theoretical surface area of graphene (2630 m²/g) were accessible, expected theoretical capacitance in graphene based capacitors would be 550 F/g (Ref[60]).

On the other hand, if reversible charge transfer occurs on the surface of the electrode by surface redox reaction or electrosorption, the device is called a pseudocapacitor[61]. Materials exhibiting pseudocapacitive behavior are mostly comprised of transition metal oxides with multiple oxidation states that change during charging and discharging. RuO₂ thin film capacitors based on pseudocapacitive redox reactions offer very high storage capacities up to 2000 F/g [62] with excellent cyclability albeit expensive [3]. Alternatively, MnO₂ is one of the most studied pseudocapacitive materials because of its promising high charge storage capacity (1370F/g)[12] and its relatively low cost, but its low conductivity reduces the performance[63]. The potential capacitance values of pseudocapacitive materials are much higher than EDLCs despite their lower surface area. Typical charge storage capacity for pseudocapacitive materials is two orders of magnitude higher than EDLCs with the same surface area[4]. But due to the faradaic reaction, pseudocapacitors are not as stable as EDLCs for long term usage. In order to overcome low conductivity and stability issues, pseudocapacitive materials and

EDLC materials were mixed and hybrid systems were proposed. For example, MnO_2 films grown on nanoporous gold electrode[13] enables the usage of very thin pseudocapacitive MnO_2 with a high surface coverage on porous gold electrodes. Enhanced electronic conductivity and ionic diffusion path for ions through highly porous structures provide high performance hybrid capacitance (up to 600F/g) where the corresponding MnO_2 contribution to the charge storage is close to its theoretical capacitance, i.e. 1145F/g.

3.1 Supercapacitor Device Configuration

Commercial supercapacitors are designed in a similar fashion to batteries, with two active electrodes separated with ion permeable membrane as illustrated in Fig. 3.1. Unlike batteries, charge storage mechanism for each individual electrode is similar to a conventional capacitor. During charging of a supercapacitor device, opposite charges accumulate on the surface of cathode and anode, respectively. Considering each electrode as a capacitor, a supercapacitor device can be modeled as two capacitors connected in series[64]. Hence, the total capacitance of the supercapacitor is given by

$$\frac{1}{C_{total}} = \frac{1}{C_1} + \frac{1}{C_2} \quad (4)$$

where C_1 and C_2 are the capacitances of each electrode. If the capacitances of each electrode are the same, the total device capacitance is half of the individual electrode.

It should be noted that the capacitances of the supercapacitors are not constant and depend on charging and discharging rate. Therefore, when capacitance is defined for ECs, a term called specific capacitance is used with a specified operational rate (scan rate or charging/discharging current). Since the charge storage mechanism of ECs relies on

the ionic species in the electrolyte, time is a limiting factor due to the ionic diffusion and electrolyte conductivity. Therefore, ECs behave capacitively at lower frequencies, but resistively at higher frequencies due to the diffusion and the charge response delay. The rate performance of the supercapacitors can be improved by:

- (1) Using highly conductive and porous electrode,
- (2) Optimizing pore distribution on the electrode to improve ionic diffusion,
- (3) Lowering the distance between two electrodes by using a thin porous separator,
- (4) Using highly conductive electrolytes.

The most prominent reason for charge response delay is the resistance of the electrode material itself. For high power systems, a highly conductive material is required. Since capacitance and the internal resistance depend mostly on the electrode material, we will discuss the electrode materials for electrochemical devices will be discussed in what follows.

3.1.1 Supercapacitor Materials

Electrode materials are the most important element for supercapacitor devices because the capacitance of the electrode determines the overall capacitance of the device. Therefore, a variety of materials are proposed for supercapacitor electrodes in order to enhance supercapacitor devices. There are three types of materials being investigated for supercapacitor electrodes:

- (1) Porous carbon (activated carbon, carbon nanotubes, graphene)[65]
- (2) Transition metal oxides (RuO_2 , MnO_2 , NiO , Co_2O_3 , V_2O_5 , MoO)[66]
- (3) Conjugated polymers (polypyrrole, polyaniline)[67]

3.1.1.1 Carbonaceous Materials

Carbonaceous materials are attractive due to low cost, high conductivity, high surface area and high chemical stability in various electrolytes[65]. Carbon is particularly attractive because it can be engineered with various morphologies including carbon nanotubes (CNTs), graphene, activated carbon, and mesoporous carbon for use as supercapacitor electrodes. By using these morphologies, up to 3000 m²/g surface area can be achieved. Since the capacitance is proportional to the accessible surface area of the electrode, porous carbons are good candidate for the supercapacitor applications. Additionally, porous carbons are chemically stable in acidic, basic, neutral and organic electrolytes. This inertness provides highly stable device performance with wide potential ranges (up to 4V in ionic liquids) which enables very high energy density devices[60].

The charge storage mechanism in porous carbon is mostly based on electrostatic double layer formation on the electrode surface without any chemical reaction. The lack of chemical reaction on the surface yields high cycle stability ($\sim 10^5$). However, porous carbons have limited capacitance due to low specific surface capacitance (21 $\mu\text{F}/\text{cm}^2$). As stated earlier, even if the highest theoretical surface area were obtained in graphene, then the capacitance would be only 550 F/g which is much lower than the capacitance of pseudocapacitive materials[60].

In order to exploit the highest performance from porous materials, an optimization is required for pore size, pore shape, and pore distribution in the structure[68]. Besides accessible area enhancement, pseudocapacitive active spots can be introduced via chemical functionalization in addition to the double layer[59].

3.1.1.1.1 Pore and Channel Distribution

Ideally, the capacitance is expected to be proportional to the surface area, but experimental results show that the capacitance is generally lower for higher surface areas ($>2500 \text{ m}^2/\text{g}$), (Fig. 3.2). The discrepancy is believed to be due to some isolated pores that are inaccessible for charge storage. The optimum distribution of pores and channels in the structure are of great importance and simply maximizing surface area will not give the best results[14].

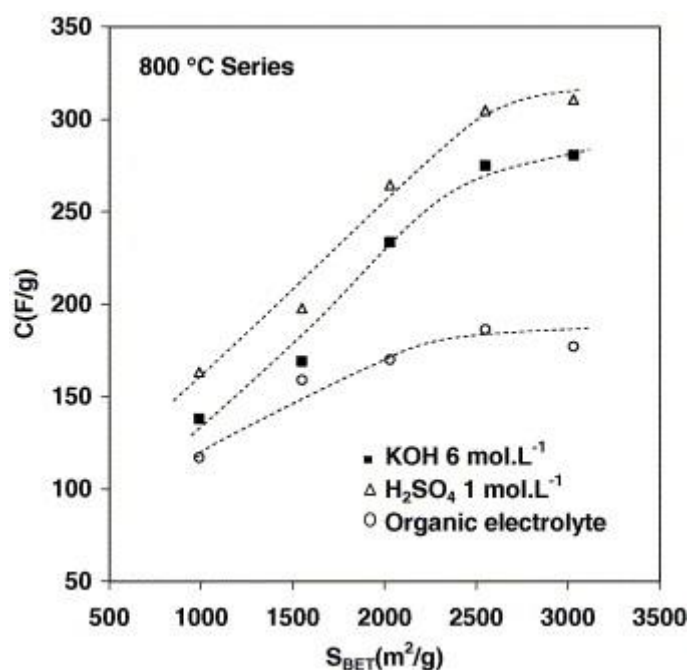


Figure 3.2. Gravimetric capacitance vs specific surface area in various electrolytes[14].

3.1.1.1.2 Pore Size and Shape Effect

Mesopores (2-50 nm pore size) have similar capacitance performance ($21 \mu\text{F}/\text{cm}^2$), but when pores are reduced below 2 nm, the capacitance increases sharply as shown in Fig. 3.3. The anomalous increment in the capacitance is based on the distortion of solvated ions and proximity of ionic centers to the charged surface[69]. The highest

capacitance is observed for pore size closer to the ion size. Specifically, the highest performance is observed with pore sizes close to 0.7 nm and 0.8 nm in aqueous and organic electrolytes [14]. Smaller and rounded pores have higher curvature and effective surface area decreases with the curvature. Slit-shaped pores provide the highest theoretical capacitance values [14].

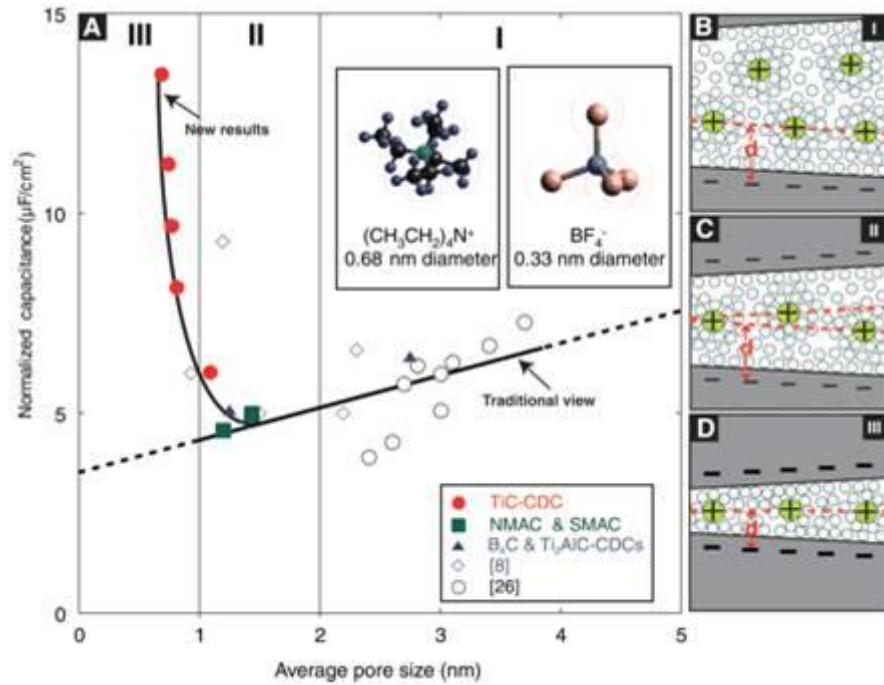
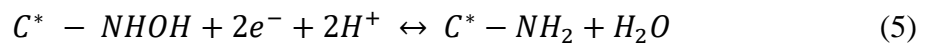


Figure 3.3. Pore size effect on the specific surface capacitance[69]

3.1.1.1.3 Functionalization

The capacitance can be further improved by chemical functionalization with active substances such as nitrogenated carbon. The enhancement of the capacitance is based on Faradaic pseudocapacitive charge storage. The following reaction represents pseudocapacitive charge storage for nitrogenated carbon surfaces (C^*)[70].



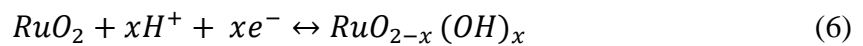
3.1.1.2 Transition Metal Oxides

The highest theoretical capacitances are reported for supercapacitor devices based on transition metal oxides[3], [13], [71]. If the theoretical capacitance performance is achieved, the supercapacitors may indeed complement batteries. Such high charge storage capacity in supercapacitors is possible because of multiple oxidation states of transition metals which can reversibly change during charge storage process via electron transfer[3]. Since the electrons are involved for the charge transfer, transition metal oxides are called pseudocapacitive materials (Faradaic). In order to exploit the material fully for charge storage, the electrolyte has to easily access all the surface of the material which requires high porosity similar to porous carbon. Various methods are employed such as nanostructurization[72], chemical modification[73], and incorporation of high surface area conductive materials[13] to develop high performance pseudocapacitive materials.

3.1.1.2.1 Ruthenium Oxide (RuO₂)

The most widely studied transition metal oxide is RuO₂. Because of its high capacitance, high potential range (1.4V), and high oxide conductivity and stability, RuO₂ is an ideal material for supercapacitor applications. Despite all these advantageous properties, RuO₂ is unlikely to see extensive commercial usage due to its high cost[3].

The exceptional high capacitance of RuO₂ relies on electro-adsorption of protons on the surface of RuO₂ via electron transfer through a change in the oxidation state of ruthenium (Ru²⁺ to Ru⁴⁺) in acidic electrolytes via



Here, the charge storage mechanism occurs on the surface of electrode, thus the specific area of the RuO_2 plays an important role. Various techniques were used to increase the accessible surface area of RuO_2 such as the synthesis of hydrous form of ruthenium oxide ($\text{RuO}_2 \cdot x\text{H}_2\text{O}$) [74] which enables specific capacitances as high as 786 F/g. Also depositing nanoscale size RuO_2 on a carbon surface enables specific capacitance up to 914 F/g¹⁹ which is much closer to the theoretical capacitance of RuO_2 . The crystallinity[75], particle size[76] and hydration amount[77] also play substantial role in the capacitive performance due to change on the surface area, ionic channels and conductance of the electrode.

3.1.1.2.2 Manganese oxide (MnO_2)

Another promising transition metal oxide is MnO_2 thanks to its high charge storage capability, relatively high potential range, relative abundance and low cost[78]. Although it has high theoretical capacitance (1300 F/g), its low conductivity (10^{-5} S/cm) limits direct usage as a supercapacitor electrode. In order to overcome the conductivity issue and obtain high capacitive performance, chemical modification[73] and hybrid systems[13] were proposed.

Thanks to having multiple oxidation states, MnO_2 can have variety of morphologies such as nanowires[79], nanorods[80], nanobelts[81]. These one dimensional morphologies improve the charge storage performance by providing high surface area. Also different crystal structures[82]–[84] of MnO_2 including α -, β -, γ - MnO_2 phases provide tunnel shape pores in the crystal structure. Another crystal structure, δ - MnO_2 has a layered structure enabling higher accessible surface area for charge storage and better performance comparing other crystal forms[85].

For better ionic conductivity, a hydrous state of MnO_2 [71] is proposed similarly to RuO_2 . However, the crystallinity of the material has to be optimized to achieve higher electronic conductivity and higher ionic conductivity together. In order to compensate for the low conductivity, more conductive materials[13], [86], [87] such as CNTs, graphene, nanoporous gold were incorporated into thin MnO_2 , all of which result in higher energy storage and power performance.

3.1.1.2.3 Conjugated Polymers

Conjugated polymers also show high capacitive behaviour similar to transition metal oxides. In addition to their high charge storage capacity; low cost, high conductivity and a high voltage window makes conjugated polymers attractive as supercapacitor electrode[88]. The only problem with these materials is their poor stability due to mechanical degradation[89].

Polyaniline (PANI)[90], polypyrrol (PPy)[91], polythiophene (PTh)[92] and their derivatives[93] are typical polymers studied as supercapacitor electrode. The high charge storage capability of these materials is based on reversible Faradaic redox reaction on the polymer backbone. Ions inserted throughout the bulk polymer structure during the charging process and generate delocalized “n” electrons on the polymer chain by doping it with negative or positive charges. This process does not cause any structural change; therefore, doping/de-doping of the conjugated polymers is highly reversible. On the other hand, the insertion and de-insertion of ions into the polymer causes significant swelling and shrinking during charge storage which results in mechanical degradation and lowers the stability performance (70% after 1000 cycles for PANI)[94].

In order to enhance the stability of the conjugated polymers, nanostructured polymers were fabricated such as PANI nanowhiskers. Having nanostructured conformation balances the volumetric changes and also improves the ionic diffusion process by enhancing the channels. High cycle stability is observed with nanowhisker PANI (95% capacitive retention after 3000 cycles)[95].

Another approach for improving the cycle stability of conjugated polymers entails fabricating hybrid structures with carbonaceous materials such as CNTs, graphene. These hybrid structures show improved conductivity, mechanical stability and processability. For example, PANI/CNTs hybrids exhibits such high capacitances (1030F/g) with high cycle stability, i.e. 95% retention after 5000 cycles [96].

3.1.2 Electrolytes

The electrolyte is the liquid medium containing mobile ions for charge transfer and storage. The type of electrolyte is important for charge storage because the applied potential range is determined by the properties of electrolyte such as its chemical stability. Also, the potential range has a substantial effect on the stored energy density. That is so, since energy density, E , [66, p. 41] is given as

$$E = \frac{1}{2}CV^2, \quad (7)$$

where C is the capacitance and V is the potential range of the device. Secondly, low internal resistance is required for high power density devices[66, p. 41]. The conductance of the electrolyte has also substantial effect on the supercapacitor performance in terms of power density. Power density, P , is,

$$P = \frac{1}{4R_s}V^2 \quad (8)$$

where R_s is internal resistance of the device. There are three types of electrolytes: (i) aqueous electrolyte, (ii) organic electrolyte and (iii) ionic liquid.

3.1.2.1 Aqueous electrolytes

H_2SO_4 , KOH, K_2SO_4 and Na_2SO_4 are common aqueous electrolytes used in supercapacitors due to their high ionic conductivities. The capacitance of the materials in aqueous electrolyte is also higher than organic electrolytes. The high conductivity and high capacitive behavior in aqueous electrolyte is due to the smaller hydrated ionic radius. Smaller hydrated ions can move faster due to electrophoretic effect and show higher ionic conductivity[97]. Also they can diffuse more into the smaller pores and result in higher capacitive performance. However, the potential window (1.15V) is limited in aqueous electrolytes due to water splitting. Since the energy density and power density depend on the potential window as stated in Eqn (7) and Eqn (8), power densities and energy densities in aqueous electrolytes are lower as compared to organic electrolytes and ionic liquids.

3.1.2.2 Organic electrolytes

In order to increase the potential range of a capacitor, organic solvents are used such as acetonitrile (MeCN) or propylene carbonate (PC) with quaternary ammonium salts or alkyl ammonium salts such as tetraethylammonium fluoroborate (TEA BF_4). They provide better potential range up to 3.5 V. However, problems with handling of organic solvents limit their usage in supercapacitors as they are highly toxic and volatile. Also 3-5 ppm water content in these electrolytes decreases the performance of organic electrolytes by reducing the potential window[66].

3.1.2.3 Ionic liquids

Ionic liquids are molten salts at room temperature and they can be used without a solvent as electrolyte[98]. The lack of solvent improves the potential range up to 6V, and enables the fabrication of EC devices fabricated from ionic liquids that have the highest energy density. However, ionic liquids have lower conductivities compared to aqueous and organic electrolytes due to their high viscosity at room temperature. In order to decrease the viscosity and increase the conductivity, charge storage needs to be performed at higher temperatures (60°C)[7].

3.1.3 Separators

For an EC device to have minimal internal resistance, the distance between two electrodes is made as short as possible. This is accomplished by use of a separator material between the two electrodes which must be electrically insulating and ionically conductive. It also provides a medium for mobile ions (electrolyte) to move in between two electrodes. There are two type of separators commonly used. The first are porous and insulating materials such as porous polymers (polypropylene)[7] or glasses[99]. The second type are gel electrolytes[100], [101], which can serve as both the separator and the electrolyte. Gel electrolytes enable thinner (10 μm) separator fabrication while typical porous polymer thickness is 25 μm [100].

3.2 Electrochemical Characterization Techniques

Capacitance (C) is the ability of a material to store charge (Q) per unit electrical potential (V). The stored charge can be determined using standard electrochemistry techniques [61] such as cyclic voltammetry, galvanostatic charge-discharge and

electrochemical impedance spectroscopy (EIS). In order to conduct these measurements, a potentiostat and a frequency analyzer are required.

There are two different configurations of the electrochemical cell setup for analysis: (i) two electrode and (ii) three electrode configurations[66]. For complete supercapacitor devices with two active electrodes and a separator, the two electrode configuration is used. The capacitance measured on such configurations show the device capacitance, but does not provide the charge contribution from each individual active electrode directly. In order to characterize each individual electrode, the three electrode configuration is used. In this configuration, one active electrode (half cell) is used with two additional electrodes that are called the reference electrode and the counter electrode, respectively. The reference electrode is used to fix the potential of the system. Depending on the electrolyte type, there are various types of reference electrodes such as Hg/HgO for basic solutions and Hg/HgCl for acidic solutions. In order to complete the cell circuit, a counter electrode is used, which is chemically inert and electronically conductive, such as platinum or graphite.

3.2.1 Cyclic Voltammetry (CV)

Cyclic voltammetry is a type of potentiodynamic measurement technique used for characterizing the electrochemical behavior of materials[61]. In this method, the electrode potential is swept reversibly between two potentials and the resulting current is measured. The resulting I-V curve is called the cyclic voltammogram (CV). Typical CV curves of an ideal capacitor and capacitor/resistor are shown in Fig. 3.4. For resistor materials, current increases linearly by increasing the potential difference and the slope of

the curve give the resistance of device from which the resistivity of the material is obtained. Contrarily, ideal capacitors exhibit rectangular CV curves. The nature of the rectangular curve is based on the infinite resistance of ideal capacitors and the process of charge accumulation under applied DC potential. Instead of current passage from one electrode to the other, the charges accumulate on top of each electrode when a potential difference is applied to the capacitor. Then, the current initially increases sharply and saturates due to the charge storage capacity of the device. Similarly, when the potential sweep is reversed, the same trend is observed. The area in the rectangular curve corresponds to the stored charge in the capacitor.

Stored charge (Q) is proportional to the potential difference (V) between electrodes[61], where the constant of proportionality is the capacitance (C), as shown in Eqn (9)

$$Q = CV, \quad (9)$$

By taking the derivative of this equation with respect to time, one obtains

$$\frac{dQ}{dt} = C \frac{dV}{dt} \quad (10)$$

where the first expression on the left hand side of Eqn (10) denotes the so-called changing current I and the last expression denotes scan rate of the potential v , such that

$$I = Cv \quad (11)$$

Per Eqn (11), the current is proportional to the time rate of potential change with time (scan rate) and the slope gives the capacitance. Typical CV curves for an ideal capacitor (double layer), capacitor with finite resistivity and pseudocapacitor are shown in Fig. 3.4.

The internal resistance and the ionic diffusion related to resistance cause a deviation from rectangular CV curves. Also, any Faradaic reactions cause a distinct peak in addition to the rectangular CV curve as shown in Fig. 3.4.

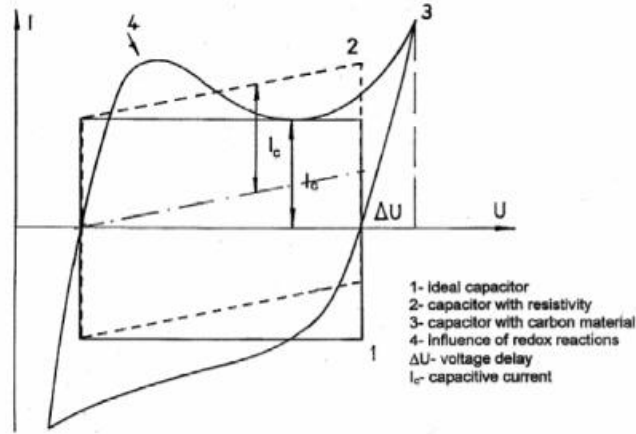


Figure 3.4. Comparison of ideal and real cyclic voltammograms [102]

The area inside of the CV curve gives the capacitance of the material. By using the Eqn (12,13) gravimetric and volumetric capacitances can be simply calculated from

$$C_g = \frac{\int IdV}{vmV} \quad (12)$$

where C_g is the gravimetric capacitance (F/g), I is the current (A), v is the scan rate (V/s), m is the mass (g), V is the potential range, and

$$C_v = C_g \times \rho \quad (13)$$

where C_v is the volumetric capacitance (F/cm³) and ρ (g/cm³) is the density of active material.

3.2.1.1 Randles-Sevcik Equation

EDLCs have rectangular CV curves similar to ideal capacitor and Eqn (11) can be conducted for EDLCs. However, additional reversible peaks arise for pseudocapacitive materials which correspond to oxidation and reduction processes for a reversible redox reaction. Typical CV curves for a reversible redox reaction and a pseudocapacitor are shown in Fig. 3.5. For a faradaic reaction, the peak current corresponding to charge transfer is calculated by using the Randles-Sevcik equation[103]

$$I = 2.69 \times 10^5 n^{3/2} A D^{1/2} \nu^{1/2} C , \quad (14)$$

where I is the peak current, n is the number of electrons transferred, D is the diffusion coefficient, A is the electrode area, ν is the scan rate and C is the concentration of electrolytes. Equation (14) shows that peak current is proportional to the square root of the scan rate ($\nu^{1/2}$) for faradaic reactions, whereas for electrostatic charge storage, current is directly proportional to the scan rate (ν). These two current and scan rate relations Eqn(11) and Eqn(14) show that the contributions of charge storage from electrostatic double layer (ν) or faradaic reaction ($\nu^{1/2}$).

3.2.2 Galvanostatic Charge/discharge Complementary

Capacitance calculated from CV measurements is sometimes inaccurate, because it does not account for the loss from the internal resistance. For an actual capacitance measurement, galvanostatic charge/discharge measurement provides better information. In this technique, the electrode is charged with a constant current rate and the potential change is recorded with time according to the reference electrode. An ideal capacitor has

a triangular galvanostatic charge discharge curve as shown in Fig. 3.5. Capacitance is calculated from discharging time according to the following equations.

$$C_g = \frac{I \times t}{m \times V} \quad (15)$$

and

$$C_v = C_g \times \rho \quad (16)$$

where C_g is the gravimetric capacitance (F/g), C_v is the volumetric capacitance (F/cm³), I is the current (A), m : mass (g), V is the potential range, t is the discharging time and ρ (g/cm³) is the density of active material.

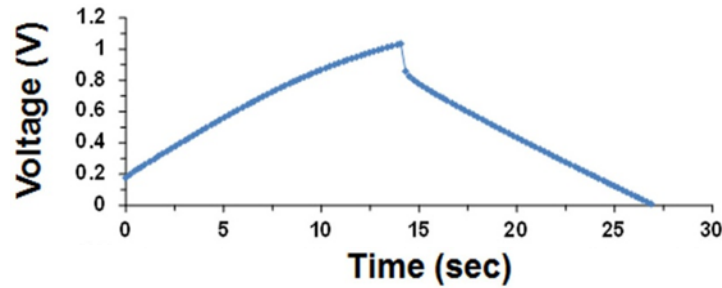


Figure 3.5. Galvanostatic charge / discharge curve[104].

In actual devices, the internal resistance of the system results in a sudden potential fall during discharging as shown in Fig. 3.5. For ultimate supercapacitor, low internal resistance is required because a high internal resistance reduces the discharging time which reduces the capacitance of the device, in addition to limiting the operational potential. Since energy density and power density are proportional to the square of the potential window, the effect of the internal resistance is vital. Furthermore, power density

is also inversely proportional to the internal resistance. For high energy density and power density supercapacitor devices, low internal resistance is crucial.

3.2.2.1 Energy Density / Power Density Calculations from Galvonastatic Measurements

The energy density and power density of the supercapacitors are calculated according to the following equations:

$$E(Wh/g) = \frac{0.5C_T\Delta V^2}{3600} \quad (17)$$

$$E_v(Wh/cm^3) = E \times \rho \quad (18)$$

$$P(W/g) = \frac{E \times 3600}{t_{discharge}} \quad (19)$$

$$P_v(W/cm^3) = P \times \rho \quad (20)$$

where C_T is the total capacitance of the two-electrode cell, ΔV is the effective potential range during discharging process, $t_{discharge}$ is the discharging time, ρ is the density of the electrode, E is the energy density and P is the power density.

3.2.3 Electrochemical Impedance Spectroscopy

Electrochemical impedance spectroscopy (EIS) gives more detailed information about the capacitive and resistive components of supercapacitor devices[105]. While the CV technique only provides the capacitance and the galvanostatic charge discharge technique provides additionally the internal resistance of the system, the overall

electronic components of a supercapacitor device are more complicated than just a capacitor and a resistor. Therefore, the EIS technique is more useful to obtain more information about each component of the device.

As discussed in earlier chapters, the specific capacitance changes with the speed of the measurement due to the diffusion of ionic species in the electrolyte and the porous electrode. To introduce the time into the measurement, an alternating current (AC) probe is used. In this context, the term impedance replaces resistance in the I/V relationship and results in

$$Z(\omega) = \frac{V(\omega)}{I(\omega)}; \omega = 2\pi f. \quad (21)$$

Typically, the impedance of a system[105] is measured by applying low amplitude alternative voltage ΔV to a steady potential V_s with $\Delta V(\omega) = \Delta V_{max}e^{j\omega t}$, where ω is the angular frequency. This applied potential leads to sinusoidal output current with $\Delta I(\omega) = \Delta I_{max}e^{j(\omega t + \varphi)}$ where φ is the phase difference between the current and voltage. Since the impedance is given by

$$Z = \Delta V / \Delta I, \quad (22)$$

One obtain Z in phasor notation (exponential coordinates) as

$$Z = Z(\omega)e^{-j\varphi} \quad (23)$$

which can be expressed as (Using Euler's theorem)

$$Z(\omega) = Z'(\omega) + jZ''(\omega) \quad (24)$$

where Z' is real part of impedance, Z'' is imaginary part of impedance, ω is the angular frequency and $j^2 = -1$. By using the real and imaginary parts of the impedance as function of frequency, Nyquist plots can be obtained to show the frequency response of the supercapacitor electrode[105].

Typical Nyquist plots are shown for an ideal capacitor in Fig. 3.7a that is modeled by a capacitor and a resistor in series (Fig. 3.6b), and other combination of capacitors and resistors (Fig. 3.6c, 3.6d). For real supercapacitor systems, a diffusion element called the Warburg term is also introduced to model diffusive species in the system (see Fig. 3.6e). By using such elements, equivalent circuit models can be developed to characterize and model supercapacitor systems. And, by modeling a quasi electrochemical system with EIS, the double layer capacitances, faradaic capacitances, ohmic resistances, and faradaic resistances with diffusion components (Warburg element) of the system can be obtained. Such AC measurements are typically carried in the 0.01 Hz and 100 kHz range.

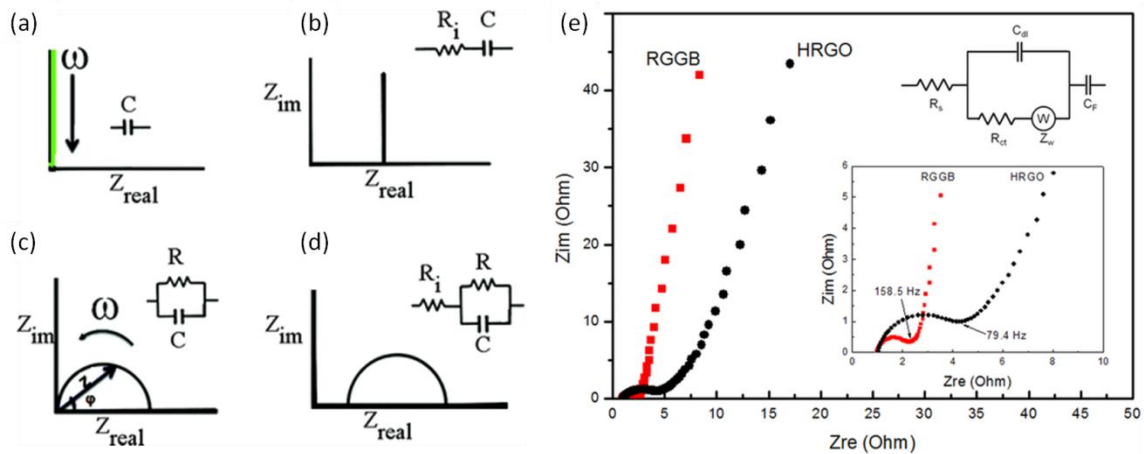


Figure 3.6. Equivalent circuit models and equivalent Nyquist plot are shown for capacitor (a), a capacitor and a resistor in series (b), a capacitor and a resistor in parallel

(c) and a resistor in series with another resistor and capacitor in parallel (d).[106] For electrochemical systems, the Warburg element is included as shown for graphene supercapacitor(e) [107].

3.3 Charge Storage Mechanisms

As mentioned previously, there are two distinct charging mechanisms of ECs and these mechanisms classify the type of ECs. If the charge storage occurs on the electrode/electrolyte interface with pure electrostatic attraction without any electrochemical reaction (i.e., non-Faradaic), it is called electrochemical double layer capacitor (EDLC). If an electrochemical reaction occurs on the electrode/electrolyte interface during charging and discharging, the mechanism is called pseudocapacitive charge storage (Faradaic). Based on these mechanisms, ECs are classified as:

- (1) Electrochemical double layer capacitors (EDLC)
- (2) Pseudocapacitors

3.3.1 Electrochemical Double Layer Capacitors

In electrochemical double layer capacitors (EDLCs), charge accumulation occurs on the electrode/electrolyte interface via polarization under applied potential. The charging mechanism in EDLC based supercapacitors is purely electrostatic as in conventional capacitors. Fig. 3.8 compares and contrasts conventional and EDLC-type supercapacitors.

Conventional capacitors are made of two metal plates separated with a dielectric medium[61]. The stored charge in such capacitors is

$$C = \varepsilon \frac{A}{d}, \quad (25)$$

where C is the capacitance, ε is the permittivity of the medium, A is the area of the plate and d is the distance between the two plates as illustrated in Fig. 3.7a. Capacitance is proportional to the area of the metal plate and inversely proportional to the thickness of the dielectric medium. In order to increase the capacitance drastically, either the area of the plate can be increased or the plate separation can be decreased for a given medium. However, the capacitance enhancement with dimensional change were restricted by fabrication limitations and the tunneling effect[108]. Due to these limitations, typical conventional dielectric capacitors have capacitances on the order of microfarad per gram.

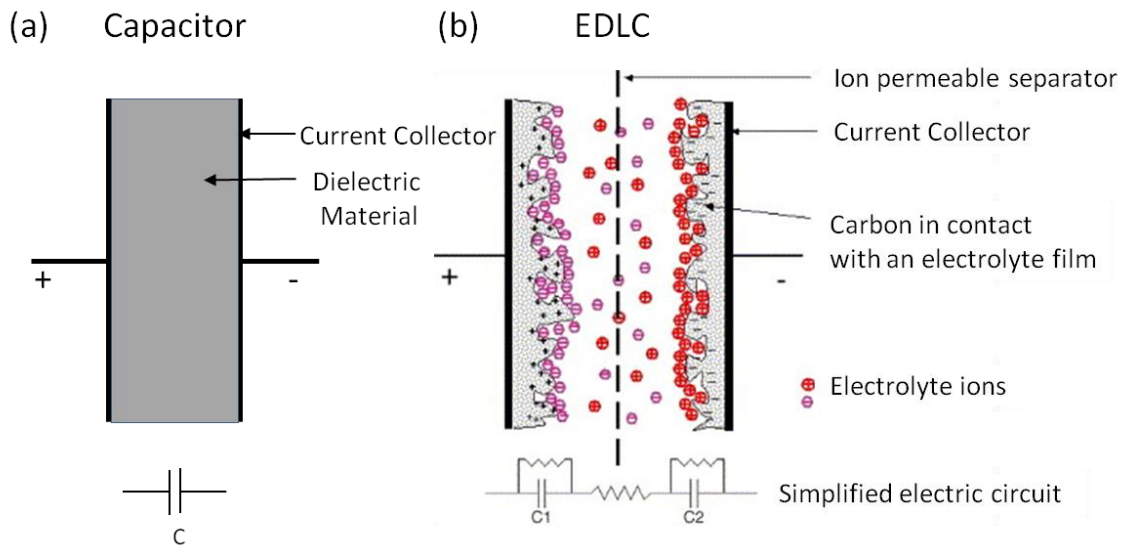


Figure 3.7. Schematics of conventional capacitor (a), and electrochemical double layer capacitor (EDLC) (b).[9]

Electrochemical double layer capacitors (EDLCs) have similar electrostatic charge storage mechanisms, but capacitances reaching up to 300 F/g which is five orders of magnitude higher compare to the conventional capacitors[109]. The enhancement of the capacitance originates from the charge storage mechanism of the electrochemical double

layer capacitance (EDLCs). During charge storage, no chemical reaction occurs on the electrodes (non-Faradaic) which enable very long service life. Next, the salient aspects of the electrical double layer theory will be elaborated on to place the ensuing discussion on EDLC's on a solid footing.

3.3.1.1 Double Layer Phenomenon and Models

Ideally when a charged, conductive surface is immersed in an electrolytic solution, it attracts the counter ions and repels the co-ions [110]. Also due to dipole interactions of the water molecules, a molecular water layer (~ 0.3 nm) separates the two surfaces which behaves as a dielectric medium in between a charged surface and counter ions (Figs. 3.7b, 3.8). This phenomenon is called double layer.

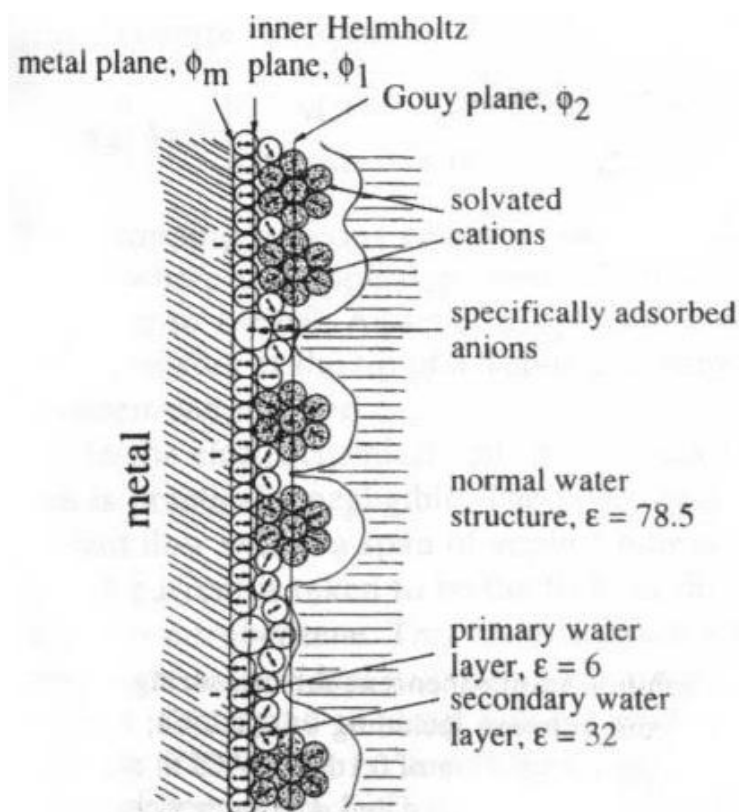


Figure 3.8. Schematic representation of a double layer on an electrode (BMD) model [110].

Double layer is an inevitable phenomenon on charged surfaces in electrolytic environment such as colloidal systems[111] and biological systems[112]. This mechanism enables small particles to be stably or metastably dispersed in a liquid medium without coagulation. Normally particles attract each other with van der Waals forces, but electrostatic repulsion of double layers of counter ions may cancel the attractive forces. For instance, milk is a mixture of water and butterfat globules[112]. Double layers surround fat droplets and prevent coagulation to the butter inside of the milk. The theory of double layer is given by DLVO theory [113] (Derjaguin, Landau, Verwey, Overbeek) and will be briefly discussed for completeness and continuity in the presentation although it is not the major forces of this study.

The thickness of the double layer, which is also known as the Debye length, depends on the concentration of the electrolyte[113]. Typical electrolyte concentration is 1M electrolytes, which leads to 0.3 nm double layer separation which is only one layer of water molecules between the charged plate and ions in the case of aqueous systems. Since water molecules behave as a dielectric material (relative permittivity of water, $\epsilon_r = 30 - 80$), the structure of the double layer can be used as capacitor. By thinning the separation of two charged plates to 0.3 nm, the capacitance can be increased by three orders of magnitude. However, capacitance calculations due to double layer formation are not as straightforward. Various double layer formation models have been proposed which are described concisely below.

3.3.1.2 Helmholtz Double Layer

Hermann von Helmholtz discussed the double layer theory for the first time in 1857 [114]. He realized that when a charged metal plate was dipped into an electrolyte, co-ions were repelled from the charged plate and counter ions were attracted to the surface of charged plate. He estimated the capacitance from first double layer model as

$$C = \frac{\partial \sigma}{\partial V}, \quad (26)$$

and

$$C = \varepsilon \frac{A}{4\pi d}, \quad (27)$$

where C is the capacitance, σ is the charge density, V is the applied potential, A is the surface area, ε is the dielectric constant of the medium between two charged layers, and d is the separation between two layers of charged electrode surface/center of the ionic layer.

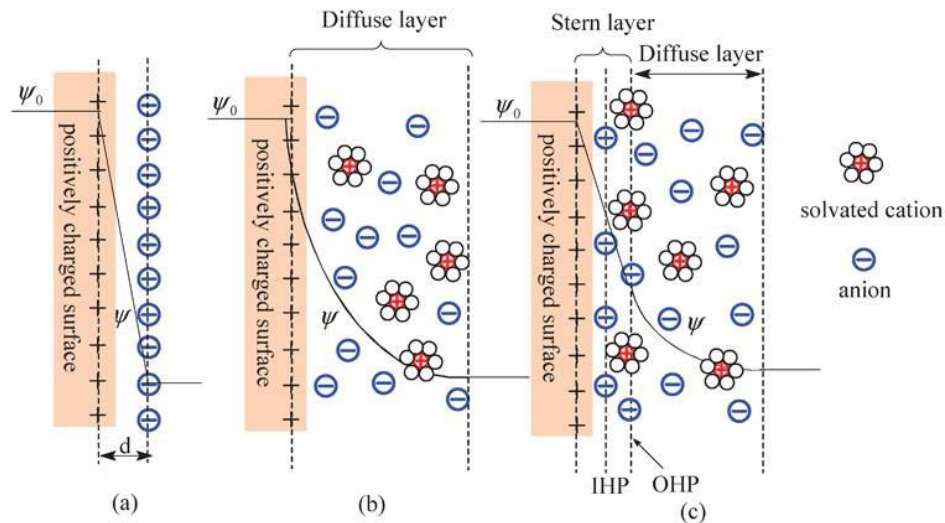


Figure 3.9. The illustration for **a)** Helmholtz model, **b)** Gouy-Chapman model, **c)** Stern and Grahame model[65].

He proposed that charge accumulation is completely electrostatic without any chemical reaction during double layer formation. In the Hemholtz model, the distribution of counter ions are well aligned on the surface of the charged surface as illustrated in Fig. 3.9a.

3.3.1.3 Gouy-Chapman Model

In 1910s Louis Georges Gouy[115] and David Leonard Chapman[116] realized that the capacitance of the double layer is not constant and depends on the applied potential and ionic concentration. They asserted that thermal motions make ions deviate from well ordered distributions on the charged surface. In order to solve this ambiguity, they introduced a diffuse layer concept to the double layer theory. By using Poisson's equation, the charge density was recalculated. Also the Boltzman equation was used for charge distribution in the electrolyte. According to this theory, the electric field decays exponentially from the charged surface through the electrolyte and ions distributed according to the electric field.

3.3.1.4 Stern model (1924)

The Stern model[117] was proposed because of the failure of Gouy-Chapman model at highly charged surfaces. They introduced an immobile layer (Stern layer) on the surface of charged plate as illustrated in Fig. 3.9c. In this model, the double layer is combination of the Stern layer and the diffuse layer.

3.3.1.5 Grahame model (1947)

Grahame proposed a model to account for the effect of specifically adsorbed ions on the surface[118]. According to his model, some ions or uncharged species can penetrate the Stern layer. If ions lose their solvation shell in close proximity to the charged electrode, they will be adsorbed specifically on the surface of the electrode as illustrated in Fig 3.9c. The double layer theory loses its validity for adsorbed ions and later the Grahame model turned out to be the base for such pseudocapacitive charge storage. In this model, the double layer was divided to three parts as illustrated in Fig. 3.9c. The inner Helmholtz layer comprised of uncharged solvent molecules and specifically adsorbed ions on the surface of electrode. The outer Helmholtz layer is the plane where the centers of the first solvated ions are closer to the electrode. Here, the diffuse layer is the region between bulk and outer Helmholtz layer.

3.3.1.6 Bockris/Devanathan/Müller (1963)

In this model, the contribution of solvent molecules on the capacitance was clarified[119] as depicted in Fig. 3.8. The relative dielectric permittivity of the water molecule on the charged surface is different than bulk water due to reorientation along the electric field. The relative dielectric permittivity of the first water layer in the inner Helmholtz layer is 6, second water layer is 32 and bulk water is 78.5. This correction to the dielectric constant provides more accurate capacitance calculation from modeling. Currently, the BDM model is still deemed valid.

3.3.1.7 Failure of Classical Double Layer Model (BDM)

Classical double layer model (BDM model) is valid for pores larger than 2 nm because of the need for space in double layer formation. According to previous studies[9], the capacitance is proportional to the accessible surface area. However, when pores are smaller than 2 nm, the linear relation between surface area and capacitance does not hold[69]. For such subnanometer pores, the normalized capacitance with surface area increases sharply due to confinement of ions. Here, the anomalous increase in the capacitance is attributed to the desolvation of ions. The deviation from linearity can be verified in Fig. 3.3 where one observes the steep increase in normalized capacitance 300% for pore sizes in the vicinity of 1 nm.

3.3.2 Pseudocapacitors

Electrostatic attraction of charges leading to adsorption of ions on the electrode surface cause the double layer theory fails (Grahame model)[118]. Under these circumstances, a charge transfer occurs across the double layer and it raises the capacitance 10-100 times than that of the double layer capacitance[3]. This behavior is observed in noble metals[13], transition metal oxides and conjugated polymers. This mechanism is called pseudocapacitance due to the charge transfer (Faradaic) that is unlike the double layer theory (non-Faradaic). The charge transfer occurs via:

- (1) Adsorption on noble metals[13] such as H adsorption on Pt and gold (see Fig. 3.10c)
- (2) Surface redox reaction on transition metal oxides as observed in RuO_2 [3] (see Fig. 3.10b)

(3) Electrochemical doping/de-doping on conductive polymer based electrodes.

In terms of the faradaic reaction, pseudocapacitors are reminiscent to rechargeable batteries, but they have very high cycle stability ($\sim 10^4$) unlike rechargeable batteries ($\sim 10^3$). The main reason for low cycle stabilities in rechargeable batteries is the phase transformation associated with the intercalation process during charging/discharging[120]. On the other hand, charging/discharging does not cause any structural changes in the electrode of a pseudocapacitor.

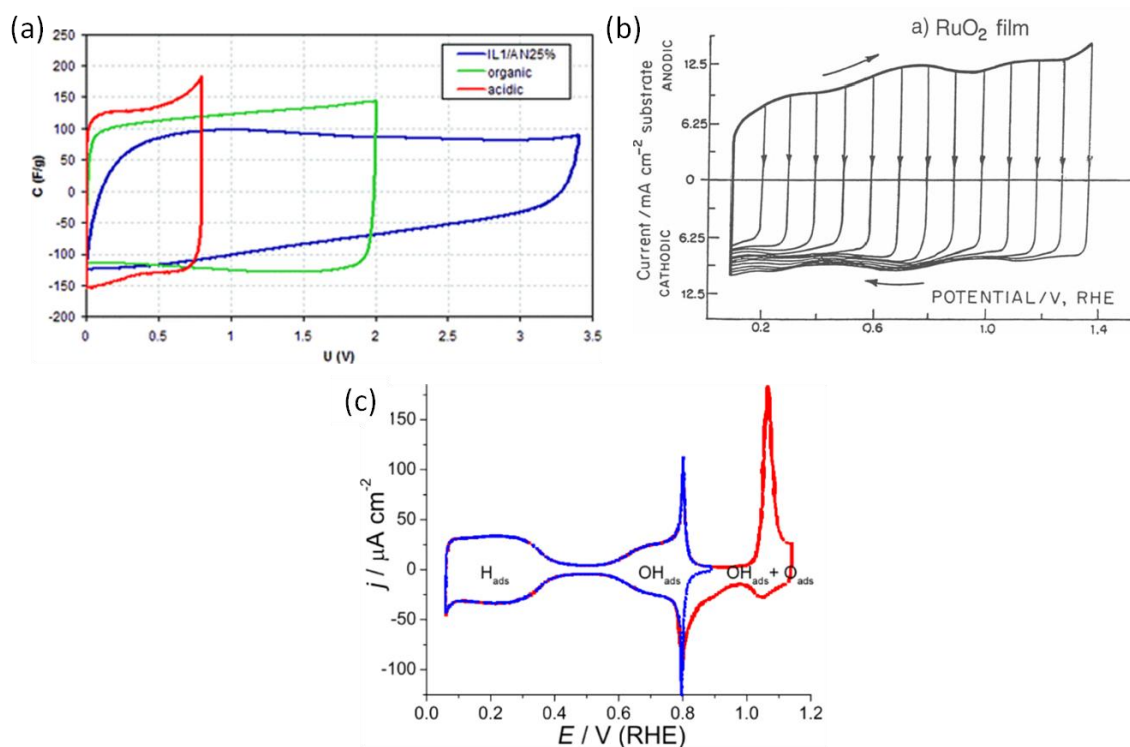


Figure 3.10. CV curves for porous carbon in acidic, organic and ionic electrolytes (EDLC)[64] (a), for RuO₂ film (Redox)[61] (b), and for Pt (Adsorption)[121] (c).

In order to show the difference between EDLCs and pseudocapacitive materials, typical cyclic voltammetry (CV) curves are shown in Fig. 3.10. The CV curve for EDLC is rectangular and represents ideal capacitor behavior in aqueous, organic electrolytes and

ionic liquids with increasing potential ranges (see Fig. 3.10a). Besides, hydrogen adsorption on platinum results in sharp peaks (see Fig. 3.10c) corresponding to charge transfer. Similarly, RuO_2 has smoother peaks corresponding to the change in the oxidation state of RuO_2 (Fig. 3.10b). The observed peaks in Figs. 3.10 (b,c) occurred over a certain potential range that signifies a potential dependent mechanism due to charge transfer by adsorption. The inner rectangular shape in Figs. 3.10 (b,c) corresponds to double layer charge storage, which suggested that pseudocapacitive materials are comprised of a double layer and pseudocapacitive charge storage mechanism. Generally, pseudocapacitive materials have ~5-10% double layer charge storage.

Typical charge contribution per atom of accessible surface areas in various electrochemical systems as[61]:

- Electrochemical double layer (EDLCs): $0.17\text{-}0.2\text{ e}^-/\text{atom}$
- Pseudocapacitors: 2.5 electrons per electroactive material (redox),
1 electron per noble metal atom (adsorption)
- Batteries: 1-3 electrons per atom or molecules depending on the oxidation states of reagents and products.

3.3.2.1 Pseudocapacitance Models

Unlike the sole electrostatic attraction of ions, there is charge transfer occurring via adsorption/desorption in pseudocapacitors[61]. In order to calculate the current associated with adsorption, the degree of surface coverage of the adsorbed ions needs to be calculated using sorption isotherms[3]. Sorption isotherms describe the thermodynamic

equilibrium governing the adsorption of ions on the surface of a material at constant temperature under isobaric conditions. The ratio of surface coverage (θ) and uncovered surface ($1-\theta$) for adsorption/desorption processes is given by

$$\frac{\theta}{1-\theta} = K C e^{\frac{VF}{RT}} \quad (28)$$

where K is the constant, C is the concentration of ions and F is the Faraday constant. Similarly the same formula can be used for the redox process by using the fraction of oxidized (X) and reduced ($1-X$) species instead of surface coverage (θ) and uncovered surface ($1-\theta$). Then the capacitance can be derived from

$$C_{\phi} = q_1 \left(\frac{d\theta}{dV} \right) \quad (29)$$

and

$$C_{\phi} = \frac{q_1 F}{RT} \cdot \theta(1 - \theta) \quad (30)$$

which indicates a peak having the maximum capacitance at $\theta = 0.5$ as shown in Fig. 3.12a.

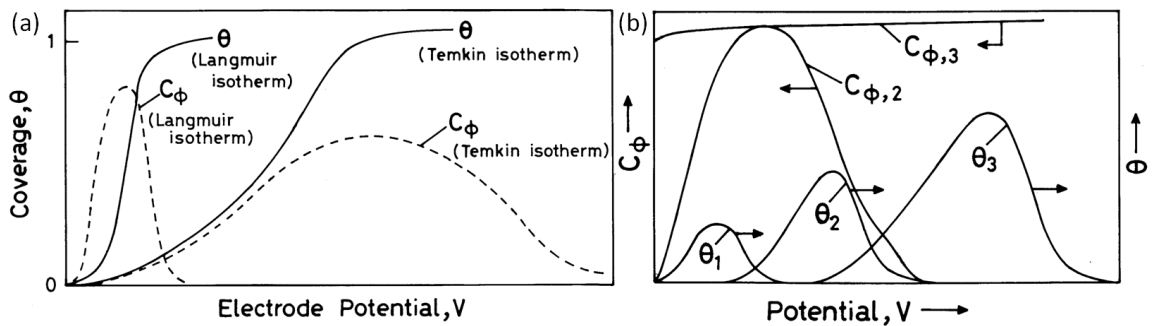


Figure 3.11. Variation of coverage (θ) and pseudocapacitance (C_{θ}) with electrode potential in accordance to Langmuir and Temkin isotherms (a). Variation of

pseudocapacitance and coverage with potential when more than one adsorbate is involved in the electrode reaction (b)[122].

Typical isotherms[122] are shown in Fig. 3.11 and are currently under investigation for developing more comprehensive models describing charge storage in pseudocapacitors. These isotherms once thoroughly studied and can be used to build a model for adsorption, intercalation processes and for the observed redox peaks observed on the cyclic voltammetry curves.

The peaks observed in pseudocapacitive were modeled with isotherms as shown in Fig. 3.11a. The peak positions depend on the potential (V) and the peak widths depend on adsorbate-adsorbate interactions. If there is no interaction between individual adsorbates, Langmuir isotherm is valid. Otherwise, if there is a repulsive interaction between adsorbates, the width of peak increases and pseudocapacitive behavior is available over a large potential-region. Moreover, the presence of multiple oxidation results in overlapped peaks leading more rectangular CV characteristic as observed in RuO_2 (Fig. 3.11b).

3.3.3 Understanding the Charge Storage Mechanisms

The abovementioned models were proposed for the ideal conditions and real systems are far from being ideal. In real systems, multiple mechanisms contribute to the charge storage. In order to differentiate which mechanism is responsible for the charge storage, various advanced experimental methods have been used up to now. The main focus on these advanced techniques is gathering data about the interface between the electrolyte and electrode surface. Knowing in-situ electrolyte organization in the pores and material morphology will enable to understand and model the charge storage more accurately.

The dynamics of the ions in the pores can be detected by sophisticated techniques including nuclear magnetic resonance[123] (NMR) spectroscopy, electrochemical quartz crystal microbalance[124], [125] (EQCM), small angle X-ray scattering[126] (SAXS), etc. Then the acquired experimental data coupled in conjunction with computer models and can be used to simulate the capacitive charge storage mechanism[127]. This approach enables one to model charge storage in porous carbons with a high degree of accuracy.

In pseudocapacitive materials, reversible surface redox reaction can be observed by probing the oxidation states of the transition metals. X-ray absorption near edge structure spectroscopy[53] (XANES) is a powerful technique to quantify the change in the oxidation states. This technique had been used to understand to explain the base of charge storage for the most investigated transition metal oxides (RuO_2 and MnO_2)[128], [129] and MXenes[130].

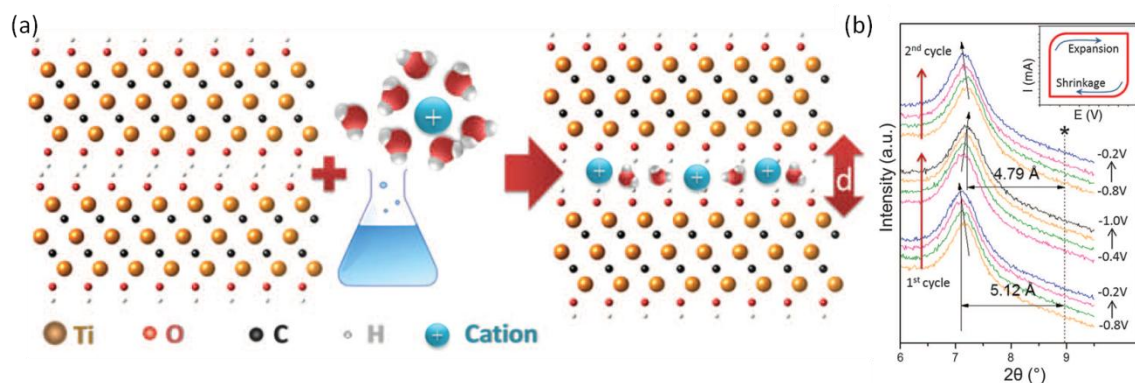


Figure 3.12. Schematic illustration of the intercalation of cations between $\text{Ti}_3\text{C}_2\text{T}_x$ layers. The interlayer spacing d increases after ion intercalation (a). Electrochemical in situ x-ray diffraction study of multilayer exfoliated $\text{Ti}_3\text{C}_2\text{T}_x$ in 1 M KOH solution (b) [8].

In layered materials such as MXene and birnessite type MnO_2 supercapacitors, the cation intercalation also contribute to the charge storage similar to the rechargeable batteries[8]. Cations easily diffuse into interlayer gaps (Van der Waals gaps) and intercalation process dominate over the charge storage. Charge storage is proportional to the degree of intercalation which can be monitored by a comparably less sophisticated but more precise technique, XRD[8]. The in-situ XRD analysis proves that the interlayer separation depends on the size of intercalant and degree of intercalation as shown in Fig 3.12.

The macroscopic effects of the charge storage have been detected by dilatometry which show that such ion insertion cause a reversible volume expansion or contraction depending on the applied potential[131]. This phenomenon had been observed for most of the electrochemically charged supercapacitor electrodes including porous carbons, electroactive polymers, and transition metal oxides.

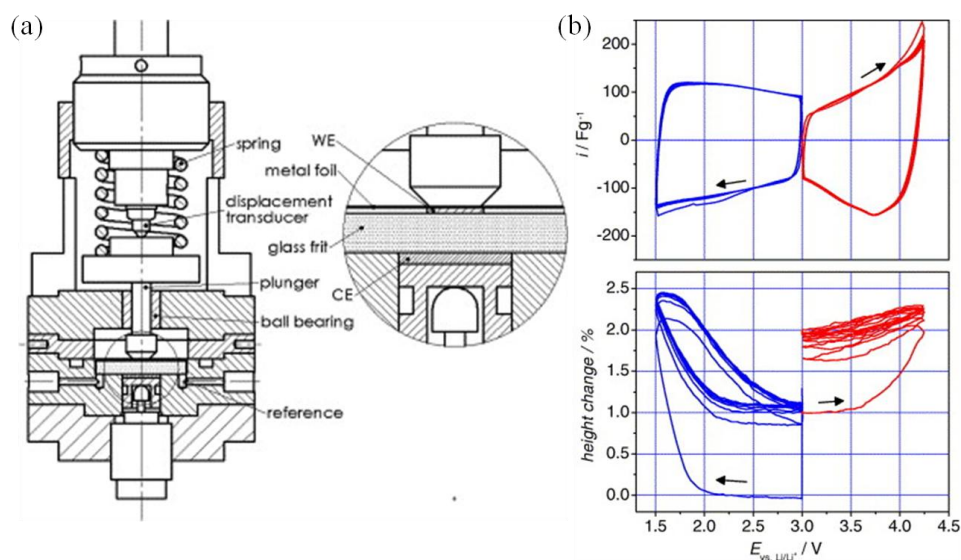


Figure 3.13. Typical cross-section of a dilatometer, working electrode is located on top of glass frit and any volume change is detected by displacement transducer (a). A CV

curve and corresponding volume change for porous carbon in organic electrolyte (b)[131].

Here is a typical example of in-situ electrochemical characterization technique showing how charge storage affects the volume of the electrode via ion insertion. For example, the thickness change probed via dilatometry technique as shown in Fig. 3.13. A supercapacitor device is placed in between one stationary and one moveable plate of the dilatometer, and then any expansion or compression is sensed with a displacement transducer. By using this setup, activated carbon was used as supercapacitor electrode with narrow pores (<1 nm) in an organic electrolyte[131]. The volume expansion was observed at the end of both anodic and cathodic sweep. The change in the volume shows a continuous insertion / de-insertion of ions expanding the porous carbon with a height change of 1.5%.

3.4 Chapter Summary

A summary of supercapacitor technologies have been introduced in this chapter. The main components of the energy storage devices including active electrodes, separators and electrolytes to fabricate state-of-the-art supercapacitor devices were summarized. This was followed by the electroanalytic techniques required to measure the electrochemical charge storage capacity in these systems. To address the reason why electrochemical supercapacitors exhibited such a high charge storage performance, charge storage models were discussed. In the end of the chapter, advanced analysis techniques were briefly discussed by which light is shed on to such high charge storage capacity in electrochemical supercapacitors.

Chapter 4 Electrochemical Actuators

Actuators directly convert energy into mechanical energy and produce either large displacement or large force. As such, they lend themselves to applications including micro/nano-electromechanical systems (MEMS/NEMS), biomedical devices, and robotic engineering[132]. In general, actuator materials respond to an external stimulus[133]–[136] (electric field, magnetic field, heat) by a reversible change in the mechanical property (shape, volume, and modulus) leading to an energy conversion to mechanical energy.

Ideally, designing a feasible actuator system in robotics require a material that can generate high mechanical force with large strain amplitudes, and exhibit high energy conversion efficiency as well as high cycle stability. Piezoelectric ceramics naturally such polymers exhibit high elastic modulus and generate high stress but produce low displacement, whereas electroactive polymers can induce high strains and displacement. However, exhibit low elastic modulus and generate low stress. Due to these limitations, the actual mechanical work done by these piezoelectric materials and electroactive polymers have remained low. In addition, piezoelectric systems require high potential gradient (10-100V/ μm) and electroactive polymers have long term stability issues making them impracticable for some applications[132].

Various types of actuator systems have been proposed with different energy conversion mechanism, the performances of which vary as shown in Table 1.

Table.1. Actuation performance of various materials [137]

Type (specific)	Maximum strain	Maximum pressure	Specific elastic energy density	Elastic energy density	Coupling efficiency k^2	Maximum efficiency	Specific density	Relative speed (full cycle)
	%	MPa	$\text{J} \cdot \text{g}^{-1}$	$\text{J} \cdot \text{cm}^{-3}$	%	%		
Dielectric elastomer (acrylic with prestrain)	380	7.2	3.4	3.4	85	60–80	1	Medium
Dielectric elastomer (silicone with prestrain)	63	3	0.75	0.75	63	90	1	Fast
Dielectric elastomer (silicone—nominal prestrain)	32	1.36	0.22	0.2	54	90	1	Fast
Electrostrictive polymer [P(VDF-TrFE)]	4.3	43	0.49	0.92	–	≈80 (est.)	1.8	Fast
Electrostatic devices (integrated force array)	50	0.03	0.0015	0.0025	50 (est.)	>90	1	Fast
Electromagnetic (voice coil)	50	0.1	0.003	0.025	–	>90	8	Fast
Piezoelectric ceramic (PZT)	0.2	110	0.013	0.1	52	>90	7.7	Fast
Piezoelectric single crystal (PZT-PT)	1.7	131	0.13	1	81	>90	7.7	Fast
Piezoelectric polymer (PVDF)	0.1	4.8	0.0013	0.0024	7	–	1.8	Fast
Shape memory alloy (TiNi)	>5	>200	>15	>100	5	<10	6.5	Slow
Shape memory polymer (polyurethane)	100	4	2	2	–	<10	1	Slow
Thermal (expansion—Al, $\Delta T = 500 \text{ K}$)	1	78	0.15	0.4	–	<10	2.7	Slow
Conducting polymer (PANi)	10	450	23	23	<1	<5 (est.)	≈1	Slow
Ionic gels (polyelectrolyte)	>40	0.3	0.06	0.06	–	30	≈1	Slow
Magnetostrictive (terfenol-D)	0.2	70	0.0027	0.025	–	60	9	Fast
Natural muscle (human skeletal)	>40	0.35	0.07	0.07	–	>35	1	Medium
Natural muscle (peaks in nature)	100	0.8	0.04	0.04	–	40	–	Slow–fast

Recent studies show that nanostructured electrochemical actuators can overcome aforementioned limitations associated with higher mechanical performance and lower operational potentials ($< 5\text{V}$) as an exemplified by nanoporous metals[138], [139] and carbon nanotubes[132]. Individual CNT fibers exhibit excellent mechanical and electronic properties, making them attractive candidate actuator material. However, the weak Van der Waals interaction between CNTs lowers the mechanical and electrical

performance of the CNT papers[132]. This is because the elastic modulus of the mechanically entangled CNTs (buckypaper) is three orders of magnitude lower than that of individual CNTs[132]. Attempts have been made to enhance the performance by wrapping DNA to CNT fibers, but their performance is still lower than individual CNTs[140]. Recently, graphene has shown similar actuation behavior. However, the restacking of graphene layers lowers the accessible surface area, which is further decreased the charge storage and deteriorated actuation behavior[141]–[143].

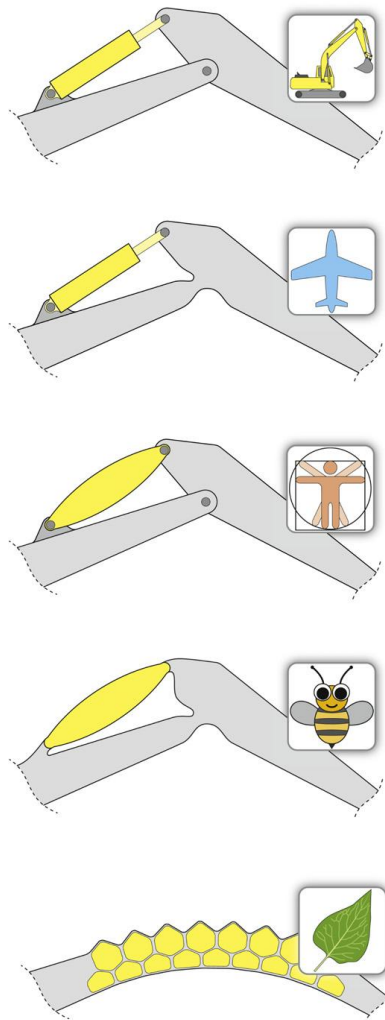


Figure 4.1. Design principles for actuator systems with single rotational degree of freedom. A rigid body actuator (a)[144]. A rigid body actuator with compliant structure

(b). Compliant actuator with rigid body structure (c). A compliant body and actuator[145]
 (d). A hybrid compliant actuator and body (e)[146].

To utilize the actuation in robotics, different design principles were illustrated in Fig. 4.1 such as rigid body actuators and compliant actuators. Compliant actuators have single a rotational degree of freedom without any rigid structure and hinges. Lack of rigid body and hinges reduces the number of parts, backlash, friction and wear which makes the mechanical systems clumsy[146]. Such advances in actuator materials will enable to develop compact, lightweight and efficient tools for robotics, biomedical devices and MEMS systems. As illustrated for single rotational degree of freedom for hydraulic systems, muscles and nastic plants in Fig. 4.1, the electroactive actuators with bending beam configuration may be categorized as electrochemical compliant actuators[146].

4.1 Electrochemical Actuator Device Configuration and Electrode Materials

Ideally, any electrochemically active material used in a supercapacitor can potentially function as an electrochemical actuator material. For instance, porous carbons[132], [142], [143] (CNTs, graphene, activated carbon), electroactive polymers[147], [148] (PPy, PANy), transition metal oxides[149, p. 5] (V_2O_5) and nanoporous metals[138], [139] (nanoporous gold, nickel) have been used as electrochemical actuator. Here, the actuator device configuration is similar to supercapacitors devices as shown in Fig. 4.2.[143]. In such devices, the main criterion is that all of the required components be flexible to carry out the mechanical deformation.

An actuator device and its actuation mechanism is depicted in Fig.4.2. In this configuration, two carbon-based electrodes are separated with a gel electrolyte. Here, the gel electrolyte is comprised of a polymer such as polyvinylidenefluoride-co-hexafluoropropylene (PVDF-HFP)[150] or polyvinylalcohol[151] (PVA) that is mixed with ionic liquid or aqueous electrolytes. Under electrical stimulus, the ion migration expands or contracts the active electrodes causing a bending displacement. Depending on the choice of electrolyte and electroactive material, the mechanism of actuation varies. More detailed information will be given in the next sections (4.4).

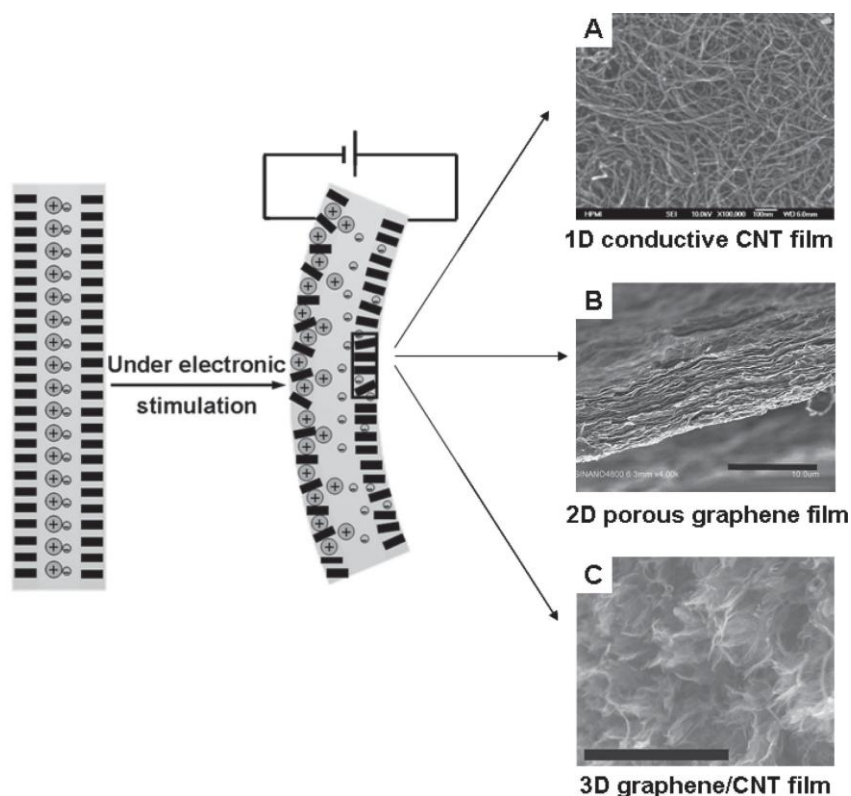


Figure 4. 2. Schematic of electrochemical actuator device illustrated in steady state and stimulated state. (a-c) Different carbon-based electrode materials for actuators. Scale bar: 500 nm[143].

The performance of the actuator depends strongly on the crystal structure of [132], [149] and pore distribution[139] in the material. If the material has isotropic

properties, the expected volume change is isotropic. However, anisotropic materials such as layered materials or nonuniform pore distribution are expected to cause anisotropic actuation [139]. The abovementioned materials generally have anisotropic crystal structures [132], [149, p. 5], pore distribution[139] or anisotropic grain orientation[152]. For instance, electrodeposition or stretching the electroactive polymers results anisotropic backbone orientation and the actuation performance strongly depends on the orientation [152].

4.2 Electrochemical Actuation Measurement Techniques

A typical volumetric electrode deformation due to charge storage can be monitored by measuring either the thickness change (out-of-plane strain) or length change (in-plane strain) on the electrode. The thickness change can be tracked via special techniques such as displacement transducer (dilatometer)[131], fiber optic displacement sensor (25nm)[153] or atomic force microscopy (<1nm)[154] with high precision. On the other hand, regarding the length is much longer than the thickness; the elongation rate for the length is much higher the thickness change for the same strain. Therefore less precise systems would be enough to measure the elongation such as the laser displacement test[142]. Another approach to quantify the actuation is amplifying the displacement via bimorph actuator configuration which can be monitored with a CCD camera[147]. Depending on the magnitude of the deformation, one of the above mentioned sensing systems can be selected.

For example, Gaffari et. al.[153] prepared highly oriented graphene and measured the thickness change during charge storage via fiber optic displacement sensor as shown

in Fig. 4.3. They obtained varying expansion rates up to 50% depending on the potential range and selected ionic liquid (Fig 4.3c). Gaffari et.al proposed that the huge strain is because of the ingress and/or depletion of mobile ions in the nano-pores in order to compensate the charges on MEGO electrode (Fig 4.3b). Such high magnitude of expansion is exciting, but the frequency response is very low as shown in the elapsed time for the reported performance in Fig 4.3c. Furthermore, the mechanical strength of graphene in the actuation direction is very low (9-67 MPa)[153].

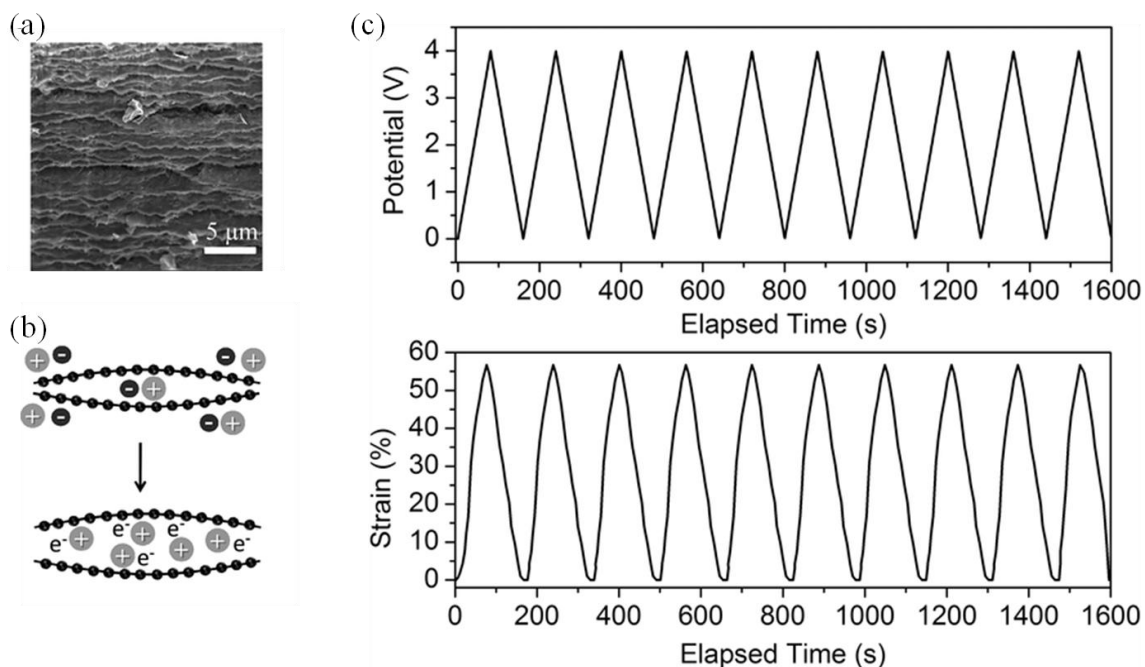


Figure 4.3. SEM image of highly oriented MEGO sheets [153](a). Illustration of ion ingress into narrow MEGO pores leading the ionic electroactuation (b). Applied voltage vs electroactuation strain in BMIM BF₄ electrolyte (c).

Xie et al[155] fabricated graphene strips and analyzed the length change under electrochemical induction in aqueous electrolyte. They used an apparatus to sense the

strain by reflected laser and displacement sensor shown in Fig. 4.4. Up to 0.85 % strain along the graphene strip has been observed.

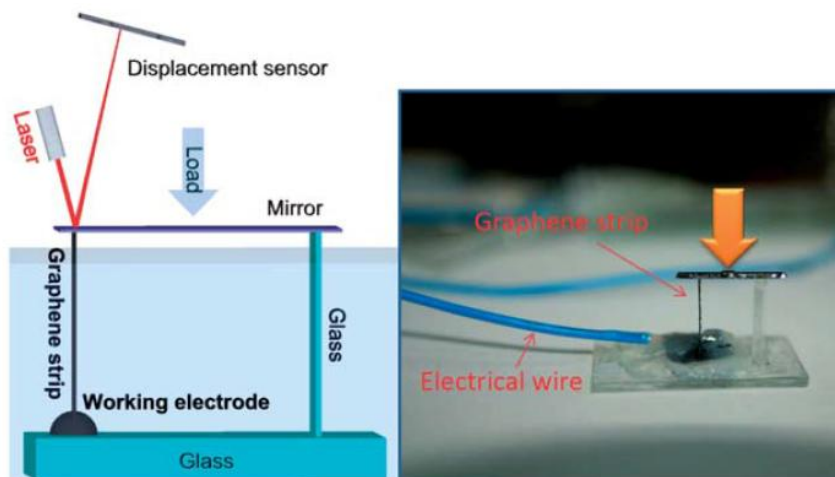


Figure 4.4 Graphene actuators[155]. The apparatus used for characterizing the length change along graphene film under load (a), the image of a final fabricated device (b).

Xie et al.[142] also modified two opposite surface of graphene with oxygen and hexane plasma (Fig. 4.5b) to obtain one side of the graphene strip electrochemically active while keeping the other side inactive. Such modification induces uneven actuation through asymmetric charging/discharging along the two opposite sides of monolithic graphene film. Under an applied potential, the active side stores charge and expands, while the other side stay passive. Therefore, the asymmetrically modified graphene film bends in the same way as that a bimetallic strip. Small lateral (in-plane) expansion or contraction results in large displacement by bending of the film. The authors propose that the strain is based on the change of the C-C bond length due to charge injection instead of intercalation. They found that the interlayer separation did not change during electrochemical induction according to their XRD study. Therefore, the intercalation

mechanism was ruled out. A detailed elaboration of electrochemical actuation mechanisms and the mechanics of bimorph actuators is provided in what follows.

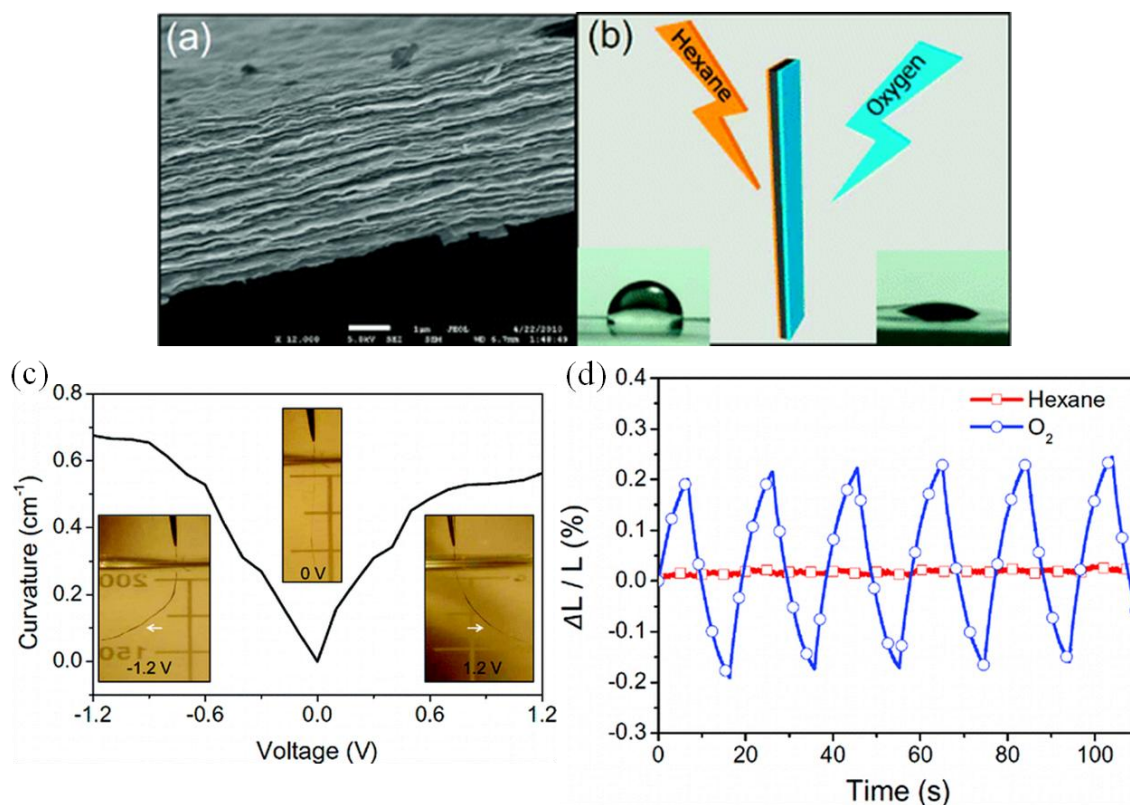


Figure 4.5. Graphene based bilayer actuator. Crosssection of SEM image of graphene (a). Illustration of asymmetric surface modification of graphene (b). Curvature change of modified graphene (c) and corresponding strain values under applied potential.[142]

4.3 Bimorph Actuators

Bilayer actuators consist of at least one active layer and one passive layer as shown in Fig. 4.6. In this configuration, a slight difference along the lateral dimensions bends the bilayer film, causing large flexural displacement. By using this approach, the electrochemical stimulus is directly transformed to mechanical response in the form of a

large displacement, which can be used in robotics, optical fiber switches and microscopic pumps in principle [132].

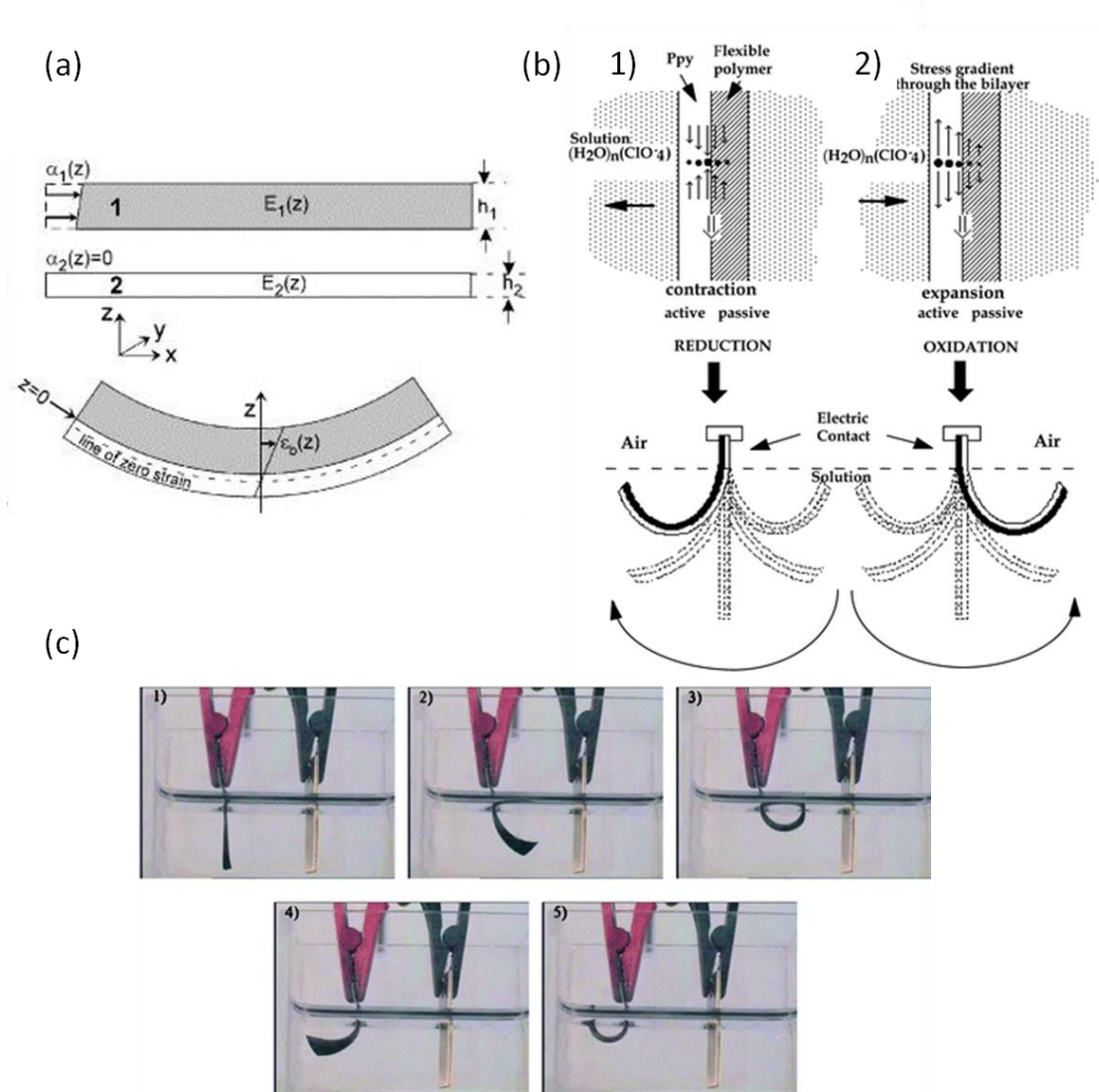


Figure 4.6. Schematics of displacement measurements of actuator[156].

On a single strip actuator material, the volume change elongates the strip which can be easily quantified by dividing the elongation by the length of the strip[132]. On the other hand, the strain calculation is more complicated for the bilayer systems, because the strain distribution in bending beam is not homogenous due to the passive layer which

constrains the elongation of the active layer. A typical strained and bent bilayer system is illustrated with stress gradient along its cross section in Fig. 4.6b.

The actual strain on the active electrode is not equal to the induced actuation strain due to the presence passive layer. Because of this reason, the degree of bending were used to compare the actuation performance in some studies[142]. The degree of bending is quantitative measure of the curvature induced in the beam which is representative of deformation. In light of recent mechanical models[157], the actual deformation (represented as a strain) is calculated by taking into account the effect of the passive layers.

First attempts to model the mechanics of bilayer systems has been developed by Timoshenko[158] for bi-metal thermostats where differential thermal expansion of the two metals induce bending displacement. These models were modified and used for electrochemical actuators in which only one layer contributes to the actuation[147], [148]. In these models, the small angle approximation is used to extract the curvatures from small displacements which are comparably lower than actuator length. For large deformations, this approximation is not valid and further modifications were developed for bilayer[139], [159] and multilayer actuators[157], [160]. It has been shown that there is a linear relation between the bending curvature of the beam and the induced strain on the active electrode as a function of thickness and elastic modulus of each layer[157]. Since, the degree of bending is proportional to the strain; a coefficient was derived for multilayer actuator systems[157]. Then the curvature (κ) is

$$\kappa = c_k \alpha_3 , \quad (31)$$

where c_k is the strain coefficient and α_3 is the actuation strain. The computational approach to derive the bending mechanics of bimorph actuators are discussed in the following section.

4.3.1 Mechanical Calculations

Typical bending motion of a multilayer beam due to active layer expansion/contraction is shown in Fig. 4.6(a,b). The lateral expansion or contraction of the active layer creates a surface stress at the interface leading a bending deformation on the beam. Corresponding strain distributions along the bent beam cross section varies with tensile strains at the convex surface, and compressive strain at the concave surface and zero strain at the neutral plane. The bending strain can be calculated from the normalized difference in the circumferences at a distance from the neutral plane according to [157]

$$\varepsilon_0(z) = \varepsilon_0 + \frac{c_z - c_0}{c_0} = \varepsilon_0 + \frac{2\pi(R + z) - 2\pi R}{2\pi R} \quad (32)$$

and

$$\varepsilon_0(z) = \varepsilon_0 + \frac{z}{R} = \varepsilon_0 + \kappa z \quad (33)$$

where ε_0 is the initial strain at $z=0$, R is the radius of the bent film, c is the corresponding circumference for the radius, κ is the bending curvature and z is the distance from the neutral plane. The corresponding stress is given by

$$\sigma = E\varepsilon = E(\varepsilon_0 - Z\kappa - \alpha) \quad (34)$$

The bending force and moment is calculated by integrating the stress along the cross section. By using

$$F = \int_0^h \sigma dz = \int_0^h E (\varepsilon_0 - Z\kappa - \alpha) dz \quad (35)$$

and

$$M = \int_0^h \sigma z dz = \int_0^h E (\varepsilon_0 - Z\kappa - \alpha) z dz \quad (36)$$

However, it is difficult to define the neutral plane for multilayers, since the mechanical and geometric properties of each layer need to be taken into account. Hence, further derivation is required to find the relation between curvature and induced strain.

At the equilibrium in a bent beam, the total force and moment are zero. Considering $\int E dz = A$, $\int E z dz = B$, $\int E z^2 dz = D$, the force and moment can be written as,

$$A\varepsilon_0 - B\kappa = F\alpha \quad (37)$$

and

$$B\varepsilon_0 - D\kappa = M\alpha \quad (38)$$

where A is the extensional stiffness, B is bending-extension coupling stiffness and D is bending stiffness. The relation between curvature and induced strain for multilayer beam can be obtained by integrating the force and moment equations as a function of the thickness and Young's modulus. For bilayer beam, the equation for curvature is;

$$\kappa = \frac{6m_2n_2(1+m_2)(\alpha_1-\alpha_2)}{h_1(1+4m_2n_2+6m_2^2n_2+4m_2^3n_2+m_2^4n_2^2)} \quad (39)$$

with $m_i = h_i/h_1$, $n_i = E_i/E_1$, h is the layer thickness and E is the elastic modulus.

Similarly, for trilayer beam, the curvature is

$$\kappa = \frac{6(X_{12}+X_{13}+X_{23})}{h_1(1+Y_2+Y_3+Y_{23})} \quad (40)$$

where

$$X_{12} = m_2 n_2 (1 + m_2) (\alpha_1 - \alpha_2) \quad (41)$$

$$X_{13} = m_3 n_3 (1 + 2m_2 + m_3) (\alpha_1 - \alpha_3) \quad (41)$$

$$X_{23} = m_2 n_2 m_3 n_3 (m_2 + m_3) (\alpha_2 - \alpha_3) \quad (42)$$

$$Y_2 = 4m_2 n_2 + 6m_2^2 n_2 + 4m_2^3 n_2 + m_2^4 n_2^2 \quad (43)$$

$$Y_3 = 4m_3 n_3 + 6m_3^2 n_3 + 4m_3^3 n_3 + m_3^4 n_3^2 \quad (44)$$

$$Y_{23} = m_2 m_3 n_3 [(4m_2^2 + 6m_2 m_3 + 4m_3^2) n_2 + 12(1 + m_2 + m_3)] \quad (45)$$

Since only one active layer contribute to the actuation, the curvature for three layer electrochemical actuator can be approximated as,

$$\kappa = \frac{-6m_3 n_3 [1+2m_2+m_3+m_2 n_2 (m_2+m_3)]}{h_1 (1+Y_2+Y_3+Y_{23})} \alpha_3 \quad (46)$$

4.2.2 Work Density Calculations

The volumetric (W_v) and gravimetric (W_g) work densities of single layer and free restacked 1T phase MoS₂ film are typically calculated with[132];

$$W_v = \frac{E \varepsilon^2}{2} \quad (48)$$

$$W_g = \frac{E \varepsilon^2}{2\rho} \quad (49)$$

In constrained systems such as bending beam, the active material is not free to move under the strained state, the residual force causes the beam deflect. Then the work (W) in bending the beam is determined by the product of the bending moment M and the

bending angle θ which can be obtained by bending curvature and actuator length[157].

The curvature can be represented by the ratio of bending moment (M) to the bending stiffness (EI) according to Euler beam theory [157]. Then the work is

$$W = \frac{M\theta}{2} = \frac{M\kappa L}{2} \quad (50)$$

and

$$\kappa = \frac{M}{EI} \quad (51)$$

then,

$$W = \frac{M^2 L}{2EI} \quad (52)$$

Integrating previously constructed moment equations for multilayer actuator, the moment is obtained as

$$M = \frac{E_1 b h_1^3 (1+Y_2+Y_3+Y_{23})}{2} (\alpha_1 + (m_2^2 + 2m_2)n_2\alpha_2 + (m_2^2 + 2m_3(1+m_2))n_3\alpha_3) \quad (53)$$

and the bending stiffness is

$$EI = \frac{E_1 b h_1^3 (1+Y_2+Y_3+Y_{23})}{12(1+m_2n_2+m_3n_3)}. \quad (54)$$

4.4 Electrochemical Expansion Mechanisms

Nanoporous materials have extremely high surface to volume ratios enabling large amount of charges to be stored on the surface electrochemically. This mechanism is the basis of electrochemical supercapacitors. Moreover, the electrochemical charge storage reconstructs the space-charge region at the electrode/electrolyte interface. Such charge redistribution on the surface affects the interatomic bonds and the distance between atoms via double layer formation[132], [161], ion intercalation[149], [153] or Faradaic reaction[139], [149]. If these charge storage mechanisms render a macroscopic

change on the electrode dimensions, these materials can be used as electrochemical actuators. There are some electrochemical actuation mechanisms were proposed to explain the relation between charge storage and actuation.

4.4.1 Ion Intercalation/de-intercalation

If pore size is comparable or smaller than the ion size, ions intercalate through the narrow pores during the charge storage, and then the ion intercalation causes an expansion in the electrode [153]. This mechanism provides large expansion values (up to 60%). However, this mechanism is active only at low frequencies which is not desired in the actuator systems.

4.4.2 Faradaic Redox Reaction

Faradaic redox reaction were proposed as possible actuation mechanism for pseudocapacitive materials such as V_2O_5 [149], NiO[139] and PPy[157]. In these systems, the actuation was attributed to the dimensional changes related to redox reaction. Such redox reactions lead a change on the oxidation state and the bond length of the electrochemically active materials.

4.4.3 Quantum Mechanical and Electrostatic Effect

An applied voltage injects electronic charge to the electrode which is compensated by ions at the interface of the electrode/electrolyte (double layer)[132], [135]. For low charge densities, injected electrons expand C-C bonds and injecting holes contracts C-C bonds on the carbon surface (CNTs, graphene). The typical calculated strain value for quantum chemical based strain is 0.2%. For high-density charge injection,

the double layer enhances the strain to 1% according to theoretical[135] and experimental[132] studies as illustrated in Fig. 4.7.

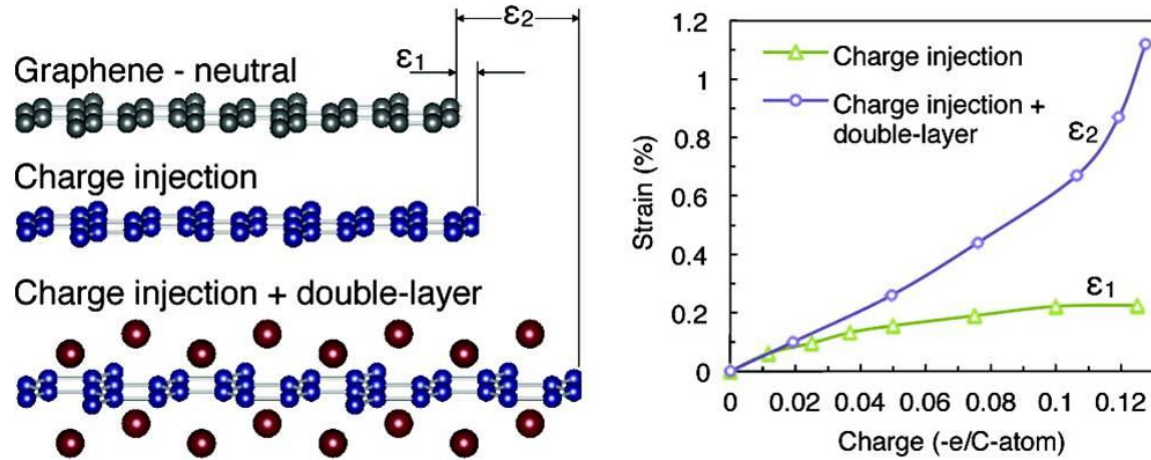


Figure 4.7. Illustration of strain with charge injection and DL assisted strain (a).

The strain comparison between charge injected and double layer assisted charge injection mechanisms (b)[135].

4.5 Chapter Summary

A brief summary of the actuator technologies was presented in this chapter. The focus was on the electrochemical actuators and a brief summary was provided regarding their structure. The effect of anisotropy on the electrode expansion and actuation behavior was highlighted. To quantify the actuation performance, different types of actuation behaviors and their electromechanical analysis were described, including bending beam actuators. To evaluate the results, the bending mechanics and models were derived. Finally, different actuation mechanisms were briefly discussed to shed light on the relation between actuation and charge storage. The statement of the problem and method of attack will be discussed in the next section.

Problem Statement and Solution Strategy

MoS₂ has a 2H phase crystal structure that exhibits semi-insulating electronic behavior[39], and therefore may not immediately appear attractive as an electrode material for energy storage. Indeed, only a few studies have described the electrochemical charge storage properties of MoS₂ electrodes [18]–[22]. To enhance the electrical conductivity, hybrid electrodes composed of graphene/MoS₂ (ref. [21]) and polyaniline/MoS₂ (ref. [22]) have been investigated. To date, however, the electrochemical storage performances obtained with either pure or hybrid 2H phase MoS₂ electrodes have been relatively modest compared with those of graphene[15], [16].

Recent prior work demonstrated that it is possible to convert semiconducting 2H phase of MoS₂ to the metallic 1T phase by chemical exfoliation of bulk MoS₂ using organolithium chemistry [50]. This metallic phase has 10⁷ times higher conductivity than the semiconducting phase [24]. In terms of layered structure and high conductivity, electrochemically, 1T MoS₂ might behave like EDLC type materials. Besides, molybdenum is a transition metal and 1T MoS₂ might behave as a pseudocapacitive materials. To date, there is no report on the electrochemical charge storage behavior of 1T MoS₂.

The aim of this work is to evaluate the 1T phase MoS₂ as supercapacitor electrode. To succeed this goal,

1. A suitable procedure to fabricate the 1T phase of MoS₂ as a supercapacitor electrode will be developed.

2. The electrochemical performance of 1T MoS₂ in various electrolytes will be investigated and compared our findings with other materials.
3. Ex-situ XRD and in-situ Raman analyses will be performed in order to comprehend the storage mechanisms by characterizing the structural changes associated with charge storage.
4. The electrochemomechanical behaviour of 1T MoS₂ using bimorph electrode configuration in different electrolytes will be analyzed and compared to our findings with other electrochemical actuator materials.

Chapter 5. Experimental Results

5. Material Synthesis, Electrode Fabrication and Material Analysis

This chapter describes the procedures of the material synthesis, electrode fabrication and material characterization in detail. Material synthesis included organolithium chemistry to lithiate and exfoliate bulk MoS₂ powder to a monolayer mostly 1T phase MoS₂.

5.1 Lithiation and Chemical Exfoliation of MoS₂

Chemically exfoliated MoS₂ was synthesized by lithium intercalation into bulk MoS₂ powder as reported previously [162]. Specifically, 3 mL butyl-Lithium (Sigma Aldrich) were added to 0.3 g bulk MoS₂ powder under argon and heated up and refluxed under argon for 48 h. The mixture was then filtered and washed with hexane (5 x 25 mL) to remove excess butyllithium (Fig. 5.1). The intercalated powder was then exfoliated in water at 1.5 mg/mL sonicated for 1 h and centrifuged to remove lithium cations as well as the non-exfoliated materials.

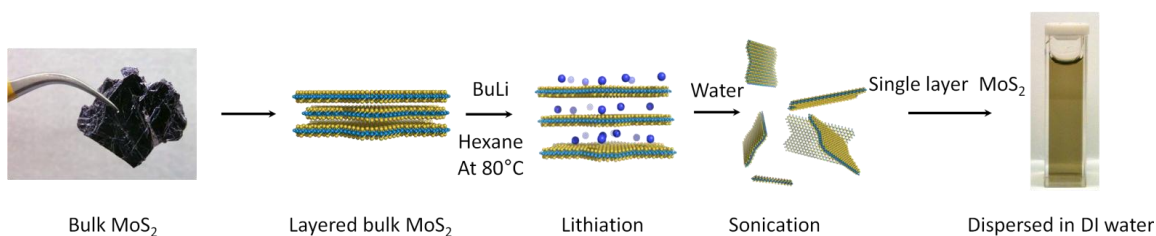


Figure 5.1. Schematics of chemical exfoliation of MoS₂.

5.2 Restacking of Exfoliated MoS₂ for Electrode Fabrication

The suspended chemically exfoliated single layer MoS₂ nanosheets were filtered over nitrocellulose membranes (25 nm diameter pore size) and then transferred on 100 nm gold coated quartz or 125 μ m polyimide substrate (see Fig. 5.2). The membrane was finally dissolved by using acetone. The thickness of the restacked 1T MoS₂ film was varied from 1 μ m to 5 μ m depending on the volume of the MoS₂ solution filtered. Restacked samples were stored under vacuum.

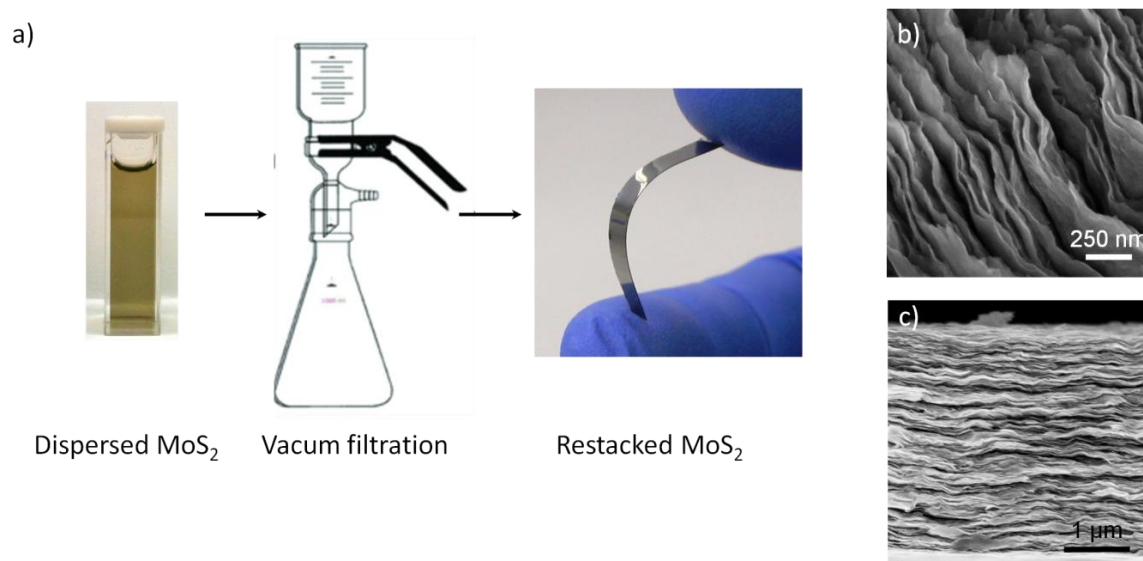


Figure 5.2. Schematics of restacking process of MoS₂ by vacuum filtration (a). SEM images of restacked MoS₂ (b, c).

5.3 Fabrication of Chemically Exfoliated 2H Phase MoS₂ Electrodes

The 2H phase of MoS₂ can be restored by annealing the as-exfoliated 1T MoS₂ electrode at 300° C under inert argon atmosphere. The 1T MoS₂ electrodes were placed in a quartz tube and the atmosphere was evacuated for 15 min. The electrodes were then annealed at 100° C, 150° C, 200° C, 250° C and 300 °C for 15 min under Argon with 80 sccm flow rate.

5.4 Physical Characterizations

In order to ascertain that each chemical exfoliation, restacking, and phase transformation processes were successfully completed, various characterization techniques were brought to bear. Firstly, single layer MoS₂ flakes were analyzed with scanning electron microscopy (SEM). Secondly, X-ray photoelectron spectroscopy (XPS) and Raman spectroscopy were used to analyze the phase transformation. Thirdly, the crystal structure and morphology of restacked MoS₂ were characterized with X-ray diffractometer (XRD) in conjunction with SEM in order to determine the orientation of flakes, and restacking order.

5.4.1 Characterizing Chemically Exfoliated Single Layer MoS₂

SEM imaging was performed using a Zeiss Sigma Field Emission SEM with Oxford INCA PentaFETx3 EDS system (Model 8100). Chemically exfoliated single layers of MoS₂ were transferred on silicon substrate. As shown in Fig.5.3, SEM image, MoS₂ layers were efficiently exfoliated toward single layer MoS₂ with large flake size distribution.

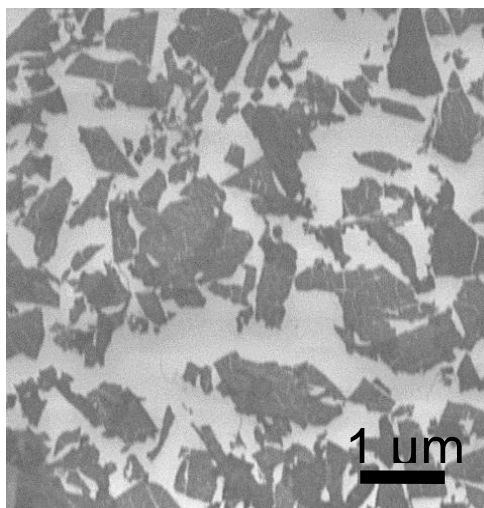


Figure 5.3. SEM images of as-exfoliated single layer 1T phase MoS₂ nanosheets.

5.4.2 Characterizing Phase Transformation from 2H to 1T MoS₂

5.4.2.1 Raman Spectroscopy

The Raman spectra were obtained using a Renishaw inVia system operating at 514 nm (2.41 eV). The presence of 1T phase of MoS₂ was identified from the presence of E_g¹, J₁, J₂ and J₃ peaks.

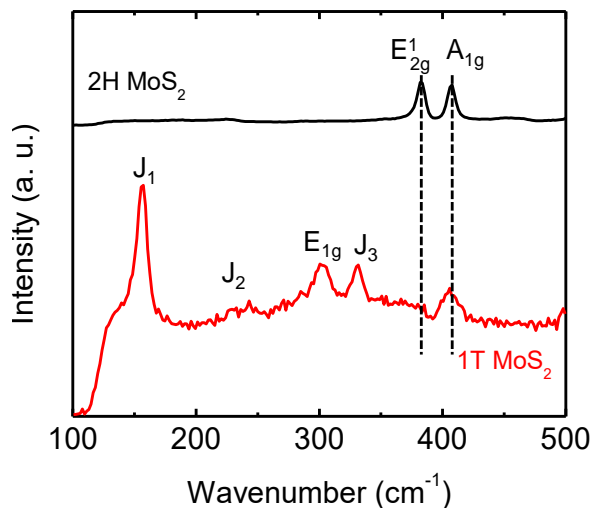


Figure 5.4. Raman spectra of chemically exfoliated 1T MoS₂ compared to 2H MoS₂.

5.4.2.2 X-ray Photoelectron Spectroscopy (XPS)

XPS analysis of chemically exfoliated and restacked MoS₂ is shown in Fig. 5.5. By deconvoluting the doublet peak in Fig. 5.5a, the phase content of MoS₂ was found as 70% 1T phase and 30% 2H phase of MoS₂. In addition to the 1T content, XPS also confirmed the absence of oxidized molybdenum or sulfur as can be seen in Fig. 5.5.

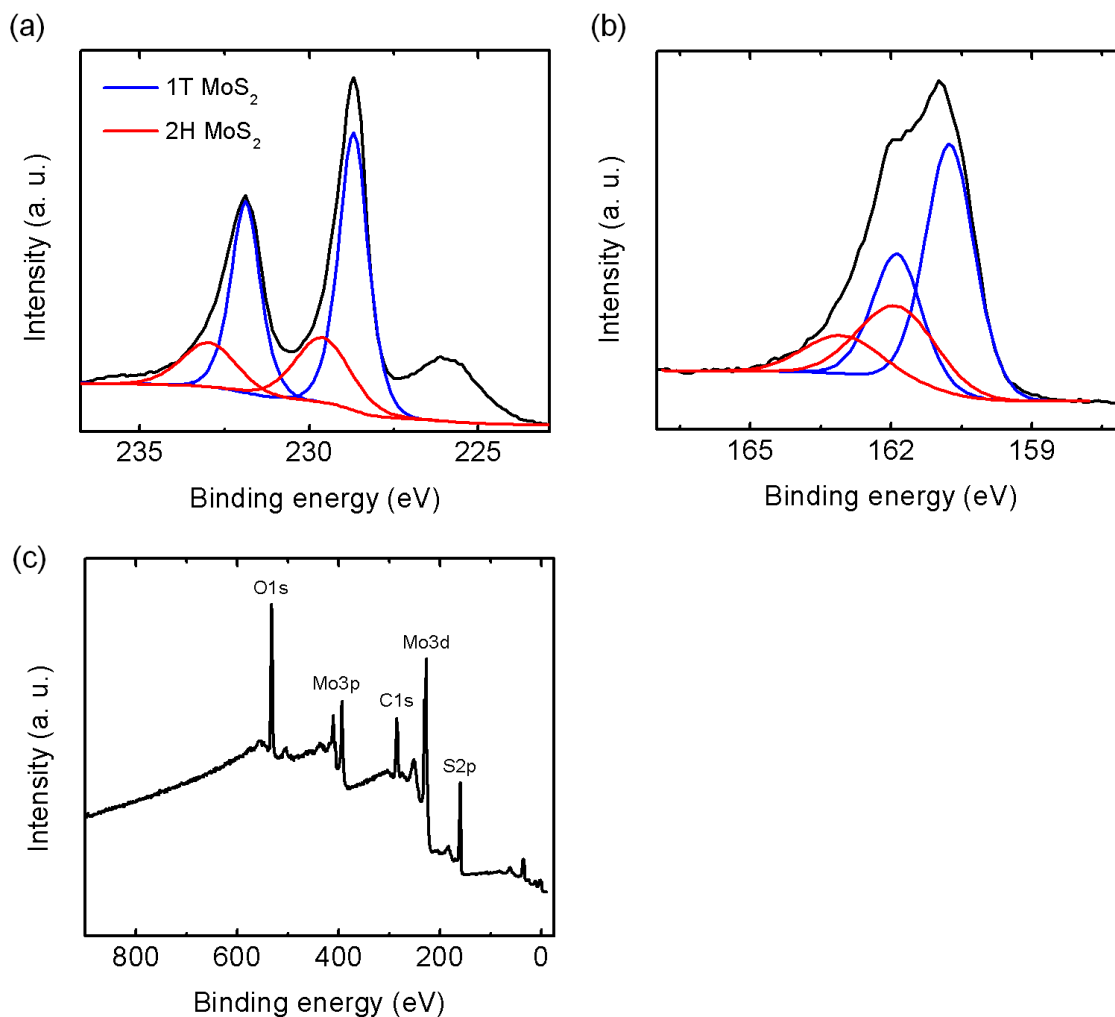


Figure 5.5. High-resolution x-ray photoelectron spectrum from the Mo 3*d* region of as-exfoliated 1T MoS₂ (a). and from the S2*p* region (b). XPS survey spectrum for as-exfoliated 1T MoS₂ (c).

5.4.3 Characterizing Restacked MoS₂

5.4.3.1 X-Ray Diffraction (XRD)

X-ray diffraction (XRD) experiments were carried out using a X-ray diffractometer from PANAnalytical (model PW3040/60) using a Cu K α radiation source ($\lambda = 1.5418\text{\AA}$). As shown in Fig. 5.6., the x-ray diffraction patterns of bulk powder and restacked films

of nanosheets reveal a broad (002) peak for restacked MoS_2 . The (002) peak, which is attributed to the interplanar spacing between the nanosheets (6.15 \AA), is the most intense peak but the presence of a new (001) peak at $2\theta \sim 7.3^\circ$ indicates an additional mean separation of $\sim 6 \text{ \AA}$ between the layers during restacking. The broadness of the (002) peak and the presence of the (001) peak indicate that the nanosheets are randomly arranged during restacking with large spacings between the layers.

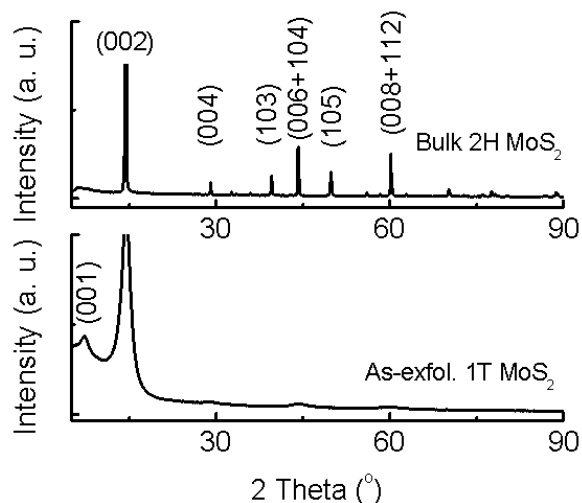


Figure 5.6. X-ray diffraction of bulk MoS_2 compared to as-exfoliated restacked MoS_2 .

5.4.3.2 Scanning Electron Microscopy (SEM) for Restacked MoS_2

The cross section of SEM images of restacked MoS_2 reveals that the layers were well oriented on the substrate horizontally. The thickness of each restacked film was measured from cross sectional SEM images as well (see Fig. 5.7).

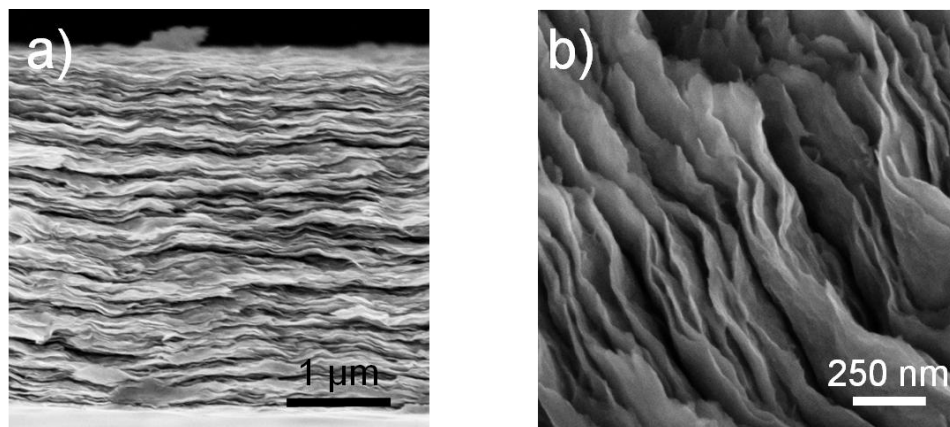


Figure 5.7. Side-view of the electrode observed by scanning electron microscope (SEM) showing the layered nature of the film made by restacking exfoliated MoS₂ nanosheets (a). High magnification image of restacked MoS₂ nanosheets (b).

5.4.3.3 Measurements Contact Angle

We measured the contact (wetting) angle by the sessile drop technique using a droplet of water of 5 μ L volume on the 1T MoS₂ film and measured the angle formed by the liquid and solid phases. The contact angle was found 28°, which is much lower than the wetting angle on quartz (79°), indicating the high hydrophilic nature of the 1T phase MoS₂.

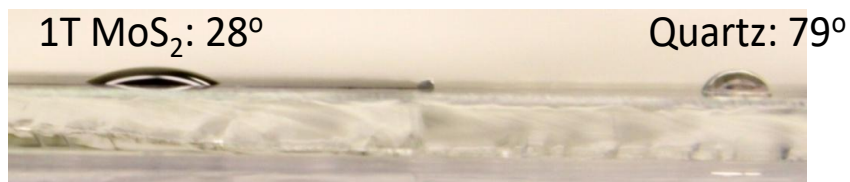


Figure 5.8. Static contact angle images of 1T MoS₂ film compare to quartz.

5.5 Chapter Summary

Organolithium chemistry was used to exfoliate bulk MoS_2 powders into single layered nanosheets [44], [50]. The flowchart of the synthesis method used is depicted in Fig. 5.1. [50]. This method yields 100% monolayered MoS_2 nanosheets that are suspended in water. Thick films or “paper” of 1T MoS_2 were obtained by filtration technique which enables one to restack the suspended nanosheets (see Fig. 5.2.). After exfoliation, the nanosheets are rigorously cleaned with hexane and de-ionized water to completely remove the residual organolithium contamination. The structure and phases of exfoliated nanosheets were assessed by Raman spectroscopy as shown in Fig. 5.4, and by x-ray photoelectron spectroscopy as depicted in Fig. 5.5. The two polymorphs of single-layer MoS_2 were identified from the $\text{Mo}3d$ and $\text{S}2p$ peaks in XPS. It was reported that the components of the 1T phase appear at a lower binding energy (~ 0.9 eV) compared to their 2H phase [50], [163]. Upon deconvoluting the $\text{Mo}3d$ and $\text{S}2p$ peaks of chemically exfoliated MoS_2 , the 1T phase content of the nanosheets was found ~ 70 %.

Chapter 6.

6. Electrochemical Characterizations

MoS₂ electrodes were prepared on gold current collector for electrochemical analysis as discussed at previous chapter. These analyses were performed in aqueous and organic electrolytes.

6.1 Electrochemical Measurements in Aqueous Electrolytes

Electrochemical analyses were performed with three-electrode cell configuration in 0.5 M H₂SO₄, Li₂SO₄, Na₂SO₄, K₂SO₄, KCl or KBr electrolyte solutions. Restacked MoS₂ films on gold contact were used as the working electrode. Saturated calomel electrode (Hg/HgCl) and platinum electrode were used as reference and counter electrode, respectively. Alternatively, a graphite rod was used as counter electrode in H₂SO₄. Electrochemical measurements were conducted using a Solartron Multistat 1480 in conjunction with Solartron 1260 Frequency Response Analyzer. For a fair comparison of their electrochemical behavior, working in different electrolytes, electrodes were prepared with the same thickness of MoS₂ and their masses were normalized with the electrode surface.

6.1.1 Cyclic Voltammetry

Cyclic voltammetry data were collected between -0.15 V and 0.85 V as a function of normalized hydrogen evolution (NHE) for neutral electrolytes; and between -0.15 V and 0.45 V vs NHE for acidic electrolytes. The operational potential ranges were chosen such that hydrogen evolution (HER) at low potentials and the oxidation of MoS₂ at high potentials were avoided.

6.1.1.1 In Neutral Electrolytes

Fig. 6.1(a,b) shows typical CV curves that were obtained scan rates ranging from 5 mV/s to 1000 mV/s for 0.5M Na₂SO₄. Rectangular shape CV characteristics were observed even at very high scan rates which indicate that 1T MoS₂ exhibits capacitive behavior.

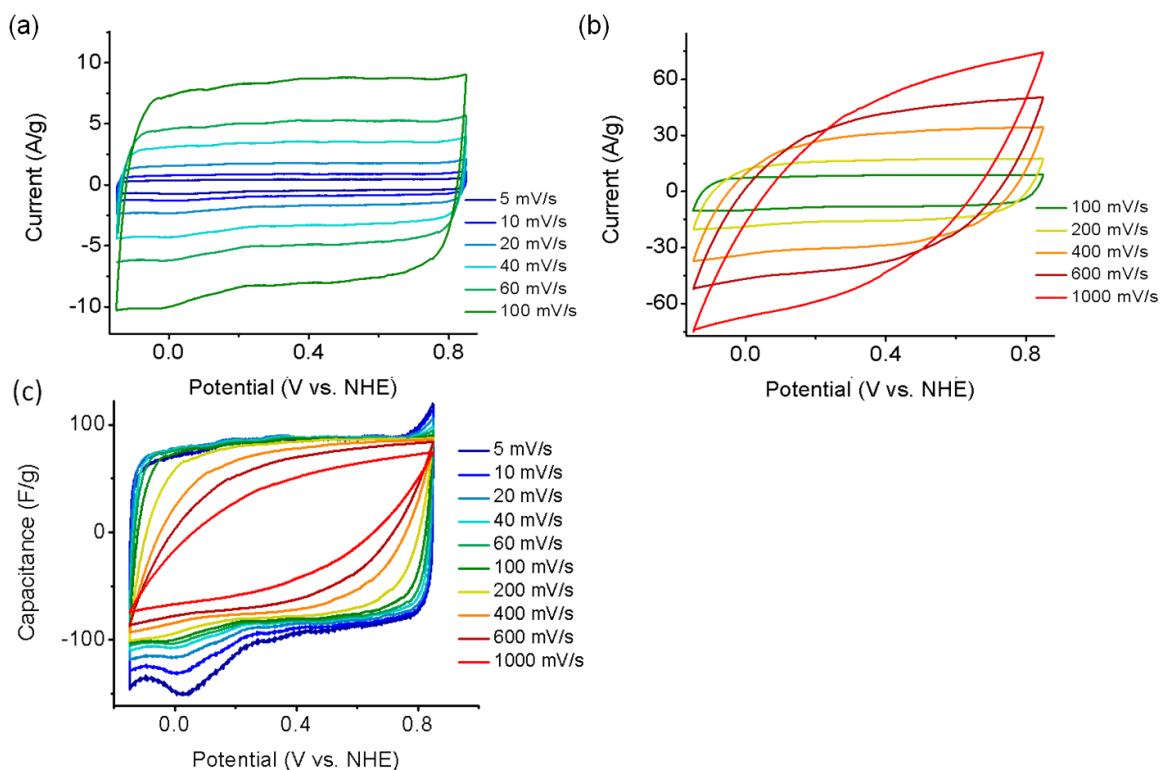


Figure 6.1. CVs of 1T phase MoS₂ electrodes in 0.5 M Na₂SO₄ from 5mV/s to 1000 mV/s (a,b). Capacitance remains virtually constant up to scan rate of 100 mV/s. (c)

For better comparison, standard cyclic voltammograms were recorded at different scan rates and transformed to the capacitance vs potential plots (Fig. 6.1c) by using Eqn (8). It clearly shows that current are proportional to the scan rate. However, a small peak at 0.05V vs NHE shows that there is deviation from ideal capacitive behaviour which can

be attributed to the redox reaction due to active spots or untransformed 2H phase MoS₂. The idea of current increment with scan rate was discussed at the chapter 3. For 1T MoS₂, the current mostly increased proportionally to scan rate “v” similar to ideal capacitors.

Similarly, 0.5M Li₂SO₄ and K₂SO₄ were scanned with the same potential range of 0.5M Na₂SO₄, and reminiscent CV characteristics were observed for all three electrolytes (Fig. 6.2a). The capacitances were found to decrease in the order as $C_{Li_2SO_4} > C_{Na_2SO_4} > C_{K_2SO_4}$. Since all three electrolytes have the same anionic group, cations should be responsible for different capacitive behaviour.

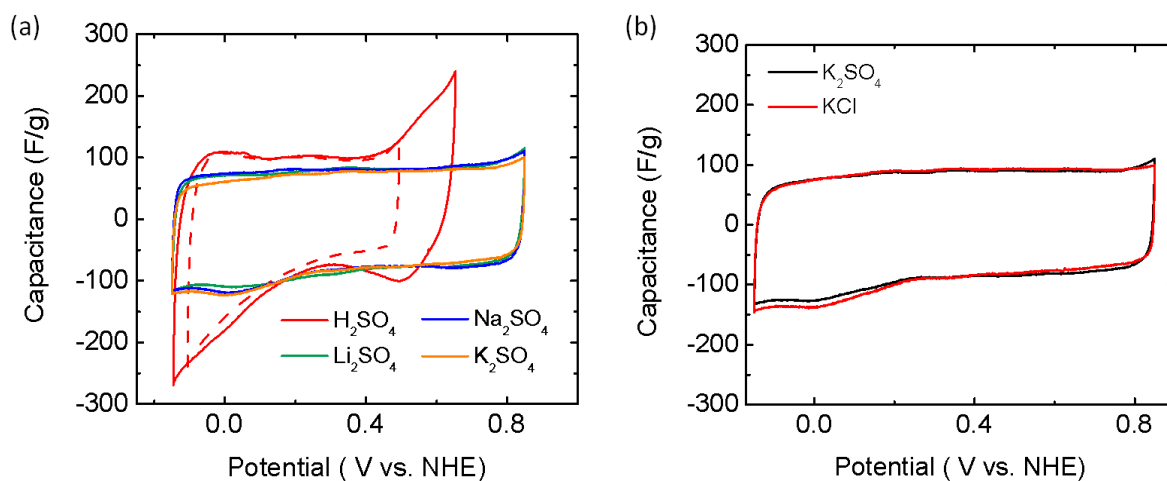


Figure 6.2. Comparison of the CV curves of 1T MoS₂ in electrolytes with different cation but the same anion (0.5M Li₂SO₄, Na₂SO₄ and K₂SO₄) (a), and electrolytes with different anion but the same cation (0.5 M K₂SO₄ and 1 M KCl) (b).

To elucidate whether the cations or anions intercalate into the electrodes, two electrolytes with different anions were tested. The CVs in K₂SO₄ and KCl are shown in Fig. 6.2b. It can be seen that the CVs for both electrolytes are nearly the same despite the

large difference in anion radii, suggesting that the cation is intercalating into the electrode.

6.1.1.2 In Acidic Electrolyte

In acidic electrolyte conditions (0.5M H_2SO_4), MoS_2 exhibits different CV characteristics as shown in Fig. 6.3. Unlike neutral electrolytes, there is more deviation from rectangular CV characteristics. The deviation starts below 0.3V and increases with increasing scan rate. This behaviour can be attributed to electrosorption of protons and pseudocapacitive charge storage contribution under acidic conditions. However, the potential range (0.6V) is much lower than that of neutral electrolytes (1V) because of early oxidation potential in acidic electrolytes. The low potential range is a limiting factor for MoS_2 in supercapacitor electrode applications.

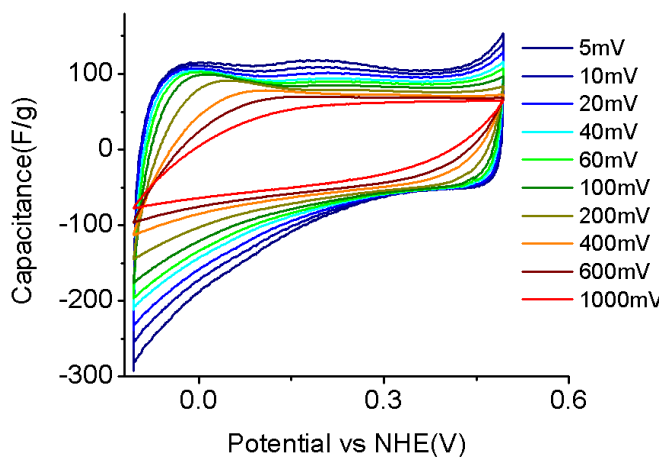


Figure 6.3. CV characteristic of 1T phase MoS_2 in 0.5M H_2SO_4 .

6.1.1.3 Thickness Effect

In order to determine whether the charge storage is a surface phenomenon or an intrinsic material behavior, electrodes were prepared with two different thicknesses; 1 μm and 5 μm . As shown in Fig. 6.4, 1T MoS_2 possess similar gravimetric capacitance for both thicknesses as studied. This result suggests that charge storage is not a surface phenomenon; it is an intrinsic material behavior where the gravimetric capacitance does not change with increasing film thickness.

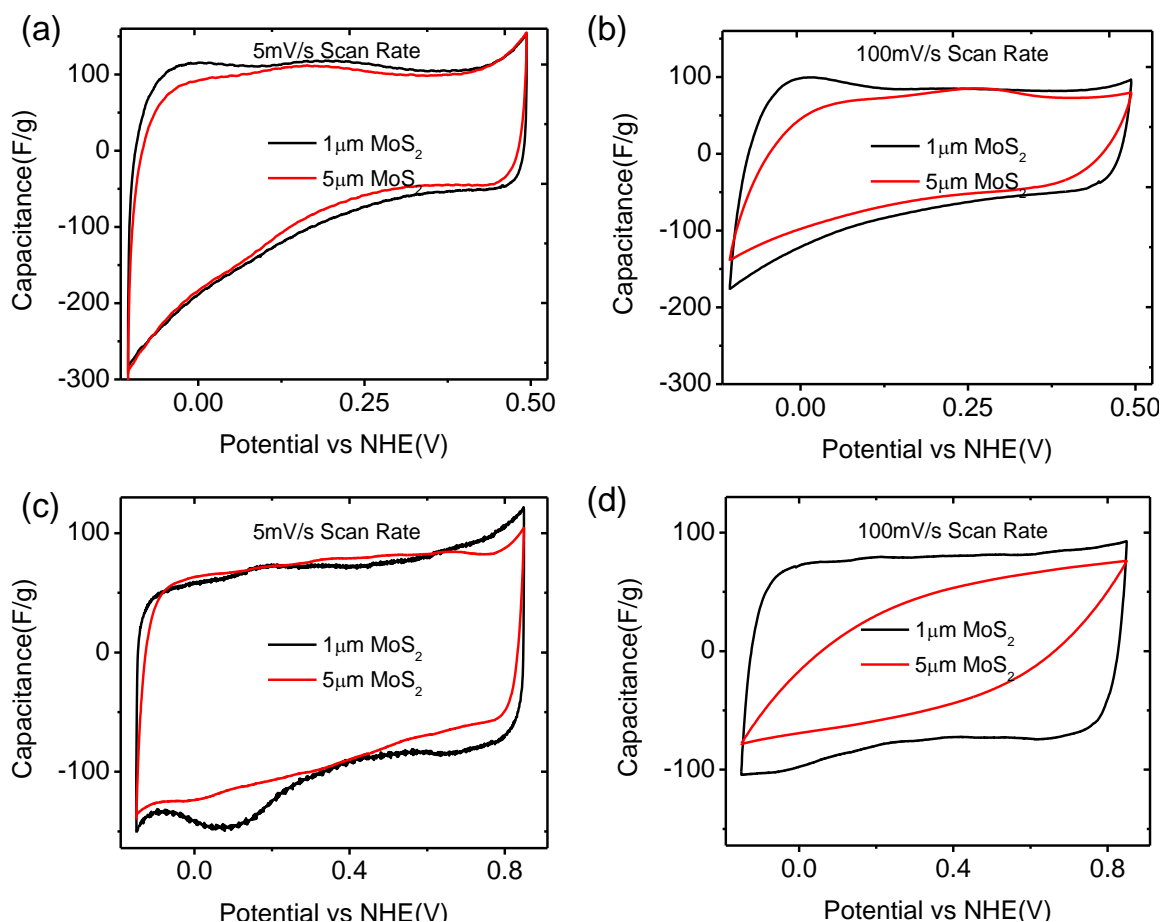


Figure 6.4. Thickness effect on the capacitance of 1T MoS_2 at 5mV/s scan rate (left) and 100mV/s scan rate (right) in H_2SO_4 (a,b) and in Li_2SO_4 (c,d).

However, the capacitance values decrease at higher scan rates. Since the thicker films possess longer pathway for ionic insertion, it is inevitable to have a longer charge response delay. Also thicker films have much lower capacitive performance with Li_2SO_4 electrolyte as compared to H_2SO_4 at high scan rates (see Fig. 6.4d). Since Li^+ ions are larger than protons, the thickness induces more reduction in the capacitance as compared to the case of protons.

6.1.1.4 2H and 1T phase MoS_2 Comparison

The 1T phase MoS_2 has 10^7 times higher conductivity than the 2H phase MoS_2 and one does expect a substantial impact of phase transformation on capacitance due to changes in conductivity. Therefore, it is important to show the difference in the capacitive behavior between the 2H and 1T phases.

As mentioned earlier, the chemical exfoliation and restacking process yielded 70% 1T phase of MoS_2 that showed high capacitance. In addition to high conductivity of metallic 1T phase of MoS_2 , the chemical exfoliation and restacking process results in a disturbed structure and negatively charged surface behavior. The material conductivity and surface properties were enhanced by chemical exfoliation and restacking process, resulting in properties that are both desired in electrochemical capacitors. Since there are two variables in the system (High conductivity and distorted structure), it is early to ascribe all observed phenomena to the phase transformation. Distinguishing the contribution of high conductivity and disturbed structure require further explanation.

As we discussed in Chapter 2, 1T MoS_2 gradually relaxes back to 2H phase if annealed at temperatures up to 300°C . Therefore one can obtain MoS_2 with various 1T/2H phase ratios by annealing 1T MoS_2 . We gradually anneal samples at 100°C ,

150°C, 200°C, 250°C and 300°C under inert argon atmosphere, and then measured the CV response (Fig. 6.5a). The annealing temperature dependence of capacitance is shown in Fig. 6.5b where it shows that the capacitance decreases with increasing annealing temperature.

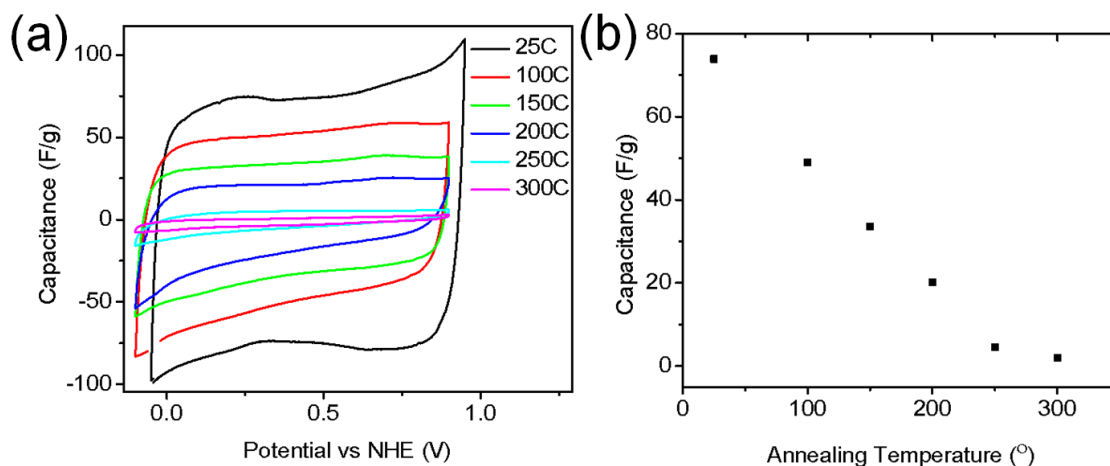


Figure 6.5. Comparison of the CVs and the capacitances at different annealing temperatures (a,b).

6.1.1.5 Comparison of All Aqueous Electrolytes

The specific capacitance as a function of the scan rate was tested for the different sulphate based electrolytes as summarized in Fig. 6.6. Also, the corresponding specific capacitance for each electrolyte, thickness and 2H phase MoS₂ were obtained. All the potentials were normalized with the hydrogen evolution potential in order to enable representative comparison since different electrolytes with different pH had to be compared. The concentration of cations in the electrolyte solutions was fixed at 1M in all experiments.

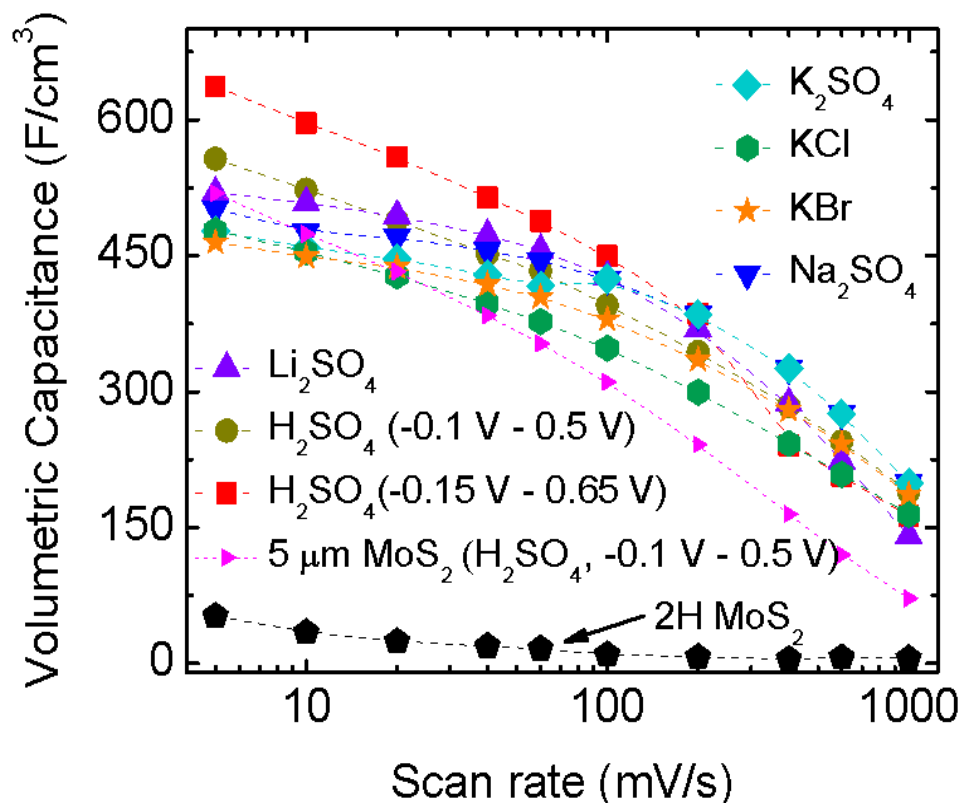


Figure 6.6. Evolution of the volumetric capacitance of the 1T phase MoS_2 electrodes with scan rate for different electrolytes for $1\mu\text{m}$ and $5\mu\text{m}$ thick films.

6.1.2 Galvanostatic Charging/discharging Measurements

Galvanostatic charging/discharging measurements were performed at 0.5, 1, 2, 4, 8 and 16A/g in Na_2SO_4 as shown in Fig. 6.7a. The response is close to ideal triangular capacitive behavior. The cyclability of the electrodes was studied by performing > 5000 cycles of charging/discharging at 2A/g current rate. Capacitive retention was found to be $> 93\%$ in neutral and $> 97\%$ in acidic electrolytes as shown in Fig. 6.7b. XPS analysis of 1T phase MoS_2 electrodes conducted after 5000 cycles did not show substantial change in the phase concentration. We also found coulombic efficiencies of 90-98% for various electrolytes at 2A/g charge/discharge current rate.

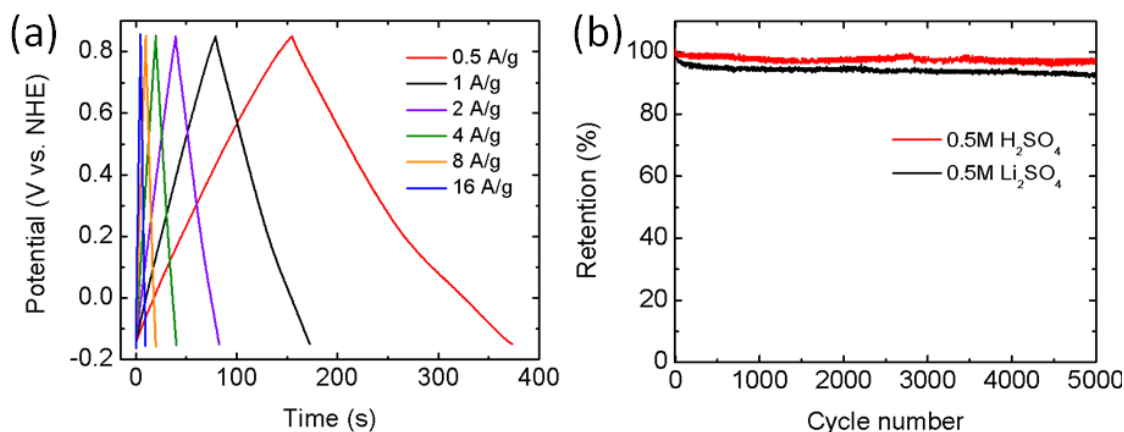


Figure 6.7. Galvanostatic cycles from 0.5 A/g to 16 A/g in Na_2SO_4 (a). Capacitance retention after 5000 cycles in 0.5 M Li_2SO_4 and H_2SO_4 (b).

6.1.3 Electrochemical Impedance Spectroscopy (EIS)

Nyquist plots were obtained with 10 mV amplitude (V_0) in the 10 mHz to 100 kHz frequency (ω) range at a fixed potential of 0.35 V vs. NHE (V_b) for each electrolyte where $V(t) = V_b + V_0 \sin(\omega t)$. As discussed in Chapter 3, the Nyquist plots show near-ideal capacitive behavior (Fig. 6.8) similar to the previously shown plots in Fig. 3.7. They also indicate that the impedance of the system depends on the type of electrolyte exhibiting semi circles at high frequencies and linear behavior at lower frequencies[97]. The semicircles correspond to parallel combination of the charge transfer resistance and double layer capacitance as illustrated in Fig. 3.7d. Since the resistance of the electrolyte increases on the order of $R_{\text{Li}_2\text{SO}_4} > R_{\text{Na}_2\text{SO}_4} > R_{\text{K}_2\text{SO}_4} > R_{\text{H}_2\text{SO}_4}$, the right shifted curves and larger semicircles are expected for higher resistivity in the system which is also observed in activated carbon[164] and MnO_2 [12]supercapacitor electrodes.

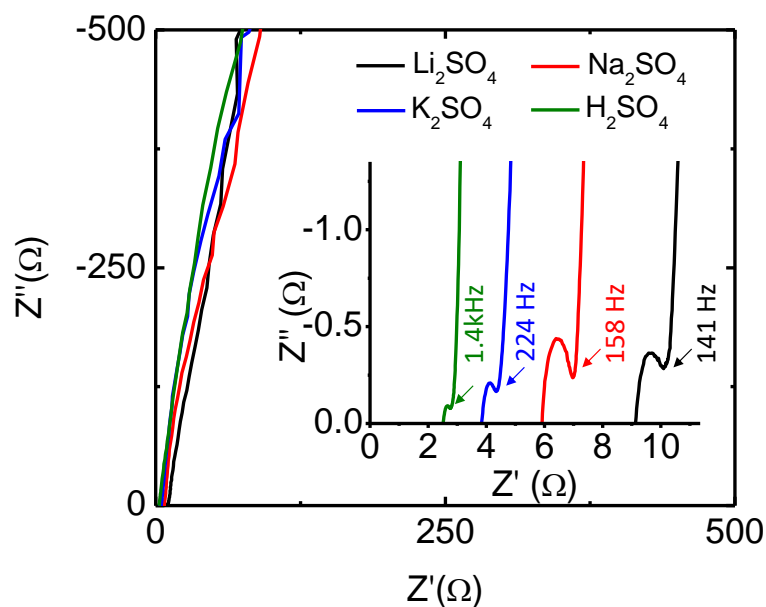


Figure 6.8. Nyquist plot of 1T MoS₂ electrode in 0.5 M H₂SO₄, K₂SO₄, Na₂SO₄ and Li₂SO₄ electrolyte solution.

We have shown the importance of 1T phase for capacitive nature of MoS₂ in previous section. CV analyses show that 1T phase of MoS₂ is highly capacitive, however 2H phase MoS₂ is 20 times less capacitive. We claimed that such high capacitance is a result of high conductivity of metallic phase. We performed EIS analysis on the gradually annealed MoS₂ samples with different annealing temperatures to better understand what has been observed in the conductivity studies.

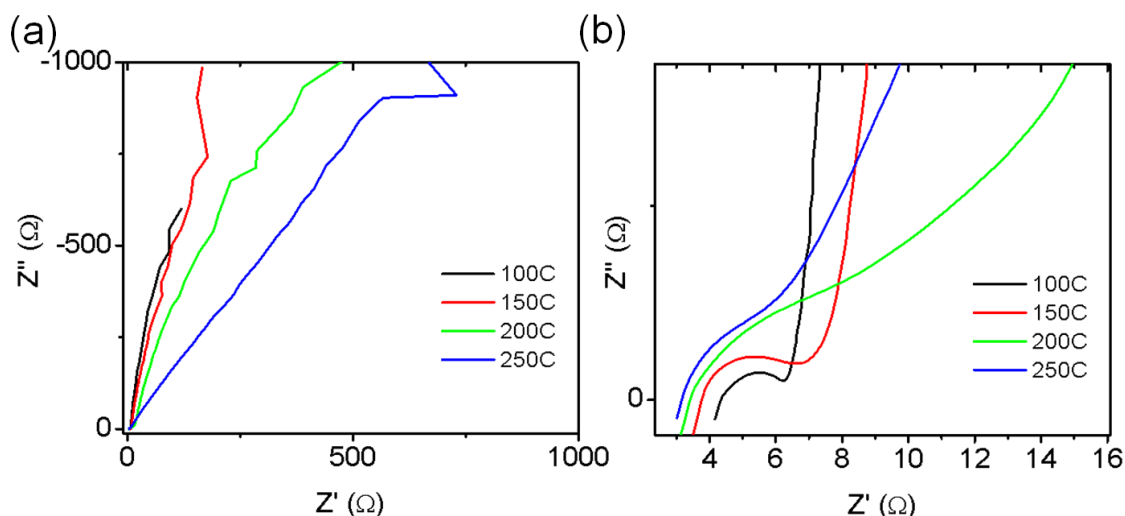


Figure 6.9. Nyquist plot for the transition from 1T MoS₂ electrode in 0.5 M H₂SO₄, K₂SO₄, Na₂SO₄ and Li₂SO₄ electrolyte solution at low frequencies (a) and at high frequencies (b).

As shown the Nyquist plot (Fig. 6.9) for annealed MoS₂ samples in 0.5 M Na₂SO₄ electrolyte, the vertical Nyquist curve at lower frequencies shift from capacitive to resistive behavior. The semicircles at higher frequencies expand upon increasing the annealing temperature indicating the charge transfer resistance is increasing.

6.1.4 Discussion for Aqueous Electrolytes

Cyclic voltammetry analysis shows that the 1T electrodes retain their high capacitance and its rectangular shape even at very high scan rates above 200 mV/s. These CV characteristics prove that 1T phase MoS₂ has capacitive behaviour (Fig. 6.1). In an effort to shed light to the charging mechanism, electrochemical analyses were conducted as a function of MoS₂ film thickness by using variety of electrolytes. Similar gravimetric capacitance behaviour with different thickness in 1T MoS₂ shows that charge storage does not only occur on the surface of the electrode, but also is an intrinsic behaviour.

Different electrolytes were compared according to their cation (Fig. 6.2a) or anion type (Fig.6.2b). Similar capacitive behaviour with the same cation and different anion based electrolytes tells us anions are not responsible for the capacitive performance (Fig.6.2b). On the other hand, different capacitive performance with different cation and similar anion based electrolytes shows us cations have substantial effect on capacitance (Fig. 6.2a). Hence, we can conclude that cations are responsible for the charge storage for 1T MoS₂.

The other finding from the comparison of CV data is that the 1T phase enhances the capacitive performance, because the chemical exfoliation and restacking process provides more conductive phase and also a disturbed structure. Both enhancements can play an important role for high charge storage capability. In order to clarify their contribution on the charge storage performance, restacked MoS₂ films were annealed at elevated temperature. Then MoS₂ films with different phase ratios were obtained. By comparing the effect of 1T/2H phase ratio on the specific capacitance, we can realize that there exist a correlation between the specific capacitance and 1T phase content of the MoS₂ film (Fig. 6.5). EIS analysis also show that the resistance of the electrodes increases with higher annealing temperatures (Fig. 6.9). The specific capacitance performances decrease with increasing 2H phase content of the MoS₂ electrode due to less conductive semiconductive nature 2H phase.

6.2 Electrochemical Behavior in Organic Electrolytes

To investigate the volumetric energy and power densities of the 1T phase MoS₂ electrodes, the electrochemical storage properties in non-aqueous electrolytes were measured. Specifically, the properties in TEA BF₄/MeCN and EMIM BF₄/MeCN organic electrolytes were evaluated because they offer a wide operating potential window of up to 3.5V. For this stage of the study, we used a two-electrode system. The device fabrication and the measurements were conducted in an Argon-filled glove box.

6.2.1 Cyclic Voltammetry

Typical CV curves in organic electrolyte are shown in Fig. 6.10(a,b). As in neutral electrolytes, rectangular CVs were observed at the measured scan rates in 1M TEA BF₄ in acetonitrile with 3V potential range. No distinct deviation from rectangular shape was observed even at high scan rates. Another organic electrolyte, EMIM BF₄ was also tested and CV curves were shown in Fig. 6.10b. Quasi-rectangular shapes are obtained at scan rates as high as 100 mV/s. The results show that the 1T phase MoS₂ behaves capacitively in organic electrolytes. The limiting factor for the potential range is the dissociation of organic electrolyte at very high potential ranges.

As summarized in Fig. 6.10c, the capacitance as high as 199 F/cm³ in TEABF₄/MeCN and 250 F/cm³ in EMIMBF₄/MeCN were obtained from 1T MoS₂ electrodes at 5mV/s. 1T MoS₂ exhibits stable capacitance behaviour even at higher scan rates.

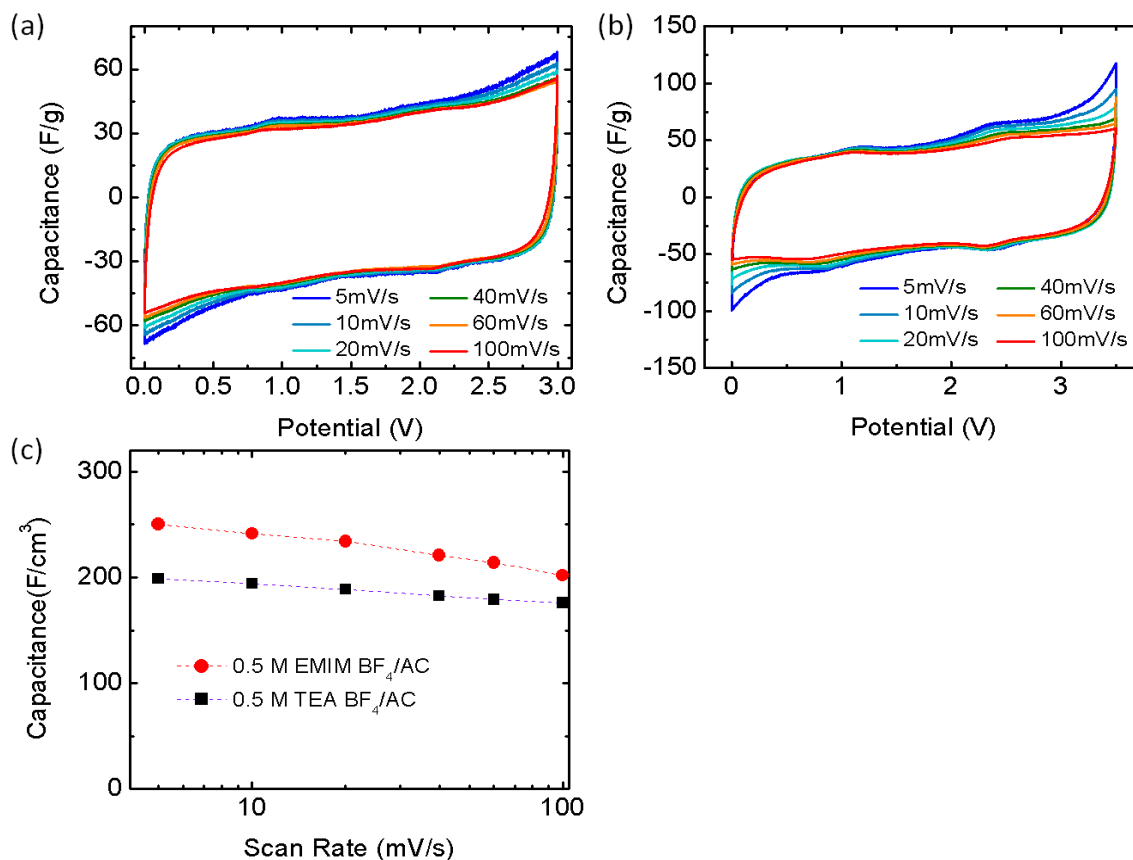


Figure 6.10. Electrochemical behaviour of 1T MoS₂ in organic electrolytes. Cyclic voltammetry curves in 1M TEA BF₄/MeCN (a). CV curves of 1T MoS₂ in 1M EMIM BF₄ in acetonitrile (b). Capacitance versus scan rates in TEA BF₄/MeCN and EMIM BF₄/MeCN electrolytes (c).

In complete contrast to response in aqueous electrolytes, initial charge storage behavior of 1T MoS₂ is very limited in organic electrolytes, although it increases gradually. As shown in Fig. 6.11, initial capacitance is as low as 1F/g, but it increases gradually with successive cycles until 50th cycles as shown in Fig. 6.11 and reaches the reported values.

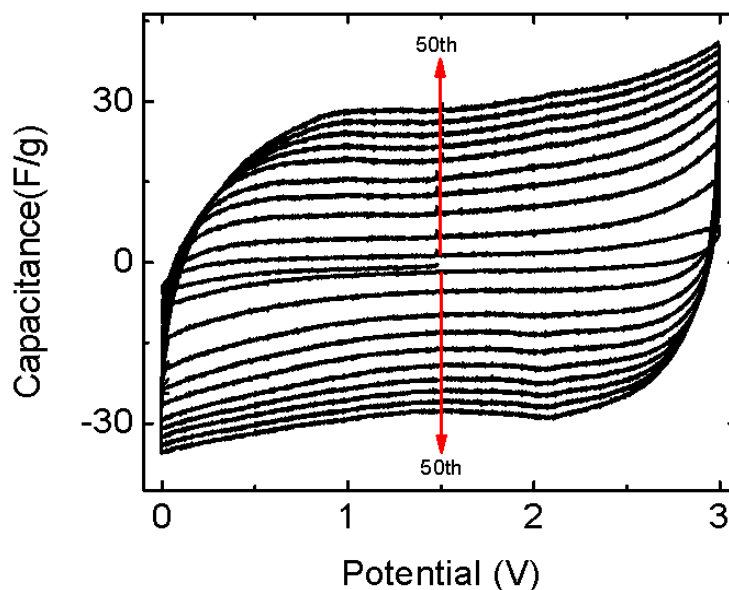


Figure 6.11. CV curves of 1T MoS₂ electrodes in TEA BF₄/AC at 100 mV/s obtained from the first 50 cycles showing the broadening of the CV response during the initial cycles.

6.2.2 Galvanostatic Charging/discharging Measurements

Galvanostatic charging/discharging measurements were conducted at current densities ranging from 0.5 A/g to 32 A/g with 1M TEA BF₄/MeCN, as shown in Fig. 6.12a. Charging/discharging curves show close to ideal behaviour with a minimal potential fall at higher discharging currents as indicated in the inset of Fig. 6.12a. The cycle stability of the 1T phase electrodes in organic electrolytes was tested for over 5000 cycles, as shown in Fig. 6.12b. We found that the electrodes retained over 90% of the initial capacitance after 5000 cycles.

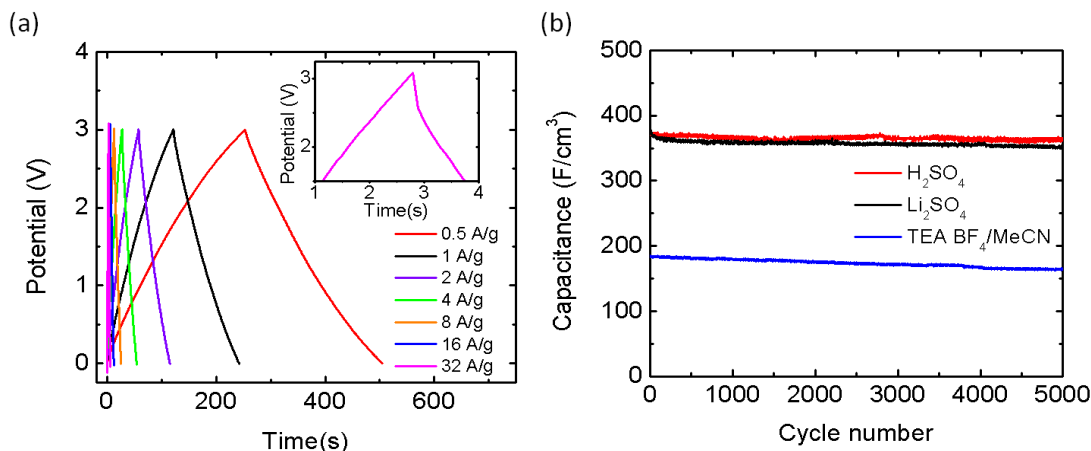


Figure 6.12. Galvanostatic charging and discharging curves in TEA BF₄/MeCN at 0.5 A/g and 32 A/g current rates (a). Inset shows the low internal resistance of the 1T MoS₂ electrodes in 1 M TEA BF₄/MeCN at 32 A/g. Capacitance retention during 5000 cycles in 1M TEA BF₄ with 0.5 M Li₂SO₄, H₂SO₄ (b)

6.2.3 Ragone Plot

In order to assess the charge storage performance, Ragone charts were plotted and compared with the literature (Fig. 6.13). For energy density and power density calculations, Eqn (14) and Eqn (16) were used. For the 1T phase of MoS₂ electrodes tested in aqueous electrolytes, we calculated an energy density of $\sim 0.016 \text{ Wh/cm}^3$ at a current density of 0.5 A/g, resulting in a power density of 0.62 W/cm^3 . At 16 A/g, the energy and power densities reached 0.011 Wh/cm^3 and 8.7 W/cm^3 , respectively. These values are very much higher than the ones obtained in organic electrolytes. We found an energy density and a power density as high as 0.11 Wh/cm^3 and 1.1 W/cm^3 at 0.5 A/g, respectively. At a higher current density of 32 A/g, these values changed to 0.051 Wh/cm^3 and 51 W/cm^3 , respectively.

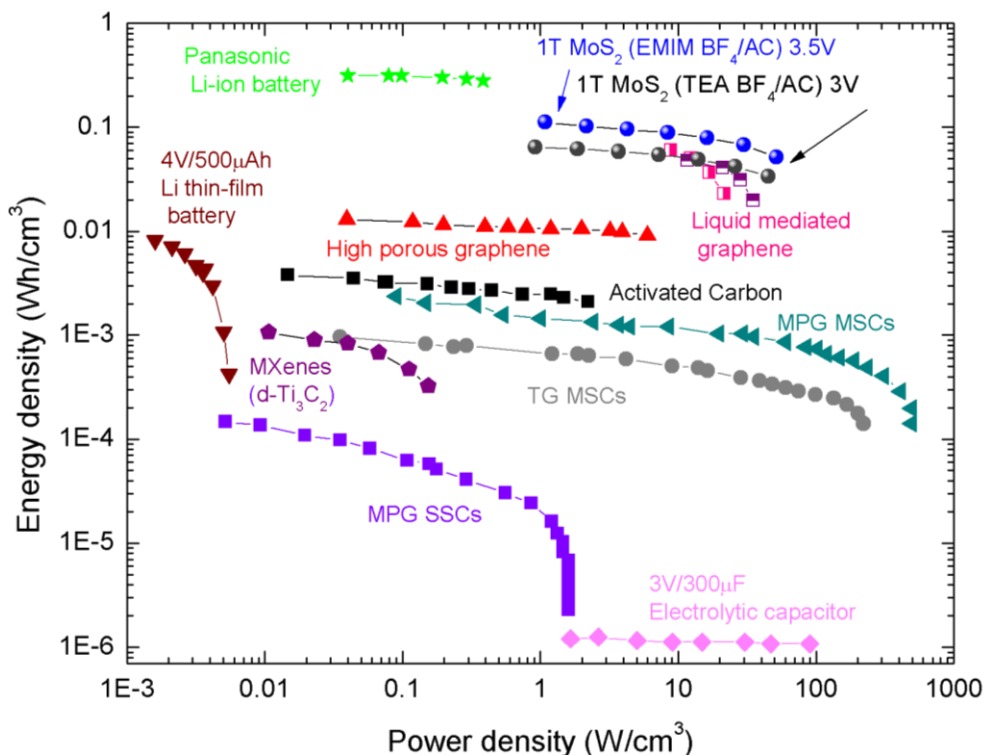


Figure 6.13. Ragone plot of the best volumetric power and volumetric energy densities reported from various materials including lithium thin film batteries [165], lithium thin batteries[166], graphene[15], [16], [167], MXenes[8] for comparison with those values obtained in this study for 1T phase MoS₂ electrodes.

6.2.4. Full Device Comparison with Thicker Electrode

As discussed in Chapter 3, a supercapacitor device is comprised of two active electrodes and two current collectors that are separated by a porous separator. Higher mass loading is desired in the active electrode as compared to other components in such supercapacitors. The mass loading achieved in abovementioned to date is low (~ 0.5 mg) and the thickness of the fabricated electrode is low (~ 1 μm) in comparison to the thickness of the separator (~ 25 μm). However, the overall mass and volume of the device have to be considered, including the separator and current collectors, so as to assess the

device performance correctly. That is so because the overall device performance efficiency is one order of magnitude lower than individual electrode. However, past attempts to fabricate thicker MoS₂ devices resulted in poor electrochemical performance in organic electrolytes.

The limiting factor to fabricate thicker MoS₂ film may either be ionic diffusion, electronic conductivity, or both. As it was shown in Fig. 6.4, thick MoS₂ films (5 μm) exhibited high capacitive behavior in aqueous electrolytes, but not in organic electrolytes, which is rather paradoxical. Therefore, electronic conductivity should not be a limiting factor for charge storage efficiency. Probably, such a paradox is because of the hydrophilic nature of 1T MoS₂. As discussed previously, organic electrolytes have hydrophobic behavior whereas 1T MoS₂ is hydrophilic and it slows down the wetting and initial charge storage in organic electrolytes. Thus, the diffusion is slower in an organic electrolyte in contrast to an aqueous electrolyte.

To enhance the electrochemical performance of MoS₂ in organic electrolytes, we incorporated a hydrophobic constituent, PTFE which might improve the electrochemical performance by increasing the diffusion rate in organic electrolyte. PTFE is frequently used as a binder in supercapacitor electrodes[59].

For a homogenous mixture, chemically exfoliated MoS₂ mixed with % 20 PTFE in DI water solution and sonicated for 5 minutes. Then, MoS₂/PTFE solution was restacked via vacuum filtration than transferred on a desired substrate as described in previous Chapter 4. We performed the electrochemical analysis in organic electrolyte, 1M EMIM BF₄/MeCN for 10 μm MoS₂ / PTFE composite as shown in Fig.6.14.

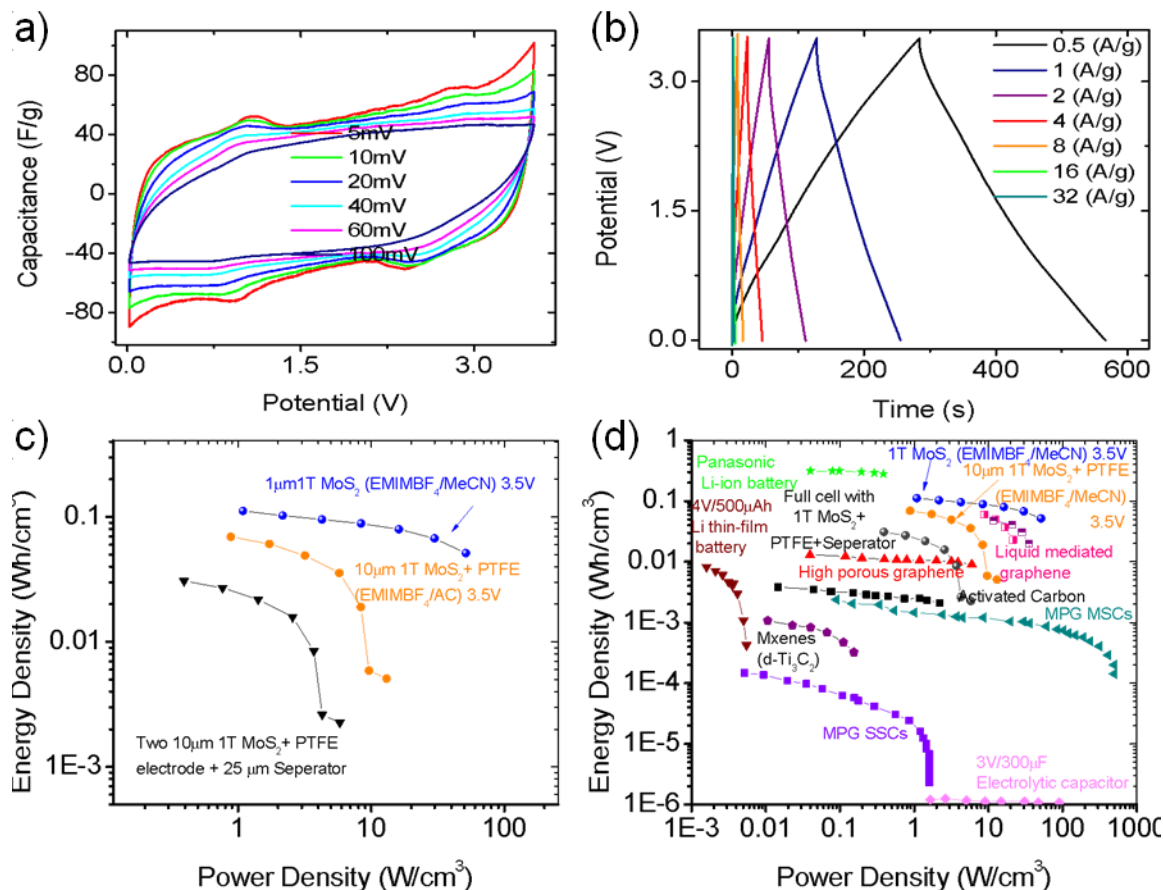


Figure 6.14. Electrochemical behaviour of 10 μm 1T phase MoS_2 / PTFE electrodes in 1M EMIM BF₄/MeCN. Cyclic voltammetry curves (a), galvanostatic charge/discharge curves (b) and Ragone plot 1 μm 1T phase MoS_2 , 10 μm 1T phase MoS_2 / PTFE and 20 μm 1T phase MoS_2 / PTFE with separator (c). The overall comparison of 1T phase MoS_2 / PTFE supercapacitor device with other materials (d).

6.2.5 Discussion for Organic Electrolytes

The 1T phase MoS₂ shows capacitive behaviour in the organic electrolytes with high potential ranges as plotted in Fig. 6.10. As compared to aqueous electrolytes, the organic electrolytes present lower capacitive performance. Since energy density is proportional to the square of the potential range, the organic electrolytes exhibit much higher energy density and power density performance compared to the aqueous electrolytes. The gravimetric capacitance values were found to be low as compared to carbon based supercapacitors, but the volumetric capacitances are higher than porous carbon due to high density of 1T MoS₂. Therefore, the volumetric energy density of 1T MoS₂ shows the highest reported value.

High power density is also required for supercapacitor applications. Since power density is inversely proportional to the internal resistance Eqn (5), the internal resistance should be as low as possible. The internal resistance were calculated from the potential fall during galvanostatic discharging. In Fig. 6.12a, the inset figure shows the potential drop at 32 A/g charging/discharging rate. Since the potential fall is very small even at very high current rate (32A/g), the internal resistance is very low for 1T MoS₂.

Interestingly, unlike in aqueous electrolyte, initial charge storage is very low, but increases gradually until it saturates (Fig. 46). Somehow the accessible surface area increases gradually and provides higher capacitance values. Gradual intercalation of ions into MoS₂ slabs might slowly enhance the accessible surface area. Since 1T MoS₂ is hydrophilic and the organic electrolytes are hydrophobic, the intercalation process is slow and diffusion limited.

6.3 Chapter Summary

It was shown that chemically exfoliated nanosheets of MoS₂ containing a high concentration of the 1T phase has extraordinarily high volumetric capacitance of nearly 700 F/cm³, that is substantially higher than carbons [15], [16] and Ti₃C₂ MXene layers [8]. For electrochemical tests, numerous aqueous electrolytes were used including H₂SO₄, Li₂SO₄, Na₂SO₄, K₂SO₄, KCl, etc. In addition to aqueous electrolytes, we have also tested organic electrolytes that are stable at much higher electrochemical potential ranges. The volumetric energy and power densities of 1T phase electrodes with organic electrolytes are among the highest reported thus far for any electrode material. The excellent electrochemical response of the phase engineered MoS₂ electrodes can be attributed to its hydrophilic response, excellent electrical conductivity, absence of binder.

Chapter 7.

7. Ex-situ XRD Analysis

1T MoS₂ exhibits very high volumetric capacitance in aqueous and organic electrolytes. Such high capacitance performance would normally requires high surface area, but the surface area of the restacked films were below 9 m²/g [168], which is substantially less than that for reduced graphene oxide [7], [16], [23]. XRD is known to be a very effective analytical tool for characterizing the inserted species in between MoS₂ layers[33]. As such ex-situ studies were conducted to gain insight into charge storage phenomena in MoS₂.

7.1 Experimental Setup for Ex-situ XRD Analysis

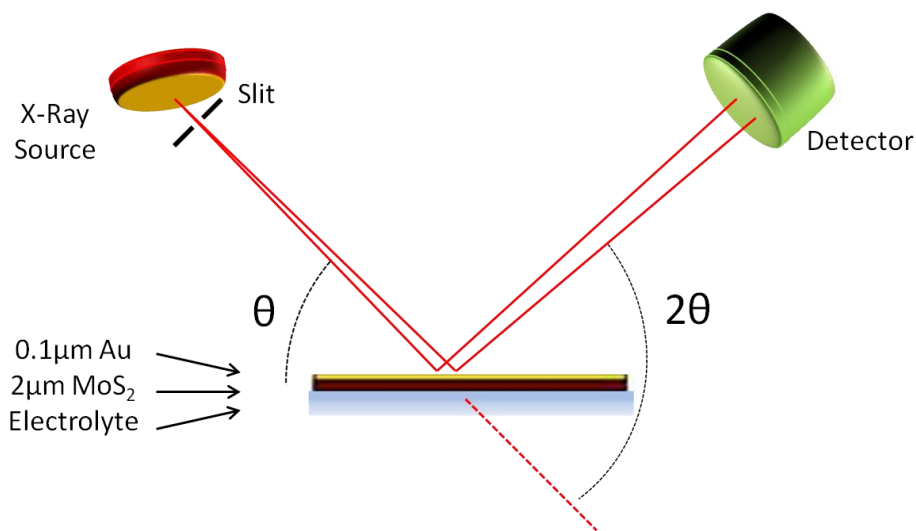


Figure 7.1. Schematic of the ex-situ X-ray diffractometer.

Ex-situ XRD analyses were performed by keeping the sample in electrolyte during XRD analysis to assess the peak shift due to vaporizing the water solvent as illustrated in Fig. 7.1. The layer spacing was calculated from the Bragg angle θ using

$$n\lambda = 2d \sin \theta \quad (31)$$

where n is the order of diffraction ($n=1$) of atomic plane, λ is the wavelength of the incident beam, θ is the angle between the beam and the atomic plane's normal, and d is the interplanar spacing.

7.2 Results & Discussion for Ex-situ XRD Analysis

Ex-situ XRD spectra of electrodes charged with different cations and protons in neutral, acidic and organic electrolytes are shown in Fig. 7.2. The intensity of the (002) peak at 14.4° in restacked MoS_2 decreases and the intensity of the (001) peak, which is an indication of interlayer expansion, increases. The new peak positions arising from expansion due to intercalation of hydrated cations are indicated in Fig. 7.2 as (001)* and (002)* to differentiate them from those obtained in non-intercalated materials. The (001)* and (002)* peak positions strongly depend on the intercalant type. The expansion of the spacing between the nanosheets due to intercalation is 6.63\AA , 6.09\AA , 3.7\AA , and 4.83\AA for Li_2SO_4 , Na_2SO_4 , K_2SO_4 and TEA BF_4 , respectively. Different spacings have been measured by X-ray diffraction can be attributed to hydrated cation intercalation. In the case of aqueous electrolyte, cations are coordinated with two water molecules for K^+ and six water molecules for Na^+ and Li^+ . In organic electrolytes, the cations are desolvated during the intercalation process giving a layer separation of 4.83\AA comparable to TEA^+ : 3.85\AA [169]. The presence of a shoulder at $\sim 16^\circ$ (black arrows) for as-exfoliated MoS_2

and electrodes intercalated in Li_2SO_4 , Na_2SO_4 and H_2SO_4 electrolytes is attributed to the presence of water bilayers[43].

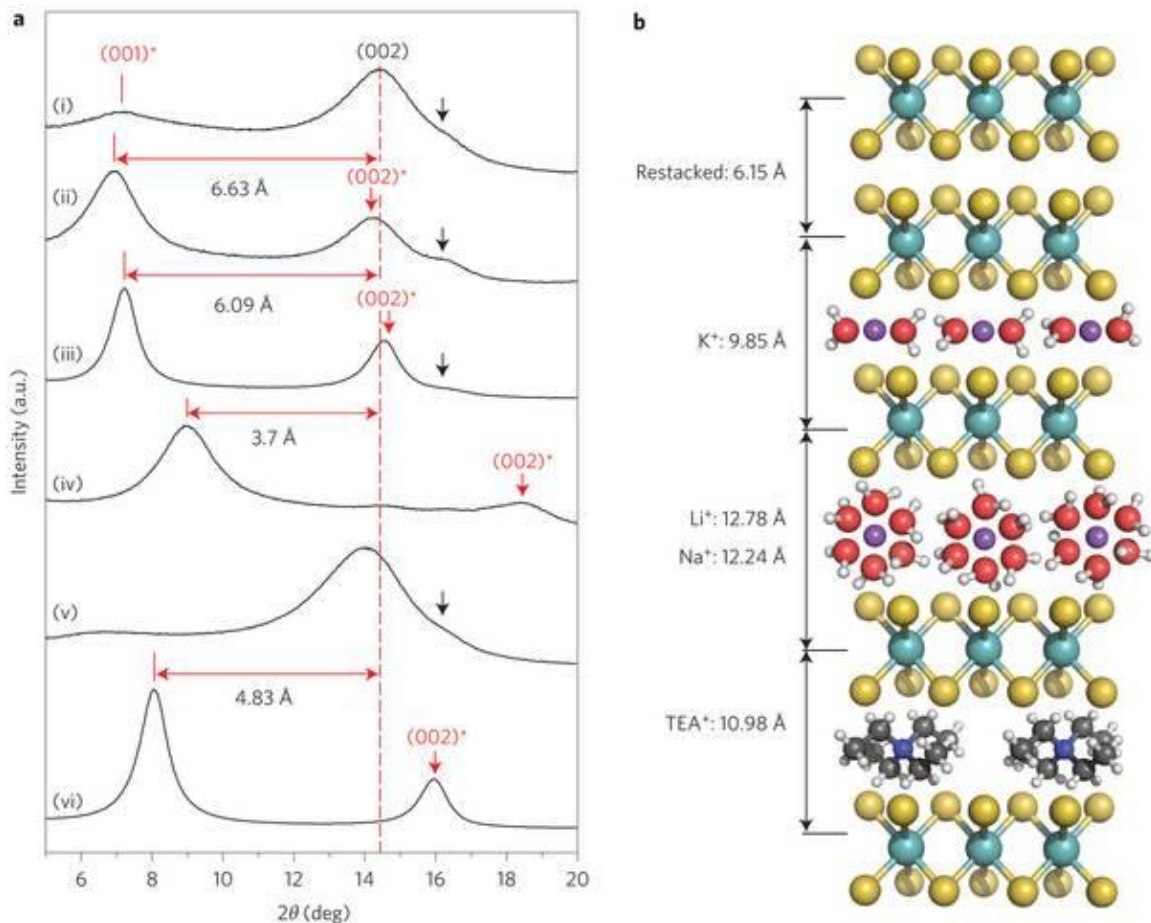


Figure 7.2. Ex-situ X-ray diffraction spectra from restacked 1T phase MoS₂ films. X-ray diffraction spectra from as-exfoliated 1T phase MoS₂ nanosheets (i) and cycled MoS₂ film (ii-v) in different sulfate-based electrolytes: Li_2SO_4 (ii), Na_2SO_4 (iii), K_2SO_4 (iv), H_2SO_4 (v) and TEA BF₄/MeCN organic electrolyte (vi). The characteristic (002) peak of restacked MoS₂ nanosheets is found at 14.4° for as-exfoliated 1T MoS₂ (a). Schematics of restacked non-intercalated and intercalated 1T MoS₂ nanosheets (b).

The expansion is higher than the hydrated cation sizes of $\text{Li}^+(\text{H}_2\text{O})_2$, $\text{Na}^+(\text{H}_2\text{O})_2$ and $\text{K}^+(\text{H}_2\text{O})$. Interestingly, unlike in neutral electrolytes, the (001) peak is absent after charging in H_2SO_4 . This is attributed to the fact that smaller protons can easily diffuse between the interlayers in restacked MoS_2 without causing substantial expansion. A small shift is however observed in the position of the (002) peak after proton intercalation in zero pH electrolytes. This can be correlated to adsorption on 1T phase MoS_2 after charging, and is consistent with the shape of the CV curve in Fig. 7.2. In the case of organic electrolytes, a similar expansion has been observed with strong (001)* and (002)* peaks at 8° and 15.9° , as shown in Fig. 50(vi).

The observed expansion is consistent with previous XRD and NMR studies of MoS_2 alkali metal intercalated compounds [43], [46], [170]. The results support that cations are dynamically intercalated through the interlayer of 1T MoS_2 . This dynamic intercalation process enhances the accessible surface area of the electrolyte. Thus, intercalation is found to be responsible for charge storage capacity, while restacked MoS_2 shows very low surface area. The absence of (002) at 14.4° in restacked MoS_2 after intercalation in TEA BF_4/MeCN suggests that the 1T phase MoS_2 electrodes are fully intercalated with the organic electrolyte. For such systems, the effective surface area is closer to the theoretical surface area than the measured surface area ($9 \text{ m}^2/\text{g}$). Selective cation intercalation into the layered 1T MoS_2 is a peculiar phenomenon. Since 2H phase MoS_2 layers do not let any substance into the layered structure except high energy lithium (butyl-lithium) which is what we have used already for chemical intercalation process. Previous studies demonstrate that 1T phase is stabilized by charge transfer from the butyl group of the organolithium exfoliation agent [36]. Zeta potential measurements [32] from

– 40 to – 50 mV indicate that the 1T MoS₂ nanosheets are negatively charged [32], [36] which may also facilitate the cation intercalation.

7.3 In-situ RAMAN Spectroscopy

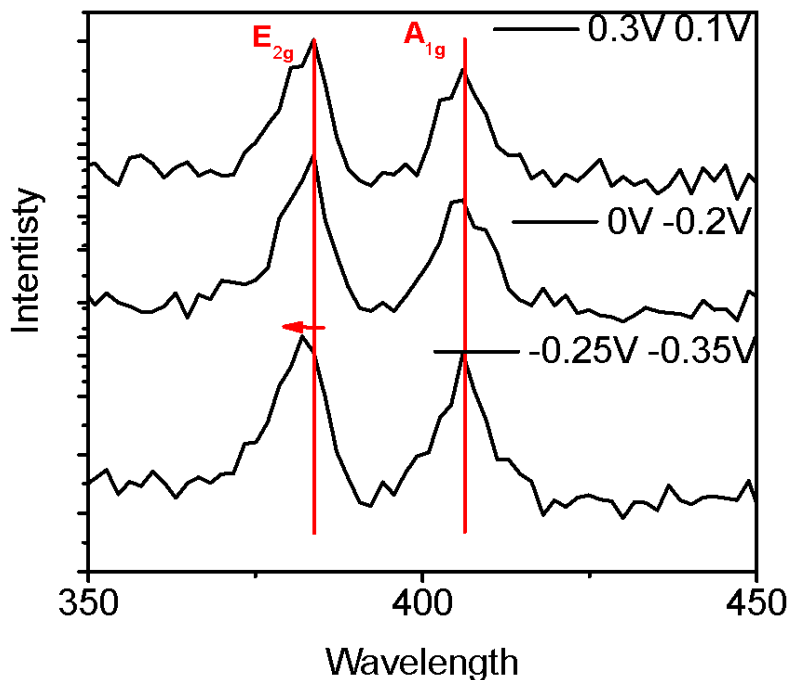


Figure 7.3. In-situ Raman spectra of 1T MoS₂, E_{1g} peak shift due to negatively charging.

In-situ RAMAN spectra were measured in immersion mode by using previously described[171] three electrode cell configuration in 0.5 M H₂SO₄. We used Renishaw inVia system with a 100X objective lens and 514 nm wavelength excitation laser beam source. In-situ RAMAN spectra were acquired at potential ranges where MoS₂ behave capacitive (-0.3 V to 0.3 V) with spectral range of 350 – 450 cm⁻¹.

At cathodic potentials cation insertion shift the E_{2g} peak to the lower energies and no distinct difference observed for A_{1g} peak. E_{2g} peak softening was attributed to change at the in-plane vibrations due to proton insertion. Similar behavior observed for WS₂ based supercapacitors[53].

7.4 Chapter Summary

Ex-situ XRD analyses were carried out in order to monitor the structural changes associated with intercalation. After all these investigations, we conclude that the charge storage mechanism based on the intercalation of cations (H^+ , Li^+ , Na^+ , and K^+) between the layers of the MoS_2 structure. The excellent electrochemical response of the phase engineered MoS_2 electrodes can be attributed to its hydrophilic response, excellent electrical conductivity, absence of binder, and accessibility of cations within the structure as indicated by the diminishing (002) peak in XRD. The results obtained to date open up interesting possibilities for phase engineering of exfoliated nanosheets in the realm of electrochemical storage properties in layered materials. These results were published as of the writing of this thesis dissertation [51].

Chapter 8

8 Electrochemical Actuation with MoS₂

At this point of this study, the charge storage properties of 1T phase MoS₂ were studied. And we established that the cation insertion/de-insertion process for 1T phase MoS₂, which also determines the interlayer separation, plays a critical role. It follows from the charge storage consideration that we expect some substantial volume change on the electrodes.

Therefore, the purpose of this study is to investigate the possible electrode expansion/contraction during electrochemical charge storage in 1T phase MoS₂. In other words, an attempt will be made to advance the understanding the macroscopic effects of ion intercalation. Results from such a study will be also helpful in engineering supercapacitor devices in order to protect them from mechanical degradation due to volumetric change. Besides, understanding basis of the driving force for the actuation is important to develop high performance actuation systems. To monitor the macroscopic changes on the active electrode, bimorph configuration has been used as demonstrated in Chapter 4.

8.1 Electrochemical Actuation Experimental Setup

To quantify the macroscopic dimensional change and analyze the mechanical behavior, the restacked 1T phase MoS₂ was transferred on a flexible substrate (gold and gold coated polyimide) in the form of bilayer or trilayer bending beam with 2 mm width

and 30 mm length with varying thickness of MoS₂ (1 μ m-8 μ m) and Kapton film (25 μ m-125 μ m). Any lateral dimensional change along the MoS₂ film will deflect the beam and transform into a curve. This method has been widely used to characterize electroactive polymer[147] and metal oxide actuators[51].

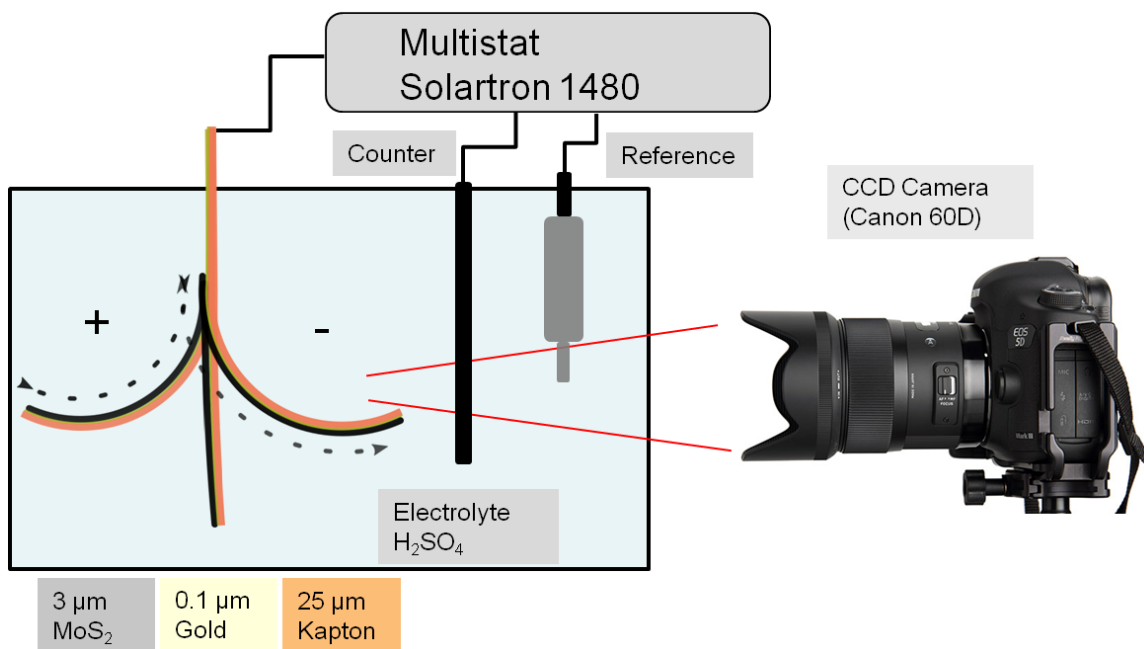


Figure 8.1. Schematics of experimental setup to track the change on the bending curvature of MoS₂ based bimorph actuator. The cross-section views of bended sample with different curvature conformations were illustrated. Positively charged MoS₂ film is shown as contracted bending inward and negatively charged MoS₂ expanded as bended outward.

To track the displacement and bending curvature, one end of the actuator was clamped as working electrode and the other end dipped vertically in a rectangular glass container filled with the electrolyte, 0.5M H₂SO₄. Then, the actuator electrodes were electrochemically induced by applying triangular and square waveform potential (-0.05 V and 0.55 V vs. NHE) by using Pt counter and calomel reference electrodes in three

electrodes configuration via Multistat (Solartron 1470). The free end displacement and the resolved bending degree of the actuator were recorded by charge coupled device (Canon 60D) as shown in Figure 1. Any slight change at the electrode curvature will be observed simultaneously with respect to electrochemical response in a resolution of 0.0001 mm^{-1} curvature change.

8.2 Electrochemical Induction and Mechanical Response (Bending Motion)

As shown in Fig. 8.2, MoS_2 electrodes subjected to a triangular wave potential (CV). The flexible electrodes were bended inwards at positive potential sweeping and outwards at negative potential sweeping. Up to 0.17 mm^{-1} curvature change has been observed with $8 \text{ }\mu\text{m}$ MoS_2 on $25 \text{ }\mu\text{m}$ Kapton film which is much higher than PPy based actuator[157] with similar configuration. Since the bending displacement is very high, the small angle approximation is not valid for the curvature calculation from tip end displacement. The curvature has been calculated directly via image processing by using MATLAB. This method will provide a simple method to elaborate in-situ macroscopic dimensional change in the MoS_2 film.

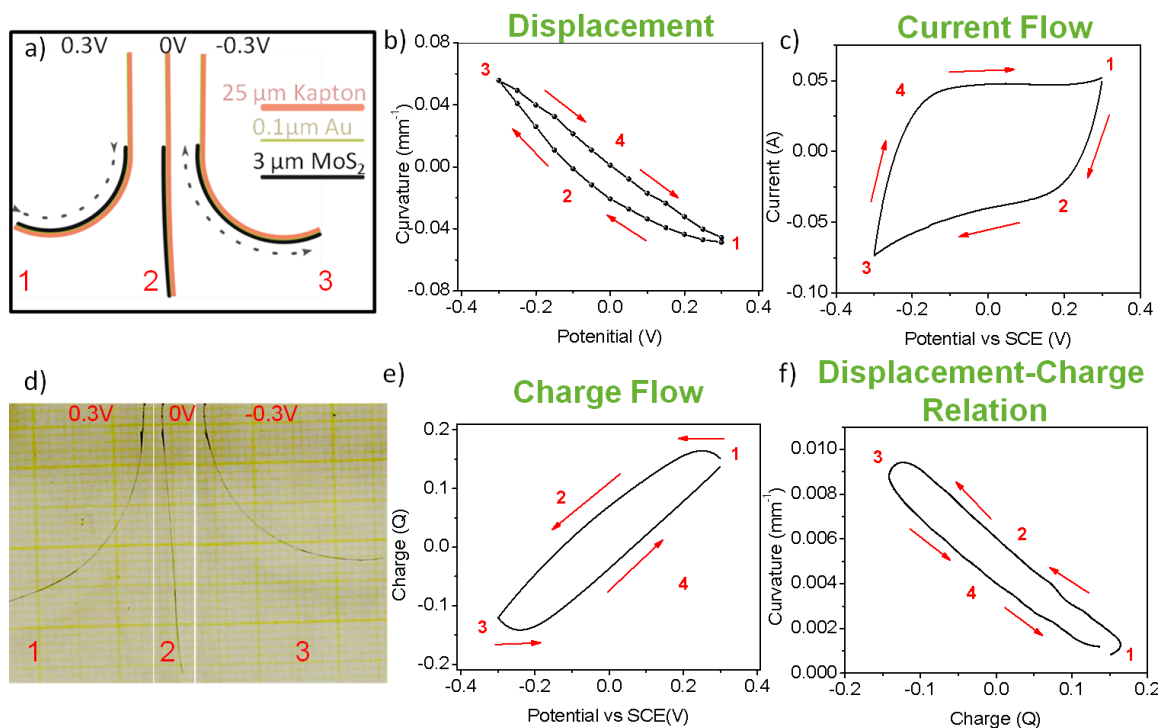


Figure 8.2. Schematics of bending beam (a). Curvature change with respect to potential change (b). Current flow due to potential sweep (5mV/s) (c). Optical images of curved bimorph actuator (d). Corresponding charge flow through electrode (e). The relation between capacitance and curvature (f).

By applying the potential gradient, the MoS₂ electrodes polarize and attract the ions leading a vast amount of charge flow through the electrode depending on the charge storage capacity. The direction of the current flow and corresponding charge flows and curvature changes with respect to potential are denoted with numbers (1-4) in Figure 8.2(c-f). During negative potential sweeping (1-3), the film bends toward MoS₂ layer indicating that in-plane expansion occurs on the MoS₂ film. And reversed positive potential sweeping (3-4-1) recovers the bending back to the initial position indicating that the deformation is reversible. According to our previous ex-situ XRD studies [51], during

negative potential sweeping, the protons insert and adsorbed into MoS_2 electrodes and during positive potential sweeping, the protons de-insert from the electrode. The amount of ion movement can be calculated from the current passage and corresponding curvature change can be correlated with it. The curvature change and the amount of charge flow changes linearly with respect to the applied potential as shown in Figure 8.2f. At negative potential sweeping (1-3), the cations flow through the electrode leading an in-plane expansion and at positive potential sweeping (3-5), the cations de-insert from the electrode leading an in-plane contraction in the film.

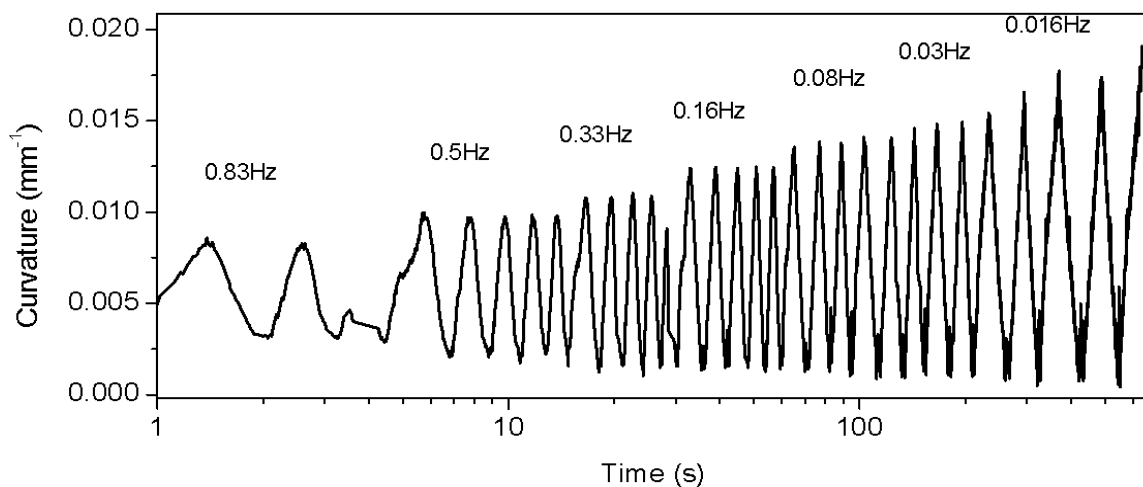


Figure 8.3. Time dependence of curvature change.

A typical triangular waveform potential sweeping at different frequencies and corresponding curvature change has been shown in Fig.8.3. Actuation is fully reversible in a broad frequency ranges and the magnitude of the actuation depends on the frequency. As shown in Figure 8.3, upon electrochemical charging on MoS_2 , actuation occurs and the corresponding charge storage with respect to scan rate in the form of differential capacitance curves in Chapter 6. Rectangular CV characteristics (Fig. 6.3) were observed

even at high scan rates indicating that proton insertion and de-insertion process is not diffusion limited which enables high actuation performance even at high rates. On the other hand, a deviation from rectangular behaviour was observed at slow scan rates which are attributed to diffusion limited redox reactions.

8.2.1 Capacitance vs Curvature Change

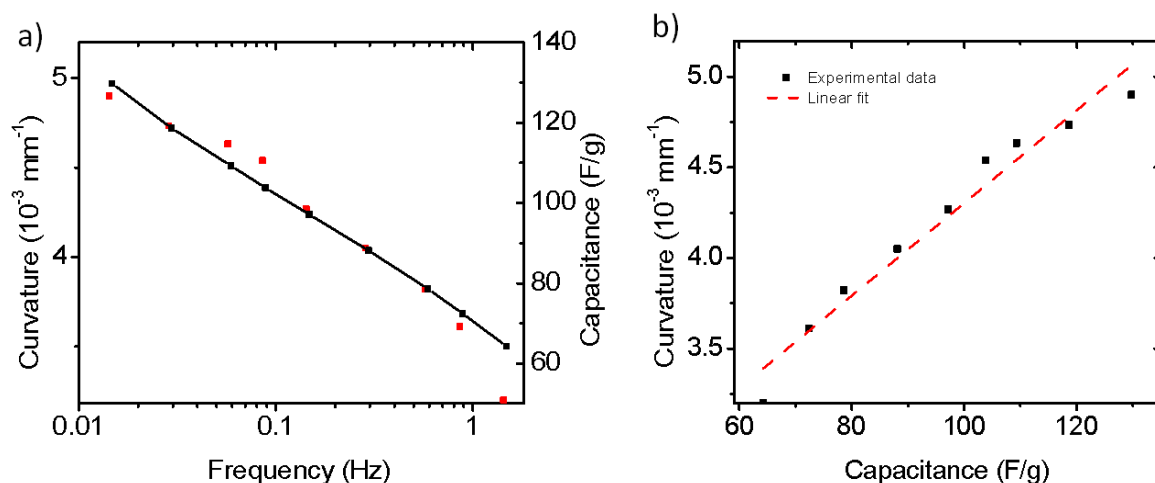


Figure 8.4. Curvature change and capacitance at different frequencies (a). The relation between actuation and capacitance (b).

It is clear that proton insertion at high rates is responsible for such high charge storage and actuation behavior. However, the contribution of diffusion limited faradaic reactions on the actuation behaviour is not clear. To elucidate whether the proton intercalation or the adsorption process induce the actuation during the charge storage, frequency dependence of actuation and capacitance results were plotted, then compared in Figure 8.4. There is a linear relation between curvature change and capacitance at moderate frequencies, but at lower frequencies, the actuation is lower than expected trajectory. It is known that faradic reactions contribute to the charge storage at slower

rates and the fall from the trajectory at low rates clarifies that the adsorption process does not contribute to the actuation. In addition, the actuation with respect to capacitance decreases at very high scan rates. The drag force increases with square of the speed of the beam which limits the actuation performance at high frequencies. Therefore, the fall at higher rates is attributed to the increase in the drag force exerted by the aqueous medium.

8.2.2 Potential Range vs Curvature Change

Since the Faradaic reactions are potential dependent process, the electrochemical charge storage at different potential ranges will give more prominent approach to understand the adsorption contribution on the actuation behaviour. Then, the potential were swept at different ranges starting from 0.1V to 0.6V potential difference. As shown in Figure 4, the capacitance and the curvature increase by expanding the potential range. This approach also shows that the proton adsorption is not important for actuation.

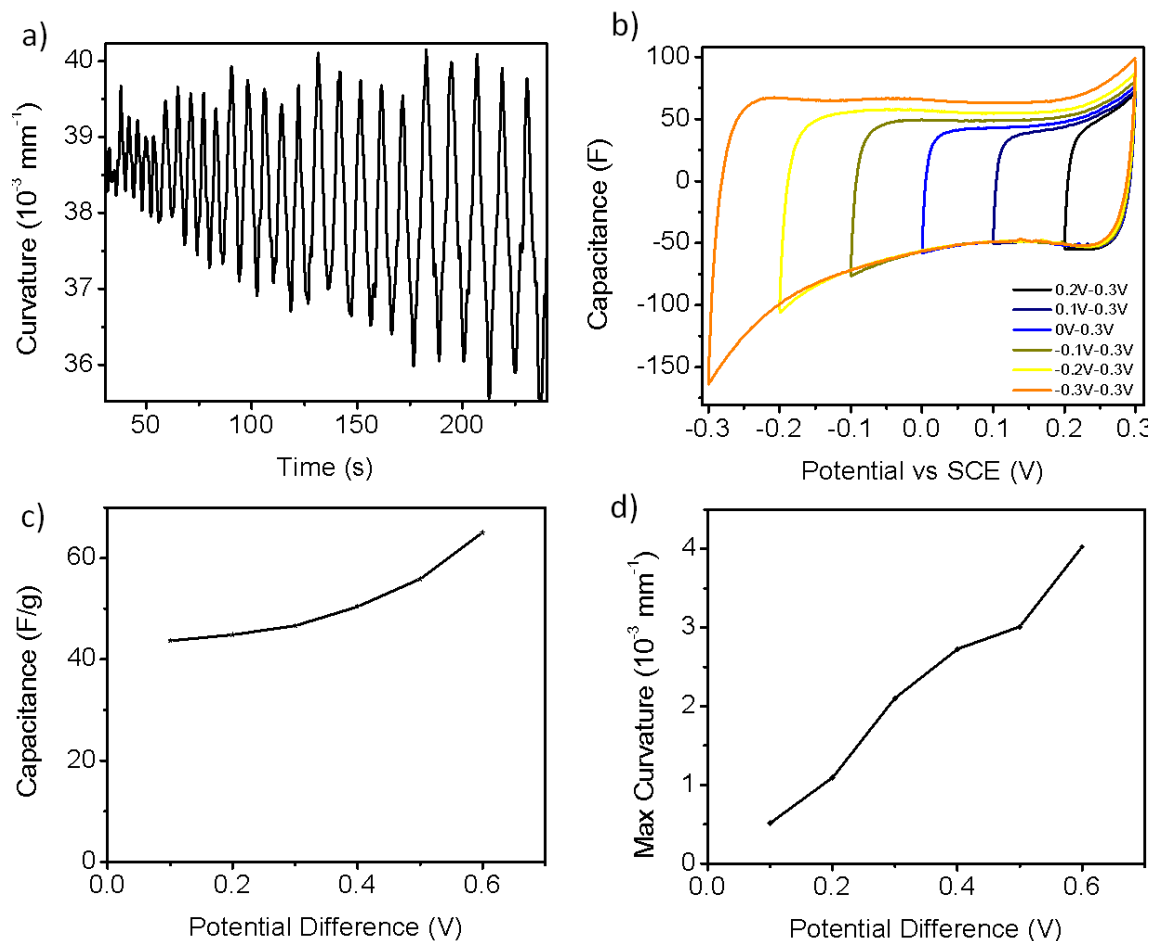


Figure 8.5. The curvature change at different potential ranges (a). Corresponding CV characteristics (b). Capacitance with respect to potential range (c). The relation between potential range and curvature change (d).

Secondly, a square wave potential was applied at different potentials to observe the effect of potential on the actuation behaviour (Fig. 8.6). In this approach, electrodes were held at designated potentials for 60 seconds and the electrochemomechanical responses were recorded. Similarly, actuation increases with increasing potential range.

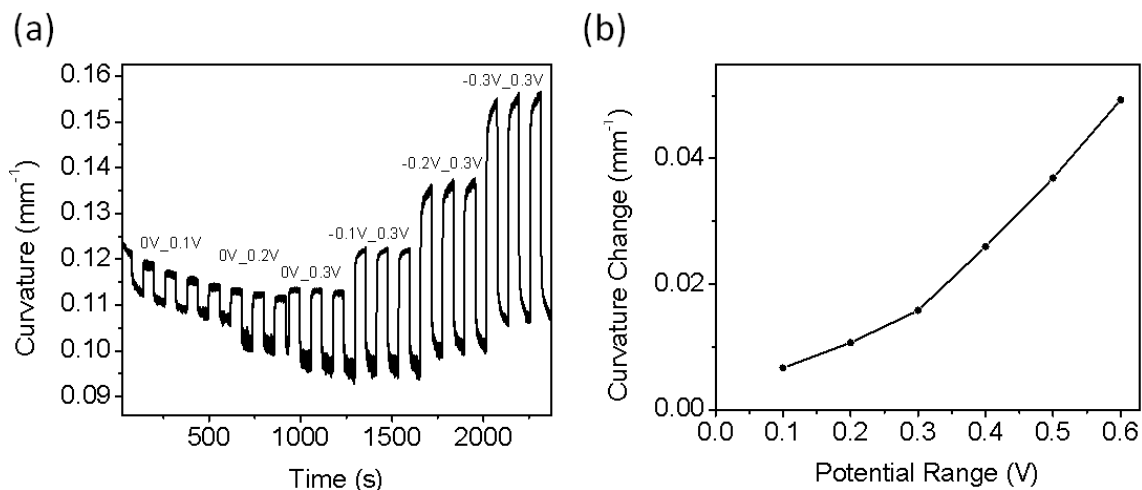


Figure 8.6. The curvature change via square wave potential at different potential ranges (a). The relation between potential range and curvature change (b).

8.2.3 Electrochemical Actuation in Neutral Electrolytes

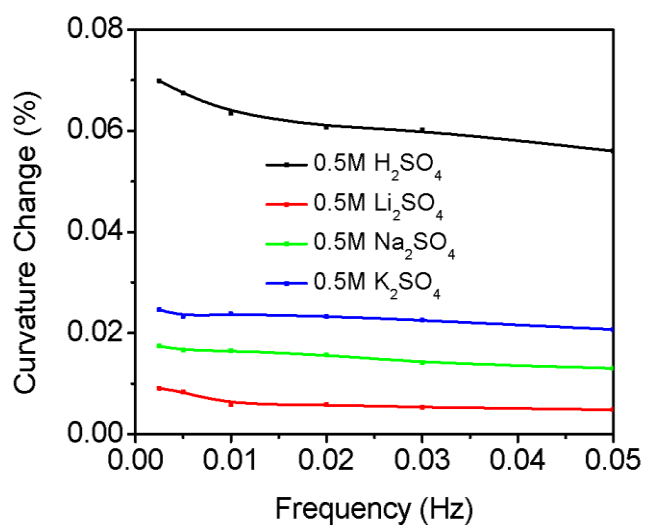


Figure 8.7. Comparison of the actuation behaviour in different electrolytes

Similar actuation measurements were performed in neutral electrolytes. Since cations intercalate between MoS₂ layers and cause an out-of-plane expansion, it is worth to conduct the same experiment for neutral electrolytes with different cation sizes. Interestingly, actuation performance decreases on the order of proton > K⁺ > Na⁺ > Li⁺. It indicates that cation type determines the actuation performance. Actuation decreases with increasing hydrated ion size which is contrary to the idea of pure intercalation expansion process.

8.2.4 Cycle Stability

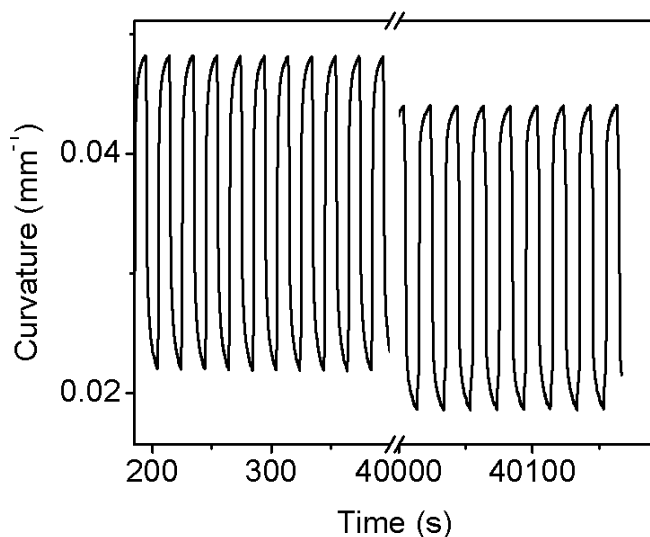


Figure 8.8 . Cycle stability test in 0.5 M H₂SO₄.

Stability of MoS₂ based bimorph actuators were measured over 5000 cycles for 24 hours. Curvature difference during square wave potential cycling did not change indicating that 1T phase MoS₂ mechanically robust for long term cycling.

8.3 Understanding the Bending Mechanics

Typical strain is the ratio of displacement to the free electrode length. However, in the beam bending configuration, the in-plane deformation is constraint by the passive layer. The misfit due to in-plane expansion leads to a residual force at the interface and curves the film. To elucidate the mechanics of bimorph actuators, previously constructed bending models were used (see Chapter 4). According to these models, the curvature is proportional to the induced strain on the active electrode as a function of thickness and elastic modulus of each layer. Here, strain is to be understood as elongation increment as a first order approximation as the structure of the actuator changes a time dependent fashion.

8.3.1 Thin Film Approximation (Stoney Approach)

The residual force can be calculated with thin film approximation (Stoney approach) where one layer is very thicker than the other layer ($t_1 \gg t_2$) [172]. To analyze the generated residual force and induced strain along the MoS₂ film, 3 μm restacked MoS₂ film was fabricated with 0.1 μm gold film in the bilayer form without Kapton layer. During the electrochemical induction, the bilayer film has been bended reversibly leading the curvature of 0.65 mm^{-1} with 0.3V potential difference as shown in Figure 5.b-c. Despite the low potential difference, the displacement is very large as expected due to low relative thickness ratios ($t_{\text{Au}} \ll t_{\text{MoS}_2}$). By using Stoney approach[172], the residual stress can be calculated by using Young's modulus of thicker film (MoS₂). However, there are no studies about mechanical behavior of chemically exfoliated and restacked 1T

MoS₂ and we still need the Young's modulus of restacked MoS₂ to derive the generated force due to electrochemical induction.

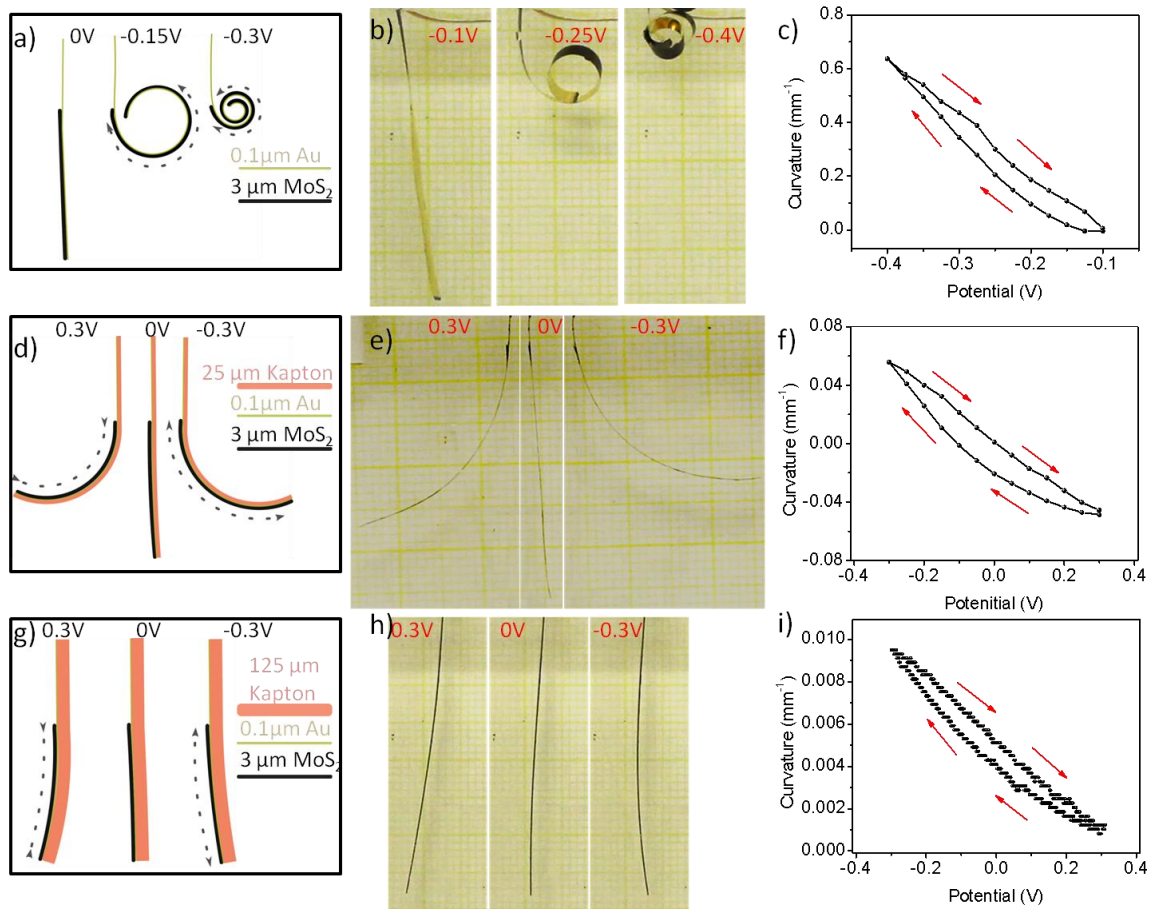


Figure 8.9. Snapshots of bending status of MoS₂/Au/Kapton trilayer actuators with different thickness variations induced electrochemically within ± 0.3 V potential. Relative bending degree increases with decreasing the thickness of passive layer, Kapton film, with respect to active layer, MoS₂. The electrodes located inside the electrolyte, 0.5M H₂SO₄.

Instead, I prepared the bimorph actuator with thicker substrate (125 μ m Kapton / 0.1 μ m Au / 3 μ m MoS₂) where the Young's modulus of thicker film is known (E_{Kapton} :

2.5 GPa) and thin film approximation ($t_{\text{MoS}_2} \ll t_{\text{Au+Kapton}}$) can be applied to calculate the residual forces generated by electrochemical actuation. As shown in Figure 5. h,i, the electrochemically induced trilayer actuator has bent with a curvature of 0.0085 mm^{-1} . According to Stoney equation, the residual stress generated by electrochemical actuation is 18.45 MPa along the interface assuming the gold layer is negligible. Considering the same stress has generated in the bilayer case ($0.1 \text{ } \mu\text{m Au} / 3 \text{ } \mu\text{m MoS}_2$), the Young's modulus of restacked MoS_2 is expected to be 2.3 GPa. If Hook's law is applicable, corresponding charge induced strain will be 0.8 %. However, it should be noted that in these mechanical analyses, the effect of thin layers assumed to be negligible. Besides, the residual stress was not included with bilayer (MoS_2/gold) configuration at higher potential ranges ($> 0.3 \text{ V}$) which might cause an overestimation. Because of these limitations, additional models need to be used to verify these findings as discussed next.

8.3.2 Multilayer Bending Models

Recent mechanical models[157] for multilayer actuators provide more accurate calculation and data fitting accounting the intermediate layers (Chapter 4 for detailed derivation). In these models, the induced-strain has a relationship to the curvature with respect to a coefficient (C_k) which is a factor of the elastic modulus and geometries of each layer. By changing the thicknesses of each layer, we can obtain the specific coefficients (C_k) for each case. The thicknesses and Young's modulus of each layer are known except Young's modulus of restacked MoS_2 film. Therefore, the coefficient can be obtained with a variable, Young's modulus of MoS_2 . Since the bending curvature is a

function of the thickness and the elastic modulus of each layer, the different thicknesses will give the insight to the relation between the thickness and curvature which reveal the effect of intrinsic strain and elastic modulus for MoS_2 . By preparing multiple samples with different thickness combinations, we can calculate the possible strain / elastic modulus curve. Since the strain and Young's modulus are constant, the corresponding curves will cross at the point where the actuation strain and elastic modulus of MoS_2 are real.

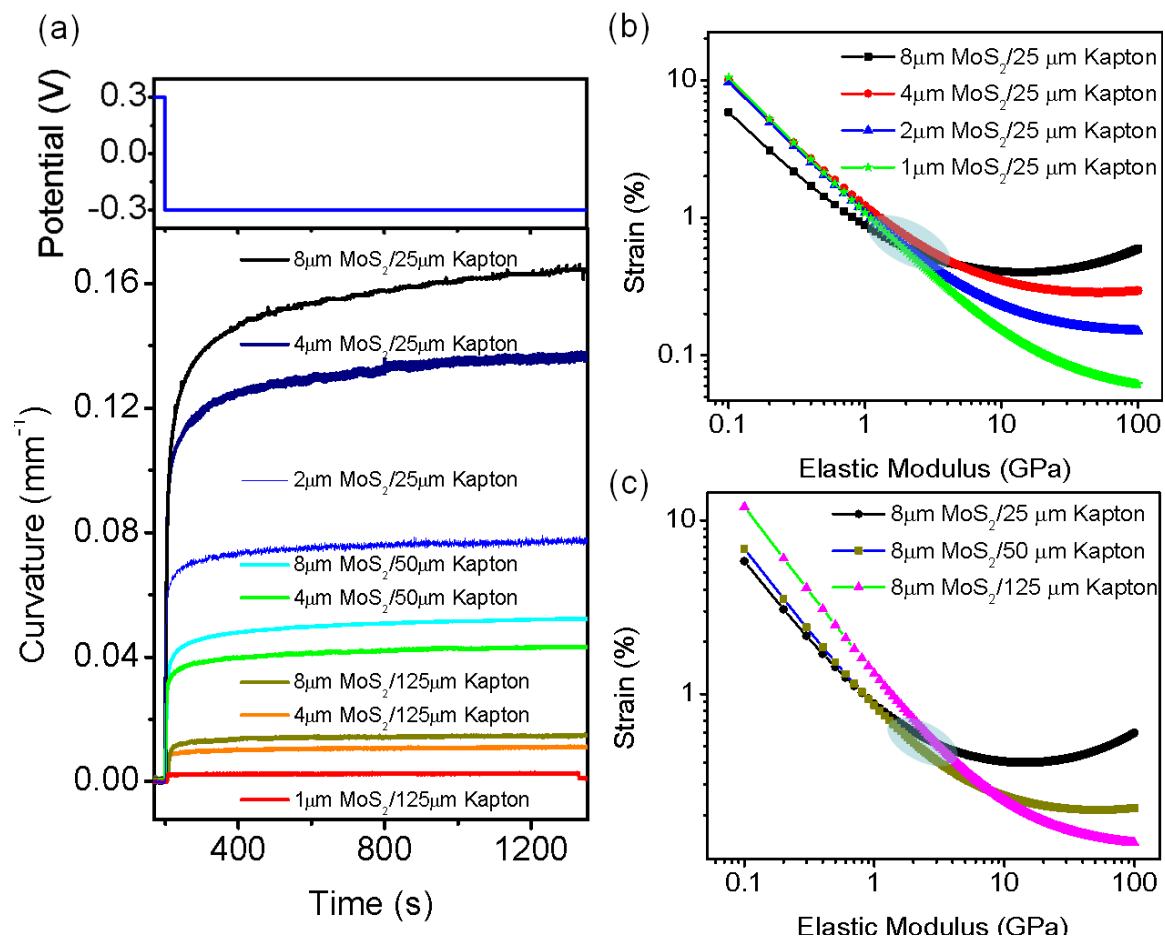


Figure 8.10. Maximum curvature values for different thickness ratios of $\text{MoS}_2/\text{Kapton}$ (8/25, 4/25, 2/25, 1/25, 8/50, 8/125, 4/50, 4/125 and 1/125)(a). Model

fitting to calculate elastic modulus of MoS₂ and strain according to abovementioned thickness configurations (b, c).

Accordingly, trilayer film were fabricated with varying thicknesses of 1 μm – 8 μm MoS₂, 25 μm -125 μm Kapton film and 0.1 μm gold layer. In order to minimize the charge response delay, the square wave potential was applied and electrodes hold at fixed potential for 1200 seconds. The curvature changes for each thickness configuration were shown in Figure 8.10a. The 8 μm MoS₂ film enable to bend 25 μm Kapton film with a curvature of up to 0.17 mm^{-1} which is higher than PPy based actuator[157]. Decreasing the ratios of $t_{\text{MoS}_2} / t_{\text{Kapton}}$, the bending curvature gradually decreased. The thicker active electrodes with respect to the passive electrodes lead to higher curvature change. By fitting the model for different thickness configurations, the relationship between charge-induced strain and Young's modulus of MoS₂ for each condition was obtained (Fig. 8.10b-c). When the magnitude of charge induced strain is around 0.5-0.8 %, the corresponding Young's modulus of restacked MoS₂ is around 1.8-3.8 GPa which are in good agreement with the results obtained from Stoney's approach. Following the Hook's Law, the strength of the material has been calculated 17 MPa. The generated stress from charge induced MoS₂ is much larger than mammalian muscle cell (0.3 MPa) and comparable to piezoelectric materials (40 MPa).

8.3.3 Mechanical Work Density

The performance of the electrochemical actuators are characterized by the work density per cycle which is generally determined by a product of Young's modulus and

square of the strain, $= \frac{1}{2} E_{eff} \varepsilon_{max}^2$. Considering Young's modulus of 1T phase MoS₂ is 183 GPa [55] and electrochemically induced strain is 0.8 %, work density of 5.9 MJ/m³ is expected which is the highest reported theoretical work density. However, effective modulus of restacked MoS₂ is two orders magnitude lower than individual layers due to weak interaction between layers. 2 - 4 GPa. Similar behaviour was observed for individual nanotubes and sheets. The corresponding work density for freely actuating MoS₂ film will be 74 kJ/m³ which is much higher than mammalian muscle cell 8 - 40 kJ/m³. The electrochemomechanical performance of 1T phase MoS₂ has been compared with other actuator systems and electrochemical actuator materials in Figure 8.11.

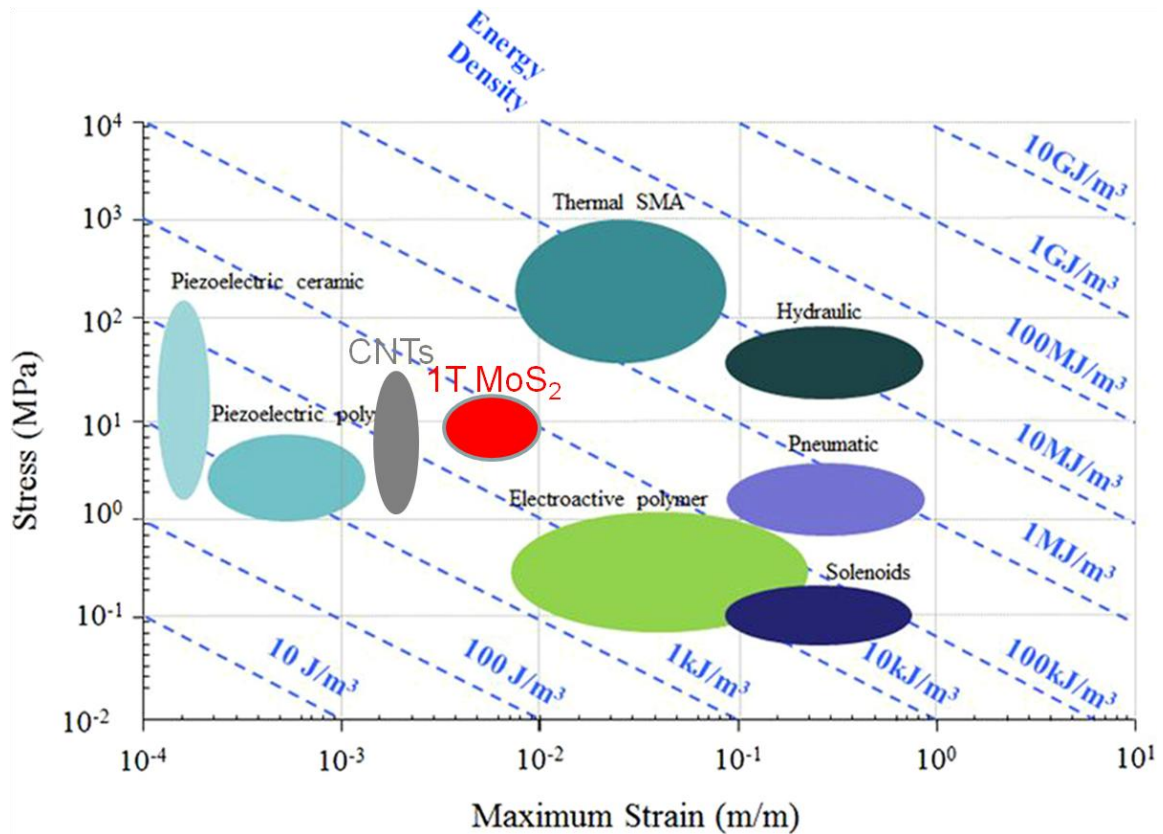


Figure 8.11. Comparison of actuator systems accounting maximum stress and strain performance[173], [174].

For multilayer bending beam, calculating the work density is more complicated. Bending beam work density is product of bending moment and bending curvature which is associated with the mechanical and geometric properties of each layer. More detailed information is given in Chapter 4. It was found that the work densities of bending beam are 20.5, 6.2 and 0.45 kJ/m³ for 8/25, 4/25 and 8/125 trilayered actuators. The work density of bimorph actuators are lower than free MoS₂ film due to the passive layer which constraint the active layer and bend the passive flexible body. By decreasing the thickness or using passive layer with a lower elastic modulus will increases the work density of multilayer actuators[157].

8.4 Inverted Series Connected Bimorph Actuator

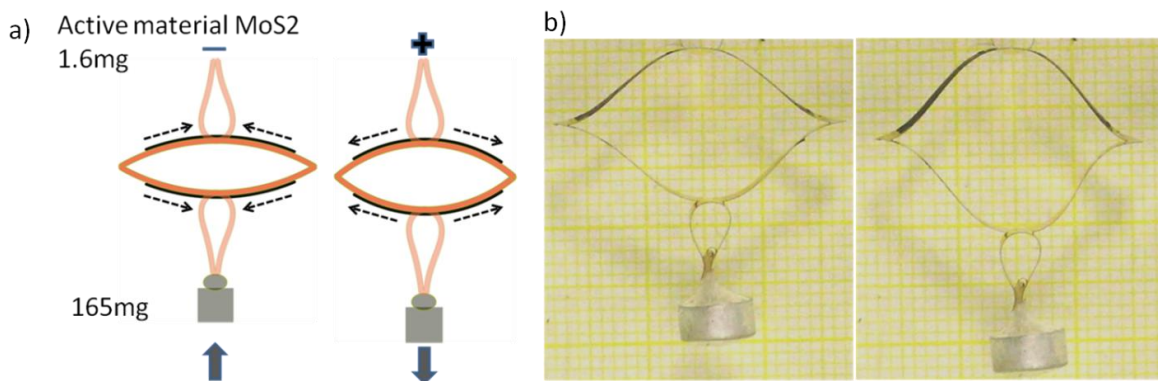


Figure 8.12. Schematic of inverted IPC bimorph actuator to lift up weight (a). Snapshot of IPC bimorph actuator lifting up 265 mg dead weight (b).

It was shown that electrochemically induced MoS_2 could generate enough force to bend the flexible Kapton film with large beam rotation. To utilize such electrochemomechanical property, an inverted-series-connected (ISC) electrochemical bimorph actuator[175] with MoS_2 film to convert the rotational motion to vertical displacement was designed. The (ISC) electrochemical bimorph actuator consists of two bimorph beams attached end to end where active film face opposite direction as shown in Figure 8.12. This alternating construction enables each bimorph actuator curved with an equal magnitude and cancels each other's rotational angle and convert to pure vertical displacement. With this configuration, under fixed load, ISC actuator behaves like elliptic spring and be considered as passive compliant actuator[176].

8.4.1 The Inverted S-beam Actuator Fabrication

To fabricate ISC bimorph actuator, 100 nm thin gold layer was deposited on both side of 25 μm Kapton film (Fig. 8.13(ii)). Gold coated film partially cropped as four strips (2 mm x 25 mm) leaving all four stripes connected as shown in Fig. 8.13(iii). And 4 μm MoS_2 films were transferred on the designated area on both sides. Then two ends were flipped over and attached to an alligator clip leaving the MoS_2 film outwards. The other two ends were flipped on the opposite way and hold the weight mass as shown in Figure 8.13(iv).

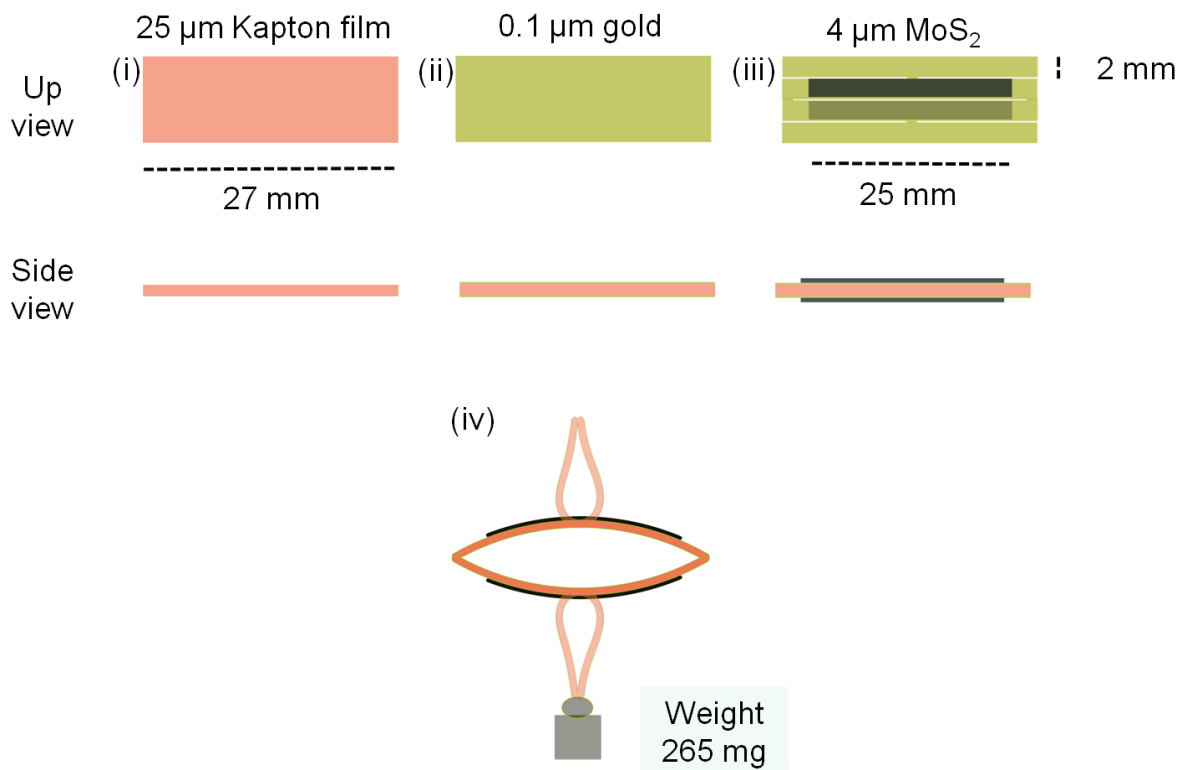


Figure 8.13. Schematics of IPC actuator fabrication. 25 μm Kapton film (i). 0.1 μm gold coating on both sides (ii). Gold coated kapton film cropped as illustrated and 25 mm x 2 mm MoS₂ film transferred on the designated area (iii). Pulling opposite sides with load attachment (iv).

8.4.2 The Inverted S-beam Actuator Energy Calculations

When the mass was hung, the IPC actuator acted like elliptic spring. In this configuration, the mass hanged on a spring in a liquid medium, the gravitational forces and buoyancy was balanced by extended spring. When a force applied on the system, it will displace the mass to find the equilibrium position. As shown in Fig. 8.14b, 1.6 mg MoS₂ lift up 265 mg load by electrochemical actuation with IPC design. We have shown

that charge induced MoS_2 bends the bimorph actuator which also deflect the spring and lift weight 100 times heavier than its own mass over 3 mm displacement.

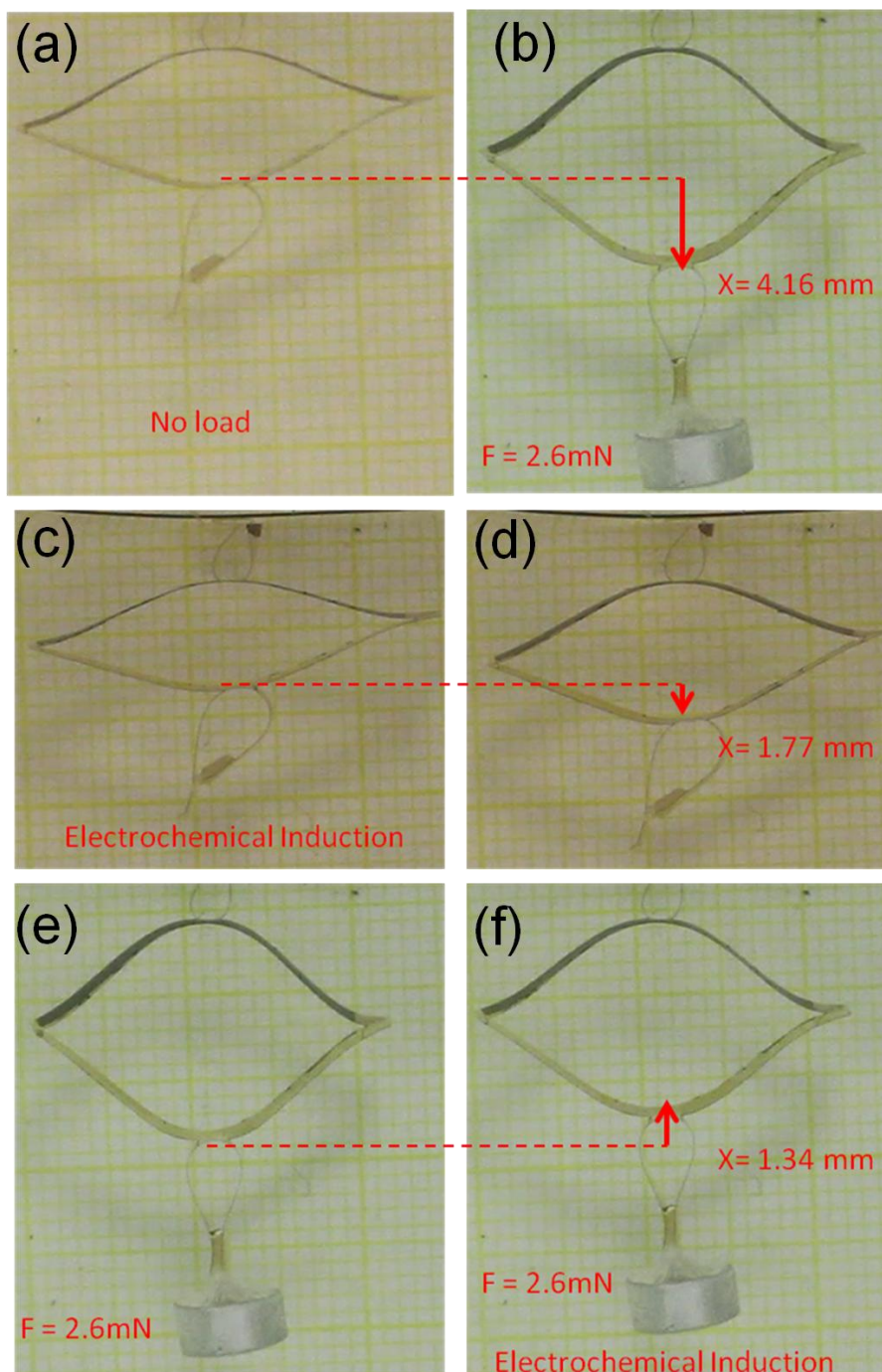


Figure 8.14. Stretched IPC actuator under loading (a,b), under electrochemical induction (c,d), under loading and electrochemical induction (e,f).

To calculate the mechanical force and energy driven by the electrochemical actuation, all of the forces exerting to the system by gravity, buoyancy, spring and friction were calculated when these forces are balanced in the equilibrium state, any additional force will disturb the system until it reaches the new equilibrium position. Gravitational force and buoyancy are calculated from the mass and volume of the hanged weight. These forces were balanced by the spring force and the spring constant is derived from the displacement as shown in Fig 8.14(a,b). The spring force (F) was calculated from Hook's law

$$F = -kx \quad (55)$$

and the work from

$$W = \int F(x)dx . \quad (56)$$

The IPC actuator was electrochemically actuated without the mass and a reversible actuation were observed with 9 mm displacement. Corresponding electrochemically induced force and work were calculated by using the spring constant. Then the mass loaded IPC actuator was electrochemically excited, and corresponding force and work were calculated.

A work density of 9 kJ/m³ electrochemomechanical energy was generated by inducing MoS₂ film as IPC bimorph actuator. This is consistent with previously calculated work density results using the multilayer bending beam model for 4 / 25 bimorph actuators. It is possible to enhance the work density by increasing the thickness

of MoS₂, decreasing the thickness of Kapton layer or using a less stiff flexible substrate[157].

The electromechanical coupling factor (k) is the ratio of mechanical work to stored energy density[132];

$$k^2 = \frac{\frac{1}{2}E\varepsilon^2}{\frac{1}{2}CV^2\rho} \quad (57)$$

By dividing the generated mechanical work to the stored energy, energy conversion efficiency were calculated and found 6 %.

8.5 Discussion

Chemically exfoliated and restacked 1T phase MoS₂ films were fabricated in the form of a bilayer and trilayer flexible electrode to study the macroscopic effects of charge storage. Triangular and square wave potentials were applied to induce charges on the electrodes. The charge flow through the electrode due to the polarization expands the electrode laterally leading a bending deformation on the flexible electrode (Fig. 8.2). Electrodes fully recover back to the original place during discharging process.

As shown in Fig. 8.2-8.9, the curvature change associated with the potential sweeping is fully reversible. However, a hysteresis was observed in the curvature vs potential curves. In previous Chapter 6, the cation intercalation process was established to explain the charge storage mechanism for 1T phase MoS₂. The intercalation is more favorable than deintercalation which makes discharging process slower than charging. Then, the hysteresis can be explained with the difference between diffusion rates of intercalation and deintercalation process. This phenomenon had been observed with PPy based

electrochemical actuators[147]. Negative surface charges on the MoS₂ might promote such behavior.

The actuation response is frequency dependent (Fig. 8.3). However, the actuation performance does not degrade a lot which is relatively higher than most of the other reported electrochemical actuator materials[138], [153]. Such high actuation response can be attributed to the high conductivity and charge storage capability of MoS₂. To elaborate on the effects of diffusion limited charge interaction, a controlled analysis has been conducted at different frequencies and potential ranges as shown in Fig.8.4-6. These findings suggest that diffusion limited faradaic reactions do not have substantial effect on the actuation.

Previous ex-situ XRD demonstrated that intercalation might contribute to the volume change during charge storage in alkaline electrolytes (Fig. 7.2). Since the MoS₂ layers were horizontally aligned on the flexible substrate and the lateral expansion is detectable with the actuator setup, we do not expect appreciable effect from the vertical expansion or contraction due to intercalation. However, one cannot completely rule out intercalation contribution to out-of-plane expansion because of in-plane rotations of the nanosheets leading to misalignment. Accordingly, we conduct similar measurements with neutral electrolytes, and reversible actuation is observed (Fig. 8.7). However magnitude of curvature change is much lower than acidic electrolytes. The actuation response decreases with increasing hydrated cation size unlike the expansion rates observed by XRD. Recent studies on intercalated layered materials show that cation intercalation effects the modulus of layered materials[177]. Cation intercalation increases the modulus and might increase the stiffness of MoS₂ electrodes.

The actuation performance of the MoS₂ based bimorph actuator is much higher than PPy based electroactive polymers considering similar actuator configuration[157]. For instance, the degree of curvature ($> 0.17 \text{ mm}^{-1}$) for 8 μm MoS₂ / 25 μm Kapton is three times higher than the curvature change ($> 0.045 \text{ mm}^{-1}$) for 9 μm PPy / 25 μm Kapton[157]. To elaborate on the mechanics of MoS₂ based bending beam, different models were used such as Stoney approach and multilayer beam bending model by using variety of different thickness combination. All of the results addressed similar results within the error limit, $\sim 0.6 \%$ strain with $\sim 3 \text{ GPa}$ modulus of elasticity for restacked MoS₂. Corresponding work densities are comparable with the piezoelectric materials and higher than muscle.

8.6 Chapter Summary

In this chapter, we analyzed the mechanical behaviour of MoS₂ under electrochemical induction with various electrolytes. Our findings indicate that charge storage induce a lateral force on the MoS₂ electrode depending on the cation size. In acidic conditions, electrochemical charge storage generates enough mechanical forces to bend flexible substrates and lift up masses 100 times heavier than its own weight for a few millimetres. High actuation performance even at high frequencies can be attributed to high conductivity of metallic 1T phase of MoS₂, comparably higher elastic modulus of MoS₂ layers and fast proton insertion into layered structure.

Chapter 9.

9.1 Future Work

To date, a methodology that is based on specialty electrochemical measurements, ex-situ XRD analyses and electromechanical analyses were developed in this study, which enabled one to analyze the electrochemical charge storage and actuation phenomena in 1T MoS₂. In the ensuing study, the very same methodology can be used for other LTMDs with a 1T phase such as 1T phase WS₂. In so doing, a comparative analysis between the 1T phases of MoS₂ and WS₂ can be carried out.

The cationic intercalation behavior seems to be apparent according to the ex-situ XRD analysis. However, it is not clear whether the intercalation is a continuous process. In other words, one does not know if 1T MoS₂ layers are stacking back to their initial condition during de-intercalation. In order to clarify the mechanism of the intercalation process thoroughly, ex-situ XRD analyses can be supplemented with in situ analyses. Such study will shed light on the actuation of MoS₂ associated with intercalation.

Finally, a comprehensive electrochemomechanical analysis in electrolyte with three electrode cell configuration was conducted. In the next evolution, one might consider to fabricate water free actuators with a gel electrolyte for enhanced actuator performance.

9.2 Conclusion

A new material, 1T phase MoS₂, was introduced as an electrode materials for high performance electrochemical supercapacitors and actuators. Our results indicate that the metallic 1T phase of MoS₂ have interesting electrochemical properties that can make it an attractive electrode material for both aqueous and organic supercapacitor devices. These electrochemical properties can be attributed to the intrinsic hydrophilicity and high electrical conductivity of 1T MoS₂, as well as the ability of the exfoliated nanosheets to intercalate various cations. Such dynamic layer expansion behavior can also be utilized to transform energy to mechanical energy. The findings of this study also indicate that charge storage induces a reversible in-plane electrode expansion up to 0.8 %, generating enough mechanical force to bend bimorph actuator and lift masses 100 times heavier than its own weight for a few millimetres. Such high actuation performance even at high frequencies can be attributed to high conductivity, fast proton insertion and comparably higher elastic modulus of MoS₂ layers.

References

- [1] P. Poizot, S. Laruelle, S. Grugeon, L. Dupont, and J.-M. Tarascon, "Nano-sized transition-metal oxides as negative-electrode materials for lithium-ion batteries," *Nature*, vol. 407, no. 6803, pp. 496–499, Sep. 2000.
- [2] E. Yoo, J. Kim, E. Hosono, H. Zhou, T. Kudo, and I. Honma, "Large Reversible Li Storage of Graphene Nanosheet Families for Use in Rechargeable Lithium Ion Batteries," *Nano Lett.*, vol. 8, no. 8, pp. 2277–2282, Aug. 2008.
- [3] B. E. Conway, "Transition from 'Supercapacitor' to 'Battery' Behavior in Electrochemical Energy Storage," *J. Electrochem. Soc.*, vol. 138, no. 6, p. 1539, 1991.
- [4] P. Simon and Y. Gogotsi, "Materials for electrochemical capacitors," *Nat. Mater.*, vol. 7, no. 11, pp. 845–854, Nov. 2008.
- [5] M. Ghidui, M. R. Lukatskaya, M.-Q. Zhao, Y. Gogotsi, and M. W. Barsoum, "Conductive two-dimensional titanium carbide 'clay' with high volumetric capacitance," *Nature*, Nov. 2014.
- [6] L. Mai, H. Li, Y. Zhao, L. Xu, X. Xu, Y. Luo, Z. Zhang, W. Ke, C. Niu, and Q. Zhang, "Fast Ionic Diffusion-Enabled Nanoflake Electrode by Spontaneous Electrochemical Pre-Intercalation for High-Performance Supercapacitor," *Sci. Rep.*, vol. 3, Apr. 2013.
- [7] M. D. Stoller, S. Park, Y. Zhu, J. An, and R. S. Ruoff, "Graphene-Based Ultracapacitors," *Nano Lett.*, vol. 8, no. 10, pp. 3498–3502, Oct. 2008.
- [8] M. R. Lukatskaya, O. Mashtalir, C. E. Ren, Y. Dall'Agnese, P. Rozier, P. L. Taberna, M. Naguib, P. Simon, M. W. Barsoum, and Y. Gogotsi, "Cation Intercalation and High Volumetric Capacitance of Two-Dimensional Titanium Carbide," *Science*, vol. 341, no. 6153, pp. 1502–1505, Sep. 2013.
- [9] R. Kötz and M. Carlen, "Principles and applications of electrochemical capacitors," *Electrochimica Acta*, vol. 45, no. 15–16, pp. 2483–2498, May 2000.
- [10] R. F. Service, "MATERIALS SCIENCE: New 'Supercapacitor' Promises to Pack More Electrical Punch," *Science*, vol. 313, no. 5789, pp. 902–902, Aug. 2006.
- [11] A. G. Pandolfo and A. F. Hollenkamp, "Carbon properties and their role in supercapacitors," *J. Power Sources*, vol. 157, no. 1, pp. 11–27, Jun. 2006.
- [12] M. Toupin, T. Brousse, and D. Bélanger, "Charge Storage Mechanism of MnO_2 Electrode Used in Aqueous Electrochemical Capacitor," *Chem. Mater.*, vol. 16, no. 16, pp. 3184–3190, Aug. 2004.
- [13] X. Lang, A. Hirata, T. Fujita, and M. Chen, "Nanoporous metal/oxide hybrid electrodes for electrochemical supercapacitors," *Nat. Nanotechnol.*, vol. 6, no. 4, pp. 232–236, Apr. 2011.
- [14] E. Raymundo-Piñero, K. Kierzek, J. Machnikowski, and F. Béguin, "Relationship between the nanoporous texture of activated carbons and their capacitance properties in different electrolytes," *Carbon*, vol. 44, no. 12, pp. 2498–2507, Oct. 2006.
- [15] X. Yang, C. Cheng, Y. Wang, L. Qiu, and D. Li, "Liquid-Mediated Dense Integration of Graphene Materials for Compact Capacitive Energy Storage," *Science*, vol. 341, no. 6145, pp. 534–537, Aug. 2013.
- [16] Y. Tao, X. Xie, W. Lv, D.-M. Tang, D. Kong, Z. Huang, H. Nishihara, T. Ishii, B. Li, D. Golberg, F. Kang, T. Kyotani, and Q.-H. Yang, "Towards ultrahigh volumetric capacitance: graphene derived highly dense but porous carbons for supercapacitors," *Sci. Rep.*, vol. 3, Oct. 2013.
- [17] J. Feng, X. Sun, C. Wu, L. Peng, C. Lin, S. Hu, J. Yang, and Y. Xie, "Metallic Few-Layered VS_2 Ultrathin Nanosheets: High Two-Dimensional Conductivity for In-Plane Supercapacitors," *J. Am. Chem. Soc.*, vol. 133, no. 44, pp. 17832–17838, Nov. 2011.

- [18] J. M. Soon and K. P. Loh, "Electrochemical Double-Layer Capacitance of MoS₂ Nanowall Films," *Electrochem. Solid-State Lett.*, vol. 10, no. 11, p. A250, 2007.
- [19] L. Cao, S. Yang, W. Gao, Z. Liu, Y. Gong, L. Ma, G. Shi, S. Lei, Y. Zhang, S. Zhang, R. Vajtai, and P. M. Ajayan, "Direct laser-patterned micro-supercapacitors from paintable MoS₂ films," *Small Wein. Bergstr. Ger.*, vol. 9, no. 17, pp. 2905–2910, Sep. 2013.
- [20] A. Ramadoss, T. Kim, G.-S. Kim, and S. J. Kim, "Enhanced activity of a hydrothermally synthesized mesoporous MoS₂ nanostructure for high performance supercapacitor applications," *New J. Chem.*, vol. 38, no. 6, p. 2379, 2014.
- [21] E. G. da Silveira Firmiano, A. C. Rabelo, C. J. Dalmascio, A. N. Pinheiro, E. C. Pereira, W. H. Schreiner, and E. R. Leite, "Supercapacitor Electrodes Obtained by Directly Bonding 2D MoS₂ on Reduced Graphene Oxide," *Adv. Energy Mater.*, vol. 4, no. 6, p. n/a-n/a, Apr. 2014.
- [22] K.-J. Huang, L. Wang, Y.-J. Liu, H.-B. Wang, Y.-M. Liu, and L.-L. Wang, "Synthesis of polyaniline/2-dimensional graphene analog MoS₂ composites for high-performance supercapacitor," *Electrochimica Acta*, vol. 109, pp. 587–594, Oct. 2013.
- [23] Y. Zhu, S. Murali, M. D. Stoller, K. J. Ganesh, W. Cai, P. J. Ferreira, A. Pirkle, R. M. Wallace, K. A. Cychoz, M. Thommes, D. Su, E. A. Stach, and R. S. Ruoff, "Carbon-Based Supercapacitors Produced by Activation of Graphene," *Science*, vol. 332, no. 6037, pp. 1537–1541, Jun. 2011.
- [24] G. Eda, H. Yamaguchi, D. Voiry, T. Fujita, M. Chen, and M. Chhowalla, "Photoluminescence from Chemically Exfoliated MoS₂," *Nano Lett.*, vol. 11, no. 12, pp. 5111–5116, Dec. 2011.
- [25] M. Chhowalla, H. S. Shin, G. Eda, L.-J. Li, K. P. Loh, and H. Zhang, "The chemistry of two-dimensional layered transition metal dichalcogenide nanosheets," *Nat. Chem.*, vol. 5, no. 4, pp. 263–275, Mar. 2013.
- [26] M. H. Cho, J. Ju, S. J. Kim, and H. Jang, "Tribological properties of solid lubricants (graphite, Sb₂S₃, MoS₂) for automotive brake friction materials," *Wear*, vol. 260, no. 7–8, pp. 855–860, Apr. 2006.
- [27] Q. H. Wang, K. Kalantar-Zadeh, A. Kis, J. N. Coleman, and M. S. Strano, "Electronics and optoelectronics of two-dimensional transition metal dichalcogenides," *Nat. Nanotechnol.*, vol. 7, no. 11, pp. 699–712, Nov. 2012.
- [28] S. Bertolazzi, J. Brivio, and A. Kis, "Stretching and Breaking of Ultrathin MoS₂," *ACS Nano*, vol. 5, no. 12, pp. 9703–9709, Dec. 2011.
- [29] B. Radisavljevic, A. Radenovic, J. Brivio, V. Giacometti, and A. Kis, "Single-layer MoS₂ transistors," *Nat. Nanotechnol.*, vol. 6, no. 3, pp. 147–150, Mar. 2011.
- [30] M. Fontana, T. Deppe, A. K. Boyd, M. Rinzan, A. Y. Liu, M. Paranjape, and P. Barbara, "Electron-hole transport and photovoltaic effect in gated MoS₂ Schottky junctions," *Sci. Rep.*, vol. 3, Apr. 2013.
- [31] L. Yang, S. Wang, J. Mao, J. Deng, Q. Gao, Y. Tang, and O. G. Schmidt, "Hierarchical MoS₂ /Polyaniline Nanowires with Excellent Electrochemical Performance for Lithium-Ion Batteries," *Adv. Mater.*, vol. 25, no. 8, pp. 1180–1184, Feb. 2013.
- [32] D. Voiry, M. Salehi, R. Silva, T. Fujita, M. Chen, T. Asefa, V. B. Shenoy, G. Eda, and M. Chhowalla, "Conducting MoS₂ Nanosheets as Catalysts for Hydrogen Evolution Reaction," *Nano Lett.*, vol. 13, no. 12, pp. 6222–6227, Dec. 2013.
- [33] E. Benavente, "Intercalation chemistry of molybdenum disulfide," *Coord. Chem. Rev.*, vol. 224, no. 1–2, pp. 87–109, Jan. 2002.

- [34] S. H. El-Mahalawy and B. L. Evans, "The thermal expansion of 2 *H* -MoS₂, 2 *H* -MoSe₂ and 2 *H* -WSe₂ between 20 and 800°C," *J. Appl. Crystallogr.*, vol. 9, no. 5, pp. 403–406, Oct. 1976.
- [35] V. Petkov, S. J. L. Billinge, P. Larson, S. D. Mahanti, T. Vogt, K. K. Rangan, and M. G. Kanatzidis, "Structure of nanocrystalline materials using atomic pair distribution function analysis: Study of LiMoS₂," *Phys. Rev. B*, vol. 65, no. 9, Feb. 2002.
- [36] J. Heising and M. G. Kanatzidis, "Exfoliated and Restacked MoS₂ and WS₂: Ionic or Neutral Species? Encapsulation and Ordering of Hard Electropositive Cations," *J. Am. Chem. Soc.*, vol. 121, no. 50, pp. 11720–11732, Dec. 1999.
- [37] G. Eda, T. Fujita, H. Yamaguchi, D. Voiry, M. Chen, and M. Chhowalla, "Coherent Atomic and Electronic Heterostructures of Single-Layer MoS₂," *ACS Nano*, vol. 6, no. 8, pp. 7311–7317, Aug. 2012.
- [38] V. Alexiev, H. Meyer zu Altenschildesche, R. Prins, and T. Weber, "Solid-State NMR Study of Hydrated Intercalation Compounds of Molybdenum Disulfide," *Chem. Mater.*, vol. 11, no. 7, pp. 1742–1746, Jul. 1999.
- [39] A. Splendiani, L. Sun, Y. Zhang, T. Li, J. Kim, C.-Y. Chim, G. Galli, and F. Wang, "Emerging Photoluminescence in Monolayer MoS₂," *Nano Lett.*, vol. 10, no. 4, pp. 1271–1275, Apr. 2010.
- [40] A. N. Enyashin and G. Seifert, "Density-functional study of LixMoS₂ intercalates (0 ≤ x ≤ 1)," *Comput. Theor. Chem.*, vol. 999, pp. 13–20, Nov. 2012.
- [41] S. Jiménez Sandoval, D. Yang, R. Frindt, and J. Irwin, "Raman study and lattice dynamics of single molecular layers of MoS₂," *Phys. Rev. B*, vol. 44, no. 8, pp. 3955–3962, Aug. 1991.
- [42] M. Calandra, "Chemically exfoliated single-layer MoS₂: Stability, lattice dynamics, and catalytic adsorption from first principles," *Phys. Rev. B*, vol. 88, no. 24, p. 245428, Dec. 2013.
- [43] P. Joensen, E. D. Crozier, N. Alberding, and R. F. Frindt, "A study of single-layer and restacked MoS₂ by X-ray diffraction and X-ray absorption spectroscopy," *J. Phys. C Solid State Phys.*, vol. 20, no. 26, pp. 4043–4053, Sep. 1987.
- [44] P. Joensen, R. F. Frindt, and S. R. Morrison, "Single-layer MoS₂," *Mater. Res. Bull.*, vol. 21, no. 4, pp. 457–461, Apr. 1986.
- [45] Y.-C. Lin, D. O. Dumcenco, Y.-S. Huang, and K. Suenaga, "Atomic mechanism of the semiconducting-to-metallic phase transition in single-layered MoS₂," *Nat. Nanotechnol.*, vol. 9, no. 5, pp. 391–396, Apr. 2014.
- [46] V. Alexiev, H. Meyer zu Altenschildesche, R. Prins, and T. Weber, "Solid-State NMR Study of Hydrated Intercalation Compounds of Molybdenum Disulfide," *Chem. Mater.*, vol. 11, no. 7, pp. 1742–1746, Jul. 1999.
- [47] K.-A. N. Duerloo, M. T. Ong, and E. J. Reed, "Intrinsic Piezoelectricity in Two-Dimensional Materials," *J. Phys. Chem. Lett.*, vol. 3, no. 19, pp. 2871–2876, Oct. 2012.
- [48] W. Wu, L. Wang, Y. Li, F. Zhang, L. Lin, S. Niu, D. Chenet, X. Zhang, Y. Hao, T. F. Heinz, J. Hone, and Z. L. Wang, "Piezoelectricity of single-atomic-layer MoS₂ for energy conversion and piezotronics," *Nature*, vol. 514, no. 7523, pp. 470–474, Oct. 2014.
- [49] N. Jalili, "Nanotube-Based Actuator and Sensor Paradigm: Conceptual Design and Challenges," 2003, vol. 2003, pp. 271–276.
- [50] G. Eda, H. Yamaguchi, D. Voiry, T. Fujita, M. Chen, and M. Chhowalla, "Photoluminescence from Chemically Exfoliated MoS₂," *Nano Lett.*, vol. 11, no. 12, pp. 5111–5116, Dec. 2011.

- [51] M. Acerce, D. Voiry, and M. Chhowalla, "Metallic 1T phase MoS₂ nanosheets as supercapacitor electrode materials," *Nat. Nanotechnol.*, vol. 10, no. 4, pp. 313–318, Mar. 2015.
- [52] D. Gendron, G. Bubak, L. Ceseracciu, F. Ricciardella, A. Ansaldo, and D. Ricci, "Significant strain and force improvements of single-walled carbon nanotube actuator: A metal chalcogenides approach," *Sens. Actuators B Chem.*, vol. 230, pp. 673–683, Jul. 2016.
- [53] Q. Mahmood, M. G. Kim, S. Yun, S.-M. Bak, X.-Q. Yang, H. S. Shin, W. S. Kim, P. V. Braun, and H. S. Park, "Unveiling Surface Redox Charge Storage of Interacting Two-Dimensional Heteronanoseeds in Hierarchical Architectures," *Nano Lett.*, vol. 15, no. 4, pp. 2269–2277, Apr. 2015.
- [54] V. Alexiev, R. Prins, and T. Weber, "DFT study of MoS₂ and hydrogen adsorbed on the (1010) face of MoS₂," *Phys. Chem. Chem. Phys.*, vol. 3, no. 23, pp. 5326–5336, Nov. 2001.
- [55] X. Guo, G. Yang, J. Zhang, and X. Xu, "Structural, mechanical and electronic properties of in-plane 1T/2H phase interface of MoS₂ heterostructures," *AIP Adv.*, vol. 5, no. 9, p. 97174, Sep. 2015.
- [56] J. P. Oviedo, S. Kc, N. Lu, J. Wang, K. Cho, R. M. Wallace, and M. J. Kim, "In Situ TEM Characterization of Shear-Stress-Induced Interlayer Sliding in the Cross Section View of Molybdenum Disulfide," *ACS Nano*, vol. 9, no. 2, pp. 1543–1551, Feb. 2015.
- [57] D. N. Futaba, K. Hata, T. Yamada, T. Hiraoka, Y. Hayamizu, Y. Kakudate, O. Tanaike, H. Hatori, M. Yumura, and S. Iijima, "Shape-engineerable and highly densely packed single-walled carbon nanotubes and their application as super-capacitor electrodes," *Nat. Mater.*, vol. 5, no. 12, pp. 987–994, Dec. 2006.
- [58] K. H. An, "Supercapacitors using singlewalled carbon nanotube electrodes," 2001, vol. 590, pp. 241–244.
- [59] V. C. Almeida, R. Silva, M. Acerce, O. P. Junior, A. L. Cazetta, A. C. Martins, X. Huang, M. Chhowalla, and T. Asefa, "N-doped ordered mesoporous carbons with improved charge storage capacity by tailoring N-dopant density with solvent-assisted synthesis," *J. Mater. Chem. A*, vol. 2, no. 36, p. 15181, Jul. 2014.
- [60] C. Liu, Z. Yu, D. Neff, A. Zhamu, and B. Z. Jang, "Graphene-Based Supercapacitor with an Ultrahigh Energy Density," *Nano Lett.*, vol. 10, no. 12, pp. 4863–4868, Dec. 2010.
- [61] B. E. Conway, *Electrochemical Supercapacitors Scientific Fundamentals and Technological Applications*. Boston, MA: Springer US, 1999.
- [62] I.-H. Kim, J.-H. Kim, and K.-B. Kim, "Electrochemical Characterization of Electrochemically Prepared Ruthenium Oxide/Carbon Nanotube Electrode for Supercapacitor Application," *Electrochem. Solid-State Lett.*, vol. 8, no. 7, p. A369, 2005.
- [63] J.-K. Chang and W.-T. Tsai, "Material Characterization and Electrochemical Performance of Hydrous Manganese Oxide Electrodes for Use in Electrochemical Pseudocapacitors," *J. Electrochem. Soc.*, vol. 150, no. 10, p. A1333, 2003.
- [64] E. Frackowiak, "Carbon materials for supercapacitor application," *Phys. Chem. Chem. Phys.*, vol. 9, no. 15, p. 1774, 2007.
- [65] L. L. Zhang and X. S. Zhao, "Carbon-based materials as supercapacitor electrodes," *Chem. Soc. Rev.*, vol. 38, no. 9, p. 2520, 2009.
- [66] G. Wang, L. Zhang, and J. Zhang, "A review of electrode materials for electrochemical supercapacitors," *Chem Soc Rev*, vol. 41, no. 2, pp. 797–828, 2012.
- [67] G. A. Snook, P. Kao, and A. S. Best, "Conducting-polymer-based supercapacitor devices and electrodes," *J. Power Sources*, vol. 196, no. 1, pp. 1–12, Jan. 2011.

- [68] J. Chmiola, G. Yushin, R. Dash, and Y. Gogotsi, "Effect of pore size and surface area of carbide derived carbons on specific capacitance," *J. Power Sources*, vol. 158, no. 1, pp. 765–772, Jul. 2006.
- [69] J. Chmiola, "Anomalous Increase in Carbon Capacitance at Pore Sizes Less Than 1 Nanometer," *Science*, vol. 313, no. 5794, pp. 1760–1763, Sep. 2006.
- [70] E. Frackowiak, G. Lota, J. Machnikowski, C. Vix-Guterl, and F. Béguin, "Optimisation of supercapacitors using carbons with controlled nanotexture and nitrogen content," *Electrochimica Acta*, vol. 51, no. 11, pp. 2209–2214, Feb. 2006.
- [71] M. Toupin, T. Brousse, and D. Bélanger, "Influence of Microstructure on the Charge Storage Properties of Chemically Synthesized Manganese Dioxide," *Chem. Mater.*, vol. 14, no. 9, pp. 3946–3952, Sep. 2002.
- [72] N. Tang, X. Tian, C. Yang, and Z. Pi, "Facile synthesis of α -MnO₂ nanostructures for supercapacitors," *Mater. Res. Bull.*, vol. 44, no. 11, pp. 2062–2067, Nov. 2009.
- [73] T. Brousse and D. Bélanger, "A Hybrid Fe[₃]O[₄]-MnO[₂] Capacitor in Mild Aqueous Electrolyte," *Electrochem. Solid-State Lett.*, vol. 6, no. 11, p. A244, 2003.
- [74] Y.-Z. Zheng, H.-Y. Ding, and M.-L. Zhang, "Hydrous-ruthenium-oxide thin film electrodes prepared by cathodic electrodeposition for supercapacitors," *Thin Solid Films*, vol. 516, no. 21, pp. 7381–7385, Sep. 2008.
- [75] J. . Zheng and Y. Xin, "Characterization of RuO₂·xH₂O with various water contents," *J. Power Sources*, vol. 110, no. 1, pp. 86–90, Jul. 2002.
- [76] Z. Sun, Z. Liu, B. Han, S. Miao, J. Du, and Z. Miao, "Microstructural and electrochemical characterization of RuO₂/CNT composites synthesized in supercritical diethyl amine," *Carbon*, vol. 44, no. 5, pp. 888–893, Apr. 2006.
- [77] W. Sugimoto, H. Iwata, K. Yokoshima, Y. Murakami, and Y. Takasu, "Proton and Electron Conductivity in Hydrous Ruthenium Oxides Evaluated by Electrochemical Impedance Spectroscopy: The Origin of Large Capacitance," *J. Phys. Chem. B*, vol. 109, no. 15, pp. 7330–7338, Apr. 2005.
- [78] H. Y. Lee and J. B. Goodenough, "Supercapacitor Behavior with KCl Electrolyte," *J. Solid State Chem.*, vol. 144, no. 1, pp. 220–223, Apr. 1999.
- [79] V. Subramanian, H. Zhu, R. Vajtai, P. M. Ajayan, and B. Wei, "Hydrothermal Synthesis and Pseudocapacitance Properties of MnO₂ Nanostructures," *J. Phys. Chem. B*, vol. 109, no. 43, pp. 20207–20214, Nov. 2005.
- [80] P. Ragupathy, H. N. Vasan, and N. Munichandraiah, "Synthesis and Characterization of Nano-MnO[₂] for Electrochemical Supercapacitor Studies," *J. Electrochem. Soc.*, vol. 155, no. 1, p. A34, 2008.
- [81] P. Yu, X. Zhang, Y. Chen, and Y. Ma, "Solution-combustion synthesis of ϵ -MnO₂ for supercapacitors," *Mater. Lett.*, vol. 64, no. 1, pp. 61–64, Jan. 2010.
- [82] J. B. Fernandes, B. D. Desai, and V. N. K. Dalal, "Manganese dioxide — a review of a battery chemical part I. Chemical syntheses and x-ray diffraction studies of manganese dioxides," *J. Power Sources*, vol. 15, no. 4, pp. 209–237, Aug. 1985.
- [83] W. H. Baur, "Rutile-type compounds. V. Refinement of MnO₂ and MgF₂," *Acta Crystallogr. B*, vol. 32, no. 7, pp. 2200–2204, Jul. 1976.
- [84] T. Brousse, M. Toupin, R. Dugas, L. Athouël, O. Crosnier, and D. Bélanger, "Crystalline MnO[₂] as Possible Alternatives to Amorphous Compounds in Electrochemical Supercapacitors," *J. Electrochem. Soc.*, vol. 153, no. 12, p. A2171, 2006.
- [85] C.-C. Ji, M.-W. Xu, S.-J. Bao, C.-J. Cai, R.-Y. Wang, and D.-Z. Jia, "Effect of alkaline and alkaline-earth cations on the supercapacitor performance of MnO₂ with various

- crystallographic structures," *J. Solid State Electrochem.*, vol. 17, no. 5, pp. 1357–1368, May 2013.
- [86] G. Yu, L. Hu, M. Vosgueritchian, H. Wang, X. Xie, J. R. McDonough, X. Cui, Y. Cui, and Z. Bao, "Solution-Processed Graphene/MnO₂ Nanostructured Textiles for High-Performance Electrochemical Capacitors," *Nano Lett.*, vol. 11, no. 7, pp. 2905–2911, Jul. 2011.
- [87] Y. Hou, Y. Cheng, T. Hobson, and J. Liu, "Design and Synthesis of Hierarchical MnO₂ Nanospheres/Carbon Nanotubes/Conducting Polymer Ternary Composite for High Performance Electrochemical Electrodes," *Nano Lett.*, vol. 10, no. 7, pp. 2727–2733, Jul. 2010.
- [88] M. Kalaji, P. J. Murphy, and G. O. Williams, "The study of conducting polymers for use as redox supercapacitors," *Synth. Met.*, vol. 102, no. 1–3, pp. 1360–1361, Jun. 1999.
- [89] L. Li, D. C. Loveday, D. S. K. Mudigonda, and J. P. Ferraris, "Effect of Electrolytes on Performance of Electrochemical Capacitors Based on Poly[3-(3,4-difluorophenyl)thiophene]," *J. Electrochem. Soc.*, vol. 149, no. 9, p. A1201, 2002.
- [90] H. Li, J. Wang, Q. Chu, Z. Wang, F. Zhang, and S. Wang, "Theoretical and experimental specific capacitance of polyaniline in sulfuric acid," *J. Power Sources*, vol. 190, no. 2, pp. 578–586, May 2009.
- [91] A. Clemente, "Solid-state, polymer-based, redox capacitors," *Solid State Ion.*, vol. 85, no. 1–4, pp. 273–277, May 1996.
- [92] A. Laforgue, P. Simon, C. Sarrazin, and J.-F. Fauvarque, "Polythiophene-based supercapacitors," *J. Power Sources*, vol. 80, no. 1–2, pp. 142–148, Jul. 1999.
- [93] M. Mastragostino, R. Paraventi, and A. Zanelli, "Supercapacitors Based on Composite Polymer Electrodes," *J. Electrochem. Soc.*, vol. 147, no. 9, p. 3167, 2000.
- [94] Z. Zhu, G. Wang, M. Sun, X. Li, and C. Li, "Fabrication and electrochemical characterization of polyaniline nanorods modified with sulfonated carbon nanotubes for supercapacitor applications," *Electrochimica Acta*, vol. 56, no. 3, pp. 1366–1372, Jan. 2011.
- [95] Y.-G. Wang, H.-Q. Li, and Y.-Y. Xia, "Ordered Whiskerlike Polyaniline Grown on the Surface of Mesoporous Carbon and Its Electrochemical Capacitance Performance," *Adv. Mater.*, vol. 18, no. 19, pp. 2619–2623, Oct. 2006.
- [96] H. Zhang, G. Cao, Z. Wang, Y. Yang, Z. Shi, and Z. Gu, "Tube-covering-tube nanostructured polyaniline/carbon nanotube array composite electrode with high capacitance and superior rate performance as well as good cycling stability," *Electrochem. Commun.*, vol. 10, no. 7, pp. 1056–1059, Jul. 2008.
- [97] Q. Qu, P. Zhang, B. Wang, Y. Chen, S. Tian, Y. Wu, and R. Holze, "Electrochemical Performance of MnO₂ Nanorods in Neutral Aqueous Electrolytes as a Cathode for Asymmetric Supercapacitors," *J. Phys. Chem. C*, vol. 113, no. 31, pp. 14020–14027, Aug. 2009.
- [98] M. Galiński, A. Lewandowski, and I. Stępnia, "Ionic liquids as electrolytes," *Electrochimica Acta*, vol. 51, no. 26, pp. 5567–5580, Aug. 2006.
- [99] L. J. Hardwick, M. Hahn, P. Ruch, M. Holzapfel, W. Scheifele, H. Buqa, F. Krumeich, P. Novák, and R. Kötz, "An in situ Raman study of the intercalation of supercapacitor-type electrolyte into microcrystalline graphite," *Electrochimica Acta*, vol. 52, no. 2, pp. 675–680, Oct. 2006.
- [100] F. Meng and Y. Ding, "Sub-Micrometer-Thick All-Solid-State Supercapacitors with High Power and Energy Densities," *Adv. Mater.*, vol. 23, no. 35, pp. 4098–4102, Sep. 2011.

- [101] D. Karabelli, J.-C. Leprêtre, F. Alloin, and J.-Y. Sanchez, "Poly(vinylidene fluoride)-based macroporous separators for supercapacitors," *Electrochimica Acta*, vol. 57, pp. 98–103, Dec. 2011.
- [102] E. Frackowiak and F. Béguin, "Carbon materials for the electrochemical storage of energy in capacitors," *Carbon*, vol. 39, no. 6, pp. 937–950, May 2001.
- [103] J. Yan, W. Sun, T. Wei, Q. Zhang, Z. Fan, and F. Wei, "Fabrication and electrochemical performances of hierarchical porous Ni(OH)₂ nanoflakes anchored on graphene sheets," *J. Mater. Chem.*, vol. 22, no. 23, p. 11494, 2012.
- [104] T. Hibino, K. Kobayashi, M. Nagao, and S. Kawasaki, "High-temperature supercapacitor with a proton-conducting metal pyrophosphate electrolyte," *Sci. Rep.*, vol. 5, p. 7903, Jan. 2015.
- [105] P. L. Taberna, P. Simon, and J. F. Fauvarque, "Electrochemical Characteristics and Impedance Spectroscopy Studies of Carbon-Carbon Supercapacitors," *J. Electrochem. Soc.*, vol. 150, no. 3, p. A292, 2003.
- [106] J. F. Robinson and Y. P. Kayinam, "Charge transport in conducting polymers: insights from impedance spectroscopy," *Chem. Soc. Rev.*, vol. 38, no. 12, p. 3339, 2009.
- [107] K. H. Kim, M. Yang, K. M. Cho, Y.-S. Jun, S. B. Lee, and H.-T. Jung, "High quality reduced graphene oxide through repairing with multi-layered graphene ball nanostructures," *Sci. Rep.*, vol. 3, Nov. 2013.
- [108] Q. Chen, Y. Wang, X. Zhou, Q. M. Zhang, and S. Zhang, "High field tunneling as a limiting factor of maximum energy density in dielectric energy storage capacitors," *Appl. Phys. Lett.*, vol. 92, no. 14, p. 142909, 2008.
- [109] J. Yan, J. Liu, Z. Fan, T. Wei, and L. Zhang, "High-performance supercapacitor electrodes based on highly corrugated graphene sheets," *Carbon*, vol. 50, no. 6, pp. 2179–2188, May 2012.
- [110] H. Ohshima and K. Furusawa, Eds., *Electrical phenomena at interfaces: fundamentals, measurements, and applications*, 2nd ed., And expanded. New York: M. Dekker, 1998.
- [111] R. Hogg, T. W. Healy, and D. W. Fuerstenau, "Mutual coagulation of colloidal dispersions," *Trans. Faraday Soc.*, vol. 62, p. 1638, 1966.
- [112] P. F. Fox and P. L. H. McSweeney, Eds., *Advanced dairy chemistry. Vol. 2: Lipids*, 3. ed. New York, NY: Springer, 2006.
- [113] E. J. W. Verwey and J. T. G. Overbeek, *Theory of the stability of lyophobic colloids*. Mineola, N.Y: Dover Publications, 1999.
- [114] H. Helmholtz, "Studien über electrische Grenzschichten," *Ann. Phys. Chem.*, vol. 243, no. 7, pp. 337–382, 1879.
- [115] G. Gouy, "Constitution of the electric charge at the surface of an electrolyte," *J. Phys.*, vol. 4, no. 457, 1910.
- [116] D. L. Chapman, "LI. A contribution to the theory of electrocapillarity," *Philos. Mag. Ser. 6*, vol. 25, no. 148, pp. 475–481, Apr. 1913.
- [117] O. Stern, "ZUR THEORIE DER ELEKTROLYTISCHEN DOPPELSCHICHT," *Z. Für Elektrochem. Angew. Phys. Chem.*, vol. 30, no. 21–22, pp. 508–516, 1924.
- [118] D. C. Grahame, "The Electrical Double Layer and the Theory of Electrocapillarity," *Chem. Rev.*, vol. 41, no. 3, pp. 441–501, Dec. 1947.
- [119] J. O. Bockris, M. A. V. Devanathan, and K. Muller, "On the Structure of Charged Interfaces," *Proc. R. Soc. Math. Phys. Eng. Sci.*, vol. 274, no. 1356, pp. 55–79, Jun. 1963.
- [120] P. Simon, Y. Gogotsi, and B. Dunn, "Where Do Batteries End and Supercapacitors Begin?," *Science*, vol. 343, no. 6176, pp. 1210–1211, Mar. 2014.

- [121] A. M. Gómez-Marín, R. Rizo, and J. M. Feliu, "Some reflections on the understanding of the oxygen reduction reaction at Pt(111)," *Beilstein J. Nanotechnol.*, vol. 4, pp. 956–967, Dec. 2013.
- [122] A. K. Shukla, S. Sampath, and K. Vijayamohanan, "Electrochemical supercapacitors: Energy storage beyond batteries," *Curr. Sci.*, vol. 79, no. 12, pp. 1656–1662, 2000.
- [123] M. Deschamps, E. Gilbert, P. Azais, E. Raymundo-Piñero, M. R. Ammar, P. Simon, D. Massiot, and F. Béguin, "Exploring electrolyte organization in supercapacitor electrodes with solid-state NMR," *Nat. Mater.*, vol. 12, no. 4, pp. 351–358, Feb. 2013.
- [124] K. Naoi, "Quartz Crystal Microbalance Study: Ionic Motion Across Conducting Polymers," *J. Electrochem. Soc.*, vol. 138, no. 2, p. 440, 1991.
- [125] M. D. Levi, G. Salitra, N. Levy, D. Aurbach, and J. Maier, "Application of a quartz-crystal microbalance to measure ionic fluxes in microporous carbons for energy storage," *Nat. Mater.*, vol. 8, no. 11, pp. 872–875, Nov. 2009.
- [126] C. Prehal, D. Weingarth, E. Perre, R. T. Lechner, H. Amenitsch, O. Paris, and V. Presser, "Tracking the structural arrangement of ions in carbon supercapacitor nanopores using in situ small-angle X-ray scattering," *Energy Env. Sci.*, vol. 8, no. 6, pp. 1725–1735, 2015.
- [127] K. Xu, X. Ji, B. Zhang, C. Chen, Y. Ruan, L. Miao, and J. Jiang, "Charging/Discharging Dynamics in Two-Dimensional Titanium Carbide (MXene) Slit Nanopore: Insights from molecular dynamic study," *Electrochimica Acta*, vol. 196, pp. 75–83, Apr. 2016.
- [128] J.-K. Chang, M.-T. Lee, and W.-T. Tsai, "In situ Mn K-edge X-ray absorption spectroscopic studies of anodically deposited manganese oxide with relevance to supercapacitor applications," *J. Power Sources*, vol. 166, no. 2, pp. 590–594, Apr. 2007.
- [129] Y. Mo, M. R. Antonio, and D. A. Scherson, "In Situ Ru K-Edge X-Ray Absorption Fine Structure Studies of Electroprecipitated Ruthenium Dioxide Films with Relevance to Supercapacitor Applications," *J. Phys. Chem. B*, vol. 104, no. 42, pp. 9777–9779, Oct. 2000.
- [130] M. R. Lukatskaya, S.-M. Bak, X. Yu, X.-Q. Yang, M. W. Barsoum, and Y. Gogotsi, "Probing the Mechanism of High Capacitance in 2D Titanium Carbide Using In Situ X-Ray Absorption Spectroscopy," *Adv. Energy Mater.*, vol. 5, no. 15, p. 1500589, Aug. 2015.
- [131] M. Hahn, O. Barbieri, R. Gallay, and R. Kötz, "A dilatometric study of the voltage limitation of carbonaceous electrodes in aprotic EDLC type electrolytes by charge-induced strain," *Carbon*, vol. 44, no. 12, pp. 2523–2533, Oct. 2006.
- [132] R. H. Baughman, "Carbon Nanotube Actuators," *Science*, vol. 284, no. 5418, pp. 1340–1344, May 1999.
- [133] Y. Zhao, L. Song, Z. Zhang, and L. Qu, "Stimulus-responsive graphene systems towards actuator applications," *Energy Environ. Sci.*, vol. 6, no. 12, p. 3520, 2013.
- [134] J. Liu, Z. Wang, X. Xie, H. Cheng, Y. Zhao, and L. Qu, "A rationally-designed synergetic polypyrrole/graphene bilayer actuator," *J. Mater. Chem.*, vol. 22, no. 9, p. 4015, 2012.
- [135] G. W. Rogers and J. Z. Liu, "Graphene Actuators: Quantum-Mechanical and Electrostatic Double-Layer Effects," *J. Am. Chem. Soc.*, vol. 133, no. 28, pp. 10858–10863, Jul. 2011.
- [136] W. Guo and Y. Guo, "Giant Axial Electrostrictive Deformation in Carbon Nanotubes," *Phys. Rev. Lett.*, vol. 91, no. 11, Sep. 2003.
- [137] P. Brochu and Q. Pei, "Advances in Dielectric Elastomers for Actuators and Artificial Muscles," *Macromol. Rapid Commun.*, vol. 31, no. 1, pp. 10–36, Jan. 2010.
- [138] H.-J. Jin, X.-L. Wang, S. Parida, K. Wang, M. Seo, and J. Weissmüller, "Nanoporous Au–Pt Alloys As Large Strain Electrochemical Actuators," *Nano Lett.*, vol. 10, no. 1, pp. 187–194, Jan. 2010.

- [139] C. Cheng and A. H. W. Ngan, "Reversible Electrochemical Actuation of Metallic Nanohoneycombs Induced by Pseudocapacitive Redox Processes," *ACS Nano*, vol. 9, no. 4, pp. 3984–3995, Apr. 2015.
- [140] S. R. Shin, C. K. Lee, I. S. So, J. H. Jeon, T. M. Kang, C. W. Kee, S. I. Kim, G. M. Spinks, G. G. Wallace, and S. J. Kim, "DNA-Wrapped Single-Walled Carbon Nanotube Hybrid Fibers for supercapacitors and Artificial Muscles," *Adv. Mater.*, vol. 20, no. 3, pp. 466–470, Feb. 2008.
- [141] J. Liang, Y. Huang, J. Oh, M. Kozlov, D. Sui, S. Fang, R. H. Baughman, Y. Ma, and Y. Chen, "Electromechanical Actuators Based on Graphene and Graphene/Fe₃O₄ Hybrid Paper," *Adv. Funct. Mater.*, vol. 21, no. 19, pp. 3778–3784, Oct. 2011.
- [142] X. Xie, L. Qu, C. Zhou, Y. Li, J. Zhu, H. Bai, G. Shi, and L. Dai, "An Asymmetrically Surface-Modified Graphene Film Electrochemical Actuator," *ACS Nano*, vol. 4, no. 10, pp. 6050–6054, Oct. 2010.
- [143] L. Kong and W. Chen, "Carbon Nanotube and Graphene-based Bioinspired Electrochemical Actuators," *Adv. Mater.*, vol. 26, no. 7, pp. 1025–1043, Feb. 2014.
- [144] M. Kintscher and M. Wiedemann, "Design of a Smart Leading Edge Device," in *Adaptive, tolerant and efficient composite structures*, M. Wiedemann and M. Sinapius, Eds. Berlin, Heidelberg: Springer Berlin Heidelberg, 2013, pp. 381–390.
- [145] R. K. Josephson, "Comparative Physiology of Insect Flight Muscle," in *Nature's Versatile Engine: Insect Flight Muscle Inside and Out*, Boston, MA: Springer US, 2006, pp. 34–43.
- [146] M. Pagitz, M. Pagitz, and C. Hühne, "A modular approach to adaptive structures," *Bioinspir. Biomim.*, vol. 9, no. 4, p. 46005, Oct. 2014.
- [147] Q. Pei and O. Inganaes, "Electrochemical applications of the bending beam method. 1. Mass transport and volume changes in polypyrrole during redox," *J. Phys. Chem.*, vol. 96, no. 25, pp. 10507–10514, Dec. 1992.
- [148] M. Christophersen, B. Shapiro, and E. Smela, "Characterization and modeling of PPy bilayer microactuators," *Sens. Actuators B Chem.*, vol. 115, no. 2, pp. 596–609, Jun. 2006.
- [149] G. Gu, M. Schmid, P.-W. Chiu, A. Minett, J. Fraysse, G.-T. Kim, S. Roth, M. Kozlov, E. Muñoz, and R. H. Baughman, "V₂O₅ nanofibre sheet actuators," *Nat. Mater.*, vol. 2, no. 5, pp. 316–319, May 2003.
- [150] J. Torop, V. Palmre, M. Arulepp, T. Sugino, K. Asaka, and A. Aabloo, "Flexible supercapacitor-like actuator with carbide-derived carbon electrodes," *Carbon*, vol. 49, no. 9, pp. 3113–3119, Aug. 2011.
- [151] L. Lu, J. Liu, Y. Hu, Y. Zhang, and W. Chen, "Graphene-Stabilized Silver Nanoparticle Electrochemical Electrode for Actuator Design," *Adv. Mater.*, vol. 25, no. 9, pp. 1270–1274, Mar. 2013.
- [152] R. Pytel, E. Thomas, and I. Hunter, "Anisotropy of Electroactive Strain in Highly Stretched Polypyrrole Actuators," *Chem. Mater.*, vol. 18, no. 4, pp. 861–863, Feb. 2006.
- [153] M. Ghaffari, W. Kinsman, Y. Zhou, S. Murali, Q. Burlingame, M. Lin, R. S. Ruoff, and Q. M. Zhang, "Aligned Nano-Porous Microwave Exfoliated Graphite Oxide Ionic Actuators with High Strain and Elastic Energy Density," *Adv. Mater.*, vol. 25, no. 43, pp. 6277–6283, Nov. 2013.
- [154] J. Come, J. M. Black, M. R. Lukatskaya, M. Naguib, M. Beidaghi, A. J. Rondinone, S. V. Kalinin, D. J. Wesolowski, Y. Gogotsi, and N. Balke, "Controlling the actuation properties of MXene paper electrodes upon cation intercalation," *Nano Energy*, vol. 17, pp. 27–35, Oct. 2015.
- [155] X. Xie, H. Bai, G. Shi, and L. Qu, "Load-tolerant, highly strain-responsive graphene sheets," *J. Mater. Chem.*, vol. 21, no. 7, p. 2057, 2011.

- [156] T. F. Otero, "Soft, wet, and reactive polymers. Sensing artificial muscles and conformational energy," *J Mater Chem*, vol. 19, no. 6, pp. 681–689, 2009.
- [157] P. Du, X. Lin, and X. Zhang, "A multilayer bending model for conducting polymer actuators," *Sens. Actuators Phys.*, vol. 163, no. 1, pp. 240–246, Sep. 2010.
- [158] S. Timoshenko, "Analysis of Bi-Metal Thermostats," *J. Opt. Soc. Am.*, vol. 11, no. 3, p. 233, Sep. 1925.
- [159] C. Cheng, J. Weissmüller, and A. H. W. Ngan, "Fast and Reversible Actuation of Metallic Muscles Composed of Nickel Nanowire-Forest," *Adv. Mater.*, vol. 28, no. 26, pp. 5315–5321, Jul. 2016.
- [160] G. Alici, B. Mui, and C. Cook, "Bending modeling and its experimental verification for conducting polymer actuators dedicated to manipulation applications," *Sens. Actuators Phys.*, vol. 126, no. 2, pp. 396–404, Feb. 2006.
- [161] J. Weissmuller, "Charge-Induced Reversible Strain in a Metal," *Science*, vol. 300, no. 5617, pp. 312–315, Apr. 2003.
- [162] G. Eda, H. Yamaguchi, D. Voiry, T. Fujita, M. Chen, and M. Chhowalla, "Photoluminescence from Chemically Exfoliated MoS₂," *Nano Lett.*, vol. 11, no. 12, pp. 5111–5116, Dec. 2011.
- [163] C. A. Papageorgopoulos and W. Jaegermann, "Li intercalation across and along the van der Waals surfaces of MoS₂(0001)," *Surf. Sci.*, vol. 338, no. 1–3, pp. 83–93, Sep. 1995.
- [164] Q. T. Qu, B. Wang, L. C. Yang, Y. Shi, S. Tian, and Y. P. Wu, "Study on electrochemical performance of activated carbon in aqueous Li₂SO₄, Na₂SO₄ and K₂SO₄ electrolytes," *Electrochem. Commun.*, vol. 10, no. 10, pp. 1652–1655, Oct. 2008.
- [165] M. F. El-Kady, V. Strong, S. Dubin, and R. B. Kaner, "Laser Scribing of High-Performance and Flexible Graphene-Based Electrochemical Capacitors," *Science*, vol. 335, no. 6074, pp. 1326–1330, Mar. 2012.
- [166] D. Pech, M. Brunet, H. Durou, P. Huang, V. Mochalin, Y. Gogotsi, P.-L. Taberna, and P. Simon, "Ultrahigh-power micrometre-sized supercapacitors based on onion-like carbon," *Nat. Nanotechnol.*, vol. 5, no. 9, pp. 651–654, Sep. 2010.
- [167] Z. Wu, K. Parvez, X. Feng, and K. Müllen, "Graphene-based in-plane micro-supercapacitors with high power and energy densities," *Nat. Commun.*, vol. 4, Sep. 2013.
- [168] G. Du, Z. Guo, S. Wang, R. Zeng, Z. Chen, and H. Liu, "Superior stability and high capacity of restacked molybdenum disulfide as anode material for lithium ion batteries," *Chem. Commun.*, vol. 46, no. 7, p. 1106, 2010.
- [169] J. Palomo and P. N. Pintauro, "Competitive absorption of quaternary ammonium and alkali metal cations into a Nafion cation-exchange membrane," *J. Membr. Sci.*, vol. 215, no. 1–2, pp. 103–114, Apr. 2003.
- [170] R. Schöllhorn and A. Weiss, "Cation exchange reactions and layer solvate complexes of ternary phases MxMoS₂," *J. Common Met.*, vol. 36, no. 1–2, pp. 229–236, May 1974.
- [171] Y.-K. Hsu, Y.-C. Chen, Y.-G. Lin, L.-C. Chen, and K.-H. Chen, "Reversible phase transformation of MnO₂ nanosheets in an electrochemical capacitor investigated by in situ Raman spectroscopy," *Chem Commun*, vol. 47, no. 4, pp. 1252–1254, 2011.
- [172] G. G. Stoney, "The Tension of Metallic Films Deposited by Electrolysis," *Proc. R. Soc. Math. Phys. Eng. Sci.*, vol. 82, no. 553, pp. 172–175, May 1909.
- [173] M. Q. Le, J.-F. Capsal, J. Galineau, F. Ganet, X. Yin, M. (Dawn) Yang, J.-F. Chateaux, L. Renaud, C. Malhaire, P.-J. Cottinet, and R. Liang, "All-organic electrostrictive polymer composites with low driving electrical voltages for micro-fluidic pump applications," *Sci. Rep.*, vol. 5, p. 11814, Jul. 2015.

- [174] D. Li, W. F. Paxton, R. H. Baughman, T. J. Huang, J. F. Stoddart, and P. S. Weiss, "Molecular, Supramolecular, and Macromolecular Motors and Artificial Muscles," *MRS Bull.*, vol. 34, no. 9, pp. 671–681, Sep. 2009.
- [175] Kemiao Jia, S. Pal, and Huikai Xie, "An Electrothermal Tip-Tilt-Piston Micromirror Based on Folded Dual S-Shaped Bimorphs," *J. Microelectromechanical Syst.*, vol. 18, no. 5, pp. 1004–1015, Oct. 2009.
- [176] R. Ham, T. Sugar, B. Vanderborght, K. Hollander, and D. Lefeber, "Compliant actuator designs," *IEEE Robot. Autom. Mag.*, vol. 16, no. 3, pp. 81–94, Sep. 2009.
- [177] J. Come, Y. Xie, M. Naguib, S. Jesse, S. V. Kalinin, Y. Gogotsi, P. R. C. Kent, and N. Balke, "Nanoscale Elastic Changes in 2D $\text{Ti}_3\text{C}_2\text{T}_x$ (MXene) Pseudocapacitive Electrodes," *Adv. Energy Mater.*, vol. 6, no. 9, p. 1502290, May 2016.